Changes in Arctic sea ice and hydrology of pan-Arctic river basins under the impact of climate change

by

Shuyu Zhang

A thesis submitted in partial fulfillment of the requirements for the degree of

Doctor of Philosophy

in

Water Resources Engineering

Department of Civil and Environmental Engineering
University of Alberta

Abstract

Under the impact of global warming, the hydro-climatology over the Arctic has changed significantly. Warming over the Arctic region is twice the global mean warming rate since the 1980s, known as Arctic Amplification, which occurs because warming induces melting of sea ice, leading to feedbacks that accelerate the ice loss, such as the ice-albedo feedbacks, water-vapor feedbacks, cloud feedbacks, and lapse-rate feedbacks. The rapid increase in air temperature leads to substantial decline of Arctic sea ice and more intensive hydrologic processes in the pan-Arctic river basins. As the primary freshwater source to the Arctic Ocean, streamflow from the pan-Arctic river basins plays a crucial role in the sea ice formation, oceanic circulation, and the thermohaline balance in the Arctic. With a warmer atmosphere, the melting season of sea ice has lengthened and the ice cover has become younger and thinner, while the streamflow from pan-Arctic river basins have shown an increasing trends in recent years.

Numerous studies detected the teleconnections between the decline in Arctic sea ice and climate patterns, and the feedbacks, but the focus of these studies was more about average changes and the effects of individual climate patterns instead of their combined impacts. In addition, partly because of limited observed hydro-climatologic data available in pan-Arctic river basins, there have been relatively few studies on hydrologic responses of pan-Arctic river basins to climate change impact compared with studies in southern, highly populated regions. This dissertation began with an investigation on the decline of Arctic sea ice using a quantile regression method at all quantile levels. Next, hydrologic responses of the pan-Arctic river basins, such as non-stationarities and trends, and changes in wet and dry spells were analyzed by statistical and probabilistic analysis, and an artificial neural network.

Therefore, the objectives of this dissertation are: (1) to analyze changes of Arctic sea ice under the possible impacts of climate patterns and the physical mechanisms behind the teleconnection with climate patterns; (2) to identify non-stationarities and trends of streamflow from three Great Siberian river basins using statistical analysis; (3) to simulate the streamflow of four large pan-Arctic river basins with machine learning models and to project hydrologic impact of climate warming to these pan-Arctic river basins; (4) to analyze the probabilistic characteristics of the duration and temperature of both wet and dry spells of the Siberian river basins, and the joint and conditional probabilities of extreme dry and wet spells occurring in these river basins estimated from a Copulas function.

Chapter 2

The probabilistic characteristics of Arctic sea ice was investigated through quantile regression analysis with time and climate indices as covariates, such as the Arctic Oscillation (AO), the North Atlantic Oscillation (NAO), and the Pacific/North American Pattern (PNA) El Niño-Southern Oscillation (ENSO), the Pacific Decadal Oscillation (PDO), and the Atlantic Multidecadal Oscillation (AMO). The results shows that the combined impacts of climate patterns on the Arctic sea ice are statistically significant, especially on low and high quantiles. The composite analysis of climate variables shows that the anomalously strong anticyclonic circulation during years of positive AO, NAO, and PNA promotes more sea ice export through Fram Strait, resulting in excessive sea ice loss.

Chapter 3

The non-stationarities and trends of streamflow from three Siberian river basins: the Ob, Yenisei, and Lena river basins, were estimated using the traditional and modified Mann-Kendall (MK) tests, Pettitt test, and wavelet analysis, at annual, seasonal, and monthly timescales. Most stations experienced abrupt changes in 1970s to 1980s. From wavelet analysis, the streamflow of these three Siberian river basins is shown to undergo significant changes at annual, inter-annual, and decadal time scales, have significant correlation with climate patterns, namely the AO, the North Pacific Oscillation (NPO), the PNA, and ENSO. Human activities such as dam regulation, agricultural and industrial water use have contributed to the winter streamflow, while climate change and climate patterns have resulted in their non-stationary changes.

Chapter 4

Monthly streamflow of four great pan-Arctic river basins: Mackenzie river basin, Ob river basin, Lena river basin, and Yenisei river basin were modelled using several popular machine learning models: Support Vector Regression Model (SVM), Artificial Neural Network (ANN), and Multi-Variable Regression Model. The results show that SVM performs better than ANN and MLR in both the calibration and validation stages. After validation, SVM, with precipitation, potential evapotranspiration, and temperature as predictors, was used to project the monthly streamflow of these four river basins subjected to climate change impact based on RCP4.5 and RCP8.5 climate scenarios of four CMIP5 GCMs: ACCESS 1.0, CanESM2, HadESM2-ES, and MPI-ESM of AR5 of IPCC, from 2006 to 2100. Results show that under climate warming impact attributed to rising concentration of greenhouse gas emissions, the monthly streamflow of the four great pan-Arctic river basins are projected to increase significantly but at different magnitudes. The annual flow pattern is projected to shift, with higher winter flows and the onset of spring snowmelt occurring earlier with higher peak flows at the expense of summer flows.

Chapter 5

Wet and dry spells in three Siberia river basins based on the daily precipitation and temperature records from stations were analyzed. The GEV-Type III distribution were found to have good performance in describing the probabilistic characteristic of the temperature for both dry and wet spells, while the two-parameter negative binomial distribution can describe that of the duration for dry and wet spells. By fitting the empirical joint probability distribution, Gumbel and Clayton Copulas from the Archimedean Copula families performs well in describing the relationships between the duration of both wet and dry spells and air temperature. Based on the fitted copulas joint probability distribution, the likelihood of suffering from extreme dry and wet spells were estimated and presented as conditional and joint return periods. The results reveal that the north of Altay Mountain within Ob river basin, the Stanovoy Range within the Lena river, and Dzhugdzhur Mountains at the southeast of Lena river basin have higher likelihood of suffering from extreme dry and wet spell with long duration and high temperature than other places.

Conclusions and future research are provided in Chapter 6.

Preface

This thesis is based on four major chapters and is organized in an article format. This thesis consists of four chapters and each chapter is written as an integrated paper for journal submission. As such, each chapter contains standalone introductions, methods, results and conclusions. A general introduction section is provided at the beginning of the thesis, research conclusions and recommendations are summarized in Chapter 6, and supplementary materials are provided at the end of thesis. Chapter 2 of the thesis has been published as Shuyu. Zhang, Thian. Yew. Gan, and Andrew. B. G. Bush, 2020: Variability of Arctic Sea Ice Based on Quantile Regression and the Teleconnection with Large-Scale Climate Patterns. Journal of Climate, 33, 4009-4025. https://doi.org/10.1175/JCLI-D-19-0375.1. For the work done in Chapter 3, 4, and 5, I was responsible for the design of the research topic, data collection, data analysis, and the manuscript composition. I am planning to submit works on Chapter 3 to 5 to scientific journals.

An aggregated bibliography is provided for the entire thesis to avoid reference repetition

Dedication

This thesis is dedicated to my parents, my families and my best friend Man, Kang, for their unconditional love, understanding, and support during my entire academic journey. Without them, I would not be the person I am today. I love you all. I also wish to dedicate this thesis to my Charlie, Zhou, whose spirits provide me endless encouragement as a constant source of motivation that inspires me to persist and finish this thesis.

Acknowledgements

First, I would like to express my sincere gratitude to my supervisor Professor Thian Yew Gan and co-supervisor Professor Andrew. G. Bush, for their continuous support and encouragement of my PhD research, for his enthusiasm, immense knowledge, inspiration, patience, motivation and guidance over the past four years. I would like to thank professors who have give my suggestions unconditionally. Their enthusiasm of learning and academic thinking have been a constant inspiration for my entire academic journey. My sincere thanks also go to the rest of my thesis committee for their valuable comments and suggestions. Finally, I would like to acknowledge the China Scholarship Council (CSC), the University of Alberta, Roy Dean Hibbs Travel Awards, and R Larry Gerard Memorial Scholarship, for financial assistance throughout the course of my research.

Table of Content

List of Tables

List of Figures

Chapter 1. General Introduction

According to the Intergovernmental Panel on Climate Change (IPCC) Fifth Assessment Report, Arctic Amplification is climate change impact amplified in the Arctic, which has been warming at twice the global rate since the 1980s, caused by several feedback mechanisms (Delworth 2000; IPCC 2014; Knutson et al. 2006). Because of climate warming the ice cover in the Arctic Ocean has been shrinking at a trend of -4.1±0.3% per decade during the period of 1979 to 2010, as determined from satellite passive microwave radiometer data (Cavalieri and Parkinson 2012); shrinking sea ice extent has been a characteristic feature of the global climate system in recent years (Chapin III et al. 2005; Graversen et al. 2008; Mauritsen 2016). Significant loss of sea ice allows for strong latent heat fluxes to escape from the ocean to the atmosphere, and the enhanced surface evaporation due to retreating winter sea ice and warming will amplify the Arctic hydrologic cycle (Bintanja and Selten 2014; Boisvert and Stroeve 2015). Coincidentally, the average annual discharge of fresh water from the six largest Eurasian rivers to the Arctic Ocean increased by about 7% from 1936 to 1999, at a mean annual rate of increase of 2.0 ± 0.7 km^3 per year (McClelland et al. 2006; Peterson et al. 2006; Peterson et al. 2002). Precipitation is the main input of the Arctic hydrological cycle that directly and indirectly affects the Arctic Ocean's freshwater balance and stratification (Bintanja et al. 2018; Kattsov et al. 2007). Furthermore, precipitation over Arctic terrain has been shown to be related to large-scale climate patterns and atmospheric circulation (Dirmeyer et al. 2013; Serreze et al. 2002a). In the snow-dominated pan-Arctic river basins, documented hydrologic trends over recent decades generally include decreasing snowpack, a longer snow-free season, increasing precipitation, a larger proportion of precipitation occurring as liquid rainfall, higher evapotranspiration loss, lower lake levels, a widespread increase in shrub abundance, increased thawing of permafrost, earlier onset of spring snowmelt, and higher winter flow at the expense of lower summer flow (Bring et al. 2016; Chapin III et al. 2005; Han et al. 2018; Scheepers et al. 2018; Schuur et al. 2009; Serreze et al. 2002a; Sturm et al. 2001). These trends will persist and amplify with continued emissions of greenhouse gases (Swann et al. 2010; Yang et al. 2002), and further changes in regional temperature and precipitation patterns are expected to affect the Arctic sea ice (Arnell 2005; White et al. 2007). Thus, it is important to investigate changes of Arctic sea ice in conjunction with the hydrological changes over Arctic basins to more accurately predict future northern hydrology and ecology, as well as the global climate. The key objectives of this thesis are: 1) to further understanding the changes of Arctic sea ice and the possible teleconnections with climate patterns; 2) to detect the non-stationarity of streamflow in pan-Arctic river basins and its relationship with climate patterns; 3) to simulate and predict the future streamflow from pan-Arctic river basins under different carbon emission scenarios with limited input; 4) to investigate the probabilistic characteristics of dry and wet spells over pan-Arctic river basins.

Chapter 2 has been published in the Journal of Climate with the following citation: Zhang, S., T. Y. Gan, and A. B. G. Bush, 2020: Variability of Arctic Sea Ice Based on Quantile Regression and the Teleconnection with Large-Scale Climate Patterns. Journal of Climate, 33, 4009-4025. https://doi.org/10.1175/JCLI-D-19-0375.1.

Under global warming, Arctic sea ice has declined significantly in recent decades, with years of extremely low sea ice occurring more frequently. Recent studies suggest that teleconnections with large-scale climate patterns could induce the observed extreme sea ice loss. In this study, a probabilistic analysis of Arctic sea ice was conducted using quantile regression analysis with covariates, including time and climate indices. From temporal trends at quantile levels from 0.01 to 0.99, Arctic sea ice shows statistically significant decreases over all quantiles levels, though of different magnitudes at different quantiles. At the representative extreme quantile levels of the 5th and 95th percentiles, the Arctic Oscillation (AO), the North Atlantic Oscillation (NAO), and the Pacific/North American Pattern (PNA) have more significant influence on Arctic sea ice than the El Niño-Southern Oscillation (ENSO), the Pacific Decadal Oscillation (PDO), and the Atlantic Multidecadal Oscillation (AMO). Positive AO as well as positive NAO contribute to low winter sea ice, and a positive PNA contributes to low summer Arctic sea ice. If, in addition to these conditions, there is concurrently positive AMO and PDO, the sea ice decrease is amplified. Teleconnections between Arctic sea ice and the climate patterns were demonstrated through a composite analysis of the climate variables. The anomalously strong anticyclonic circulation during the years of positive AO, NAO, and PNA, promotes more sea ice export through Fram Strait, resulting in excessive sea ice loss. The probabilistic analyses of the teleconnections between the Arctic sea ice and climate patterns confirms the crucial role that the climate patterns and their combinations play in overall sea ice reduction, but particularly on the low and high quantiles of sea ice concentration.

Chapter 3: Arctic rivers contribute more than one third of the total freshwater discharge into the Arctic Ocean, and therefore play an essential role in the heat and mass circulation in the Arctic atmosphere/ocean system. With the current Arctic warming, the discharge of the largest Arctic rivers in Siberia were noticed to increase in the past decades. A non-stationary analysis is used in this study to estimate changes in the streamflow of three large Siberian river basins: the Ob, Yenisei, and Lena river basins. Through the regular and modified Mann-Kendall (MK) test, significant trend, auto-correlation and long-term persistence are determined in the streamflow time series of the Ob, Yenisei, and Lena river basins at annual, seasonal, and monthly timescales. Most stations are found to have abruptly changed during the 1970s to 1980s through the Pettitt test.

From a wavelet analysis, significant changes in periods at annual, inter-annual, and decadal periods are found in the streamflow of these three Siberian river basins. The streamflows are found to have significant correlation with climate patterns, namely the Arctic Oscillation, the North Pacific Oscillation, the Pacific/North America Pattern, and ENSO, at different time-scales, respectively, through wavelet coherence analysis. Results prove the existence of non-stationarity within the streamflow of large Siberian river basins at multi-time-scales. Human activities, such as dam regulation and agricultural and industrial water use have limited influence on the seasonal streamflow changes, while the climate change and climate pattern have more responsibility for their non-stationary changes.

Chapter 4: as the largest freshwater source to the Arctic Ocean, streamflow plays a crucial role in sea ice formation, oceanic circulation, and the thermohaline balance in the Arctic. Under a warmer climate, streamflow from the pan-Arctic river basins has exhibited an increasing trend in recent years. However, due to the limited number of observational climate stations in the Arctic, and given the challenges of modeling hydrologic processes in the northern environment subjected to the freeze-thaw cycles of snow and ice, frozen ground and permafrost, there have been a limited number of studies conducted on modeling streamflow from pan-Arctic river basins and the hydrologic impact of climate warming. In this chapter, two widely-used machine learning models are used to address this problem. The Support Vector Regression Model (SVM) and Artificial Neural Network (ANN), were first calibrated to simulate the monthly streamflow of four great pan-Arctic river basins: Mackenzie river basin, Ob river basin, Lena river basin, and Yenisei river basin. Their performances were evaluated and compared with a statistical Multi-Variable Regression (MLR) model. When compared with observations, the results show that SVM performs better than ANN and MLR in modeling the monthly streamflow of the four pan-Arctic river basins in both the calibration and validation stages. After validation, SVM, with precipitation, potential evapotranspiration, and temperature as predictors, was used to predict the monthly streamflow of these four river basins subjected to climate changes based on RCP4.5 and RCP8.5 climate scenarios of four CMIP5 GCMs: ACCESS 1.0, CanESM2, HadESM2-ES, and MPI-ESM, for the 2050s and 2080s. As expected, under climate warming impacts attributed to rising greenhouse gas concentrations, the monthly streamflow of the four great pan-Arctic river basins are projected to increase significantly but with different increasing trends in different basins. In addition, the annual flow pattern is projected to change with the onset of spring snowmelt occurring earlier with higher peak flows at the expense of summer flows.

Chapter 5: under the global warming, the frequency of extreme events have changed globally. Wet spells and dry spells as episodes of consecutive rainy or non-rainy days characterize the day-to-day variability of precipitation, which have been widely researched. However, in the pan-Arctic area, especially Siberian area, researches about the dry and wet spells are restricted by the observations. Therefore, this chapter investigated the probabilistic characteristic of duration and temperature of dry and wet spells in Siberian river basins through Copulas function. Univariate probability distribution were first fitted to the temperature and duration of dry and wet spells, and GEV Type-III distribution were found to have good performance on describing the probabilistic characteristic of temperature of both dry and wet spell, while two-parameter negative-binomial distribution performs good in describing the that of the duration. Then the Copulas function were applied to generate the conditional and joint probability distribution of the duration and temperature of spells. Gumbel and Clayton Copulas were found to have better performance in the dry spells and wet spells, respectively. The conditional and joint return periods under four extreme scenarios were estimated through the above Copulas function. Results show that the north of Altay

Mountain within Ob river basin, the Stanovoy Range within the Lena river, and Dzhugdzhur Mountains at the southeast of Lena river basin have higher likelihood of suffering from extreme dry and wet spell with long duration and high temperature than other places.

Chapter 2. Variability of Arctic sea ice based on quantile regression and the teleconnection with large-scale climate patterns

2.1 Introduction

Under the impact of global warming, Arctic sea ice (ASI) has been decreasing significantly in recent decades. With a warmer atmosphere, the melting season has lengthened (Stroeve et al. 2017) and the ice cover has become younger and thinner (Kwok 2018; Lindsay and Schweiger 2015; Stroeve et al. 2014). Warming over the Arctic region is twice the global mean, through Arctic Amplification. Arctic Amplification occurs because the warmer atmosphere induces ice loss (Serreze and Barry 2011; Serreze et al. 2009), leading to feedbacks that accelerate that ice loss, such as water-vapor feedbacks (Dessler et al. 2013; Held and Soden 2000; Solomon et al. 2010), cloud feedbacks (Bony et al. 2015; Ceppi et al. 2017; Vavrus 2004; Wetherald and Manabe 1988), lapse-rate feedbacks (Bintanja et al. 2011; Feldl et al. 2017; Graversen et al. 2014), and ice-albedo feedbacks (Kashiwase et al. 2017; Landy et al. 2015). According to climate model simulations that include these feedbacks (Stroeve et al. 2016; Stroeve et al. 2012), future reduction of Arctic sea ice will be continuous and amplified (Derksen and Brown 2012; Pithan and Mauritsen 2014), with ice-free summers occurring as early as the 2030s, and an ice-free year occurring as early as the 2050s (Onarheim et al. 2018).

The circulation of ASI, characterized by the anticyclonic Beaufort Gyre (BG) and the Transpolar Drift Stream (TDS) that transports ice from the Siberian coast across the North Pole and into the North Atlantic(Serreze and Barrett 2010), is largely controlled by the surface wind field(Thorndike and Colony 1982). The local atmospheric circulation is strongly teleconnected to the climate of remote regions through climate patterns, such as the Arctic Oscillation (AO), the North Atlantic Oscillation (NAO), the Pacific North America Pattern (PNA), and the El Niño

Southern Oscillation (ENSO). The AO is the first mode of wintertime sea level pressure (SLP) variability for regions north of 20°N (Thompson and Wallace 1998). The positive (negative) AO is characterized by low (high) SLP anomalies over the Arctic that lead to cyclonic (anticyclonic) atmospheric circulation anomalies (Armitage et al. 2018), an eastern (western) TDS, and a contracted (expanded) BG circulation (Kwok et al. 2013; Rigor et al. 2002). These, in turn, are found to minimize sea ice growth in winter (Hegyi and Taylor 2017). During positive NAO years, the enhanced north-south gradient in SLP over the North Atlantic has also been shown to drive greater southward ice flux through Fram Strait (Armitage et al. 2018; Hilmer and Jung 2000; Hurrell 1995; Kwok 2000; Kwok et al. 2013; Rigor et al. 2002). From the persistent surface forcing of quasi-stationary meridional thermal gradients, the NAO pattern has affected the sea ice variability at interannual time scales (Caian et al. 2018). The PNA is one of the dominant patterns of low-frequency variability in the extratropics of the Northern Hemisphere, and it was strongly teleconnected to the ASI in summer 2007 (L'Heureux et al. 2008). There was an extreme positive phase of PNA that exhibited a 500-hPa cyclonic anomaly west of the Aleutian Islands and a large anticyclonic anomaly south of Alaska. Combined, they drove warm maritime air from lower latitudes poleward thereby warming the western Arctic (L'Heureux et al. 2008).

ASI is teleconnected to climate patterns in a much more complex manner than a simple linear, univariate or multivariate regression manner. All PNA, AO, and PDO are related to the anomaly of the Beaufort High (L'Heureux et al. 2008; Moore et al. 2018; Petty 2018; Serreze and Barrett 2011), which is an anticyclone centered north of Alaska that largely controls the mean circulation of the Arctic sea ice cover (L'Heureux et al. 2008; Thorndike and Colony 1982). Simultaneously strong ENSO and NAO episodes were found to be associated with anomalous sea-ice extent because of strong SST anomalies and a deepened Icelandic Low that led to very strong northerly winds in the Labrador Sea (Mysak et al. 1996). Liu et al. (2004) also found that in the western Arctic the reaction of sea ice to a positive AO is similar to that to El Niño, but that this reaction is opposite in the eastern Arctic. In addition, the interaction between climate oscillations further complicates the teleconnections to sea ice: the NAO responses to ENSO in the central Pacific are mostly linear, while the NAO responses to ENSO in the Eastern Pacific are predominantly nonlinear (Ding et al. 2017a; Zhang et al. 2019). This nonstationary interaction is affected by the Atlantic Multidecadal Oscillation (AMO), such that the negative ENSO-NAO interaction in late winter will only be significant when ENSO and AMO are in-phase (Zhang et al. 2018). Moreover, during the winter of 2009-2010, ENSO was found to amplify the anomalous temperature patterns across the extratropical landmasses of the Northern Hemisphere generated by a moderate to strong AO (Cohen et al. 2010). The simultaneous occurrence of a negative PDO and La Niña events generate strong and significant North Atlantic Oscillation (NAO)-like pattern anomalies, but with opposite polarity(Ding et al. 2017b).

ASI changes non-uniformly under the influence of multiple non-uniform internal or external factors (Ding et al. 2017a; Ding et al. 2019; Ding et al. 2017b; England et al. 2019; Olonscheck et al. 2019). As a time series, sea ice characteristics could be described by statistical measures such as the mean, standard deviation, skewness, and kurtosis. Quantiles, which are widely used in hydrologic frequency analysis, represent the relative magnitudes of particular values in the historical records. For example, in this study an extremely low ice cover is represented by a small quantile, while an extremely high ice cover is represented by a large quantile. Past studies about changes in sea ice are more based on a linear regression that describes the average changes of sea ice. Quantile regression replaces the conditional mean function in linear regression with a conditional quantile function (Barbosa 2008; Koenker and Bassett 1978; Koenker and Hallock

2001). It provides slopes at any arbitrary quantile so that it is possible to analyze the trend analysis of extreme ice conditions accurately. Using quantile regression to detect the trend of ASI extent, (Tareghian and Rasmussen 2013) found high variability in the change of sea ice, such that low sea ice extent tends to decrease faster than an average sea ice extent. However, they did not consider spatial patterns of the changes in sea ice. In this study, regression coefficients between gridded sea ice concentration and climate indices were estimated to represent the spatial distribution of the sea ice's responses to the climate patterns. Next, a multivariate quantile regression model was developed that allows us to project sea ice under different possible combinations of climate patterns. Based on a composite analysis of climate variables such as sea level pressure (SLP), sea surface temperature (SST), geopotential height at 500-hPa (GPH), and wind speeds (UV), atmospheric circulations associated with the teleconnections between ASI and climate patterns are discussed.

This paper is organized as follows: The ASI data and large-scale climate patterns are described in Section 2.2; the technical details on quantile regression and composite analysis are described in Section 2.3; trend detection, the influence of climate patterns on Arctic sea ice, and sea ice projections are given in Section 2.4; a discussion of atmospheric circulations associated with the teleconnection patterns is given in Section 2.5; conclusions are presented in Section 2.6.

2.2 Data

Several datasets were used in this study to investigate the changes in ASI and its teleconnections with large-scale climate patterns. The data of monthly sea ice concentration (ASI) from 1979 to 2017 were downloaded from the Near-Real-Time DMSP SSMIS Daily Polar Gridded Sea Ice Concentrations and the Sea Ice Concentrations from Nimbus-7 SMMR and DMSP SSM/I-SSMIS Passive Microwave Data. This dataset is stored in the NSIDC database of monthly Sea Ice

Index, Version 3, with a spatial resolution of 25km×25km (Fetterer et al. 2017). Monthly data are grouped into seasonal data such that: summer is June-August; autumn is September-November; winter is December-February, and; spring is March-May.

The AO index is the first leading mode of the mean height anomalies at 1000-hPa, and a positive AO index means a lower than normal pressure in the Arctic. The NAO index is the leading mode from the Rotated Principal Component Analysis of the monthly standardized 500-hPa height anomalies in the region of 20°N-90°N with variability at inter-seasonal and inter-annual time scales (Bladé et al. 2012; Hurrell 1995; Hurrell and Deser 2010; Ogi et al. 2003). The PNA index is derived from the variability of opposite geopotential height anomalies centered between the Aleutian and the Hawaiian islands, with positive phases coinciding with a warmer western North America and drier western Canada (Assel 1992; Gan et al. 2007; Leathers et al. 1991; Sheridan 2003). El Niño events based on the Niño3.4 index are considered active if a 5-month running mean of SST anomalies in the Niño3.4 region of the Tropical Pacific exceeds 0.4°C for 6 months or more (Trenberth 1997). Niño3.4 was downloaded from the Climate Prediction Center of NOAA on Earth System Research Laboratory (https://www.esrl.noaa.gov/psd/data/climateindices/list/). In addition, the Pacific Decadal Oscillation (PDO), the leading pattern of sea surface temperature (SST) anomalies in the North Pacific basin (typically, polewards of 20°N; Deser and Trenberth (2016), and the Atlantic Multidecadal Oscillation (AMO), a near-global scale multidecadal climate variability with alternating warm and cool phases over large parts of the Northern Hemisphere (Enfield et al. 2001), were considered in the multivariate quantile regression model.

The composites of SST, SLP, GPH at 500-hPa, and wind speed at 500-hPa (UV) were estimated to investigate the effects of climate patterns on Arctic sea ice. Datasets for the above climate variables from 1979 to 2017 are taken from the ERA-Interim monthly dataset of 0.75°×0.75° spatial resolution (Dee et al. 2011).

2.3 Methodology

2.3.1 Quantile regression

Quantile regression has been widely used in trend analysis (Cannon 2018; Fan and Chen 2016; Gao and Franzke 2017; Malik et al. 2016; Tan et al. 2018b). Here, it is used to examine the temporal changes of sea ice extent and concentration at multiple quantiles. The teleconnection between sea ice and climate patterns are examined through quantile regression with climate indices as predictor variables, in which regression coefficients at the low (5th), median (50th), and high (95th) quantiles were extracted to represent the responses of extremely low, medium, and extremely high ice cover to the climate patterns. Moreover, multivariate quantile regression models are developed to project sea ice concentrations under the effects of different climate patterns.

Quantile regression is derived from the ordinary linear regression (OLR) model denoted as $Y_i = \beta t + \gamma$, with Y_i as the dependent variable, time t as the independent variable in temporal trend analysis, which could also be the time series of a climate pattern index, and β and γ are the slope and the y-intercept estimated from the OLR model, e.g., $Y = f(\beta, \gamma, t)$. The parameters β and γ were estimated from the traditional least-squares method by minimizing $\sum_i [y_i - f(\beta, \gamma, t)]^2$, which is essentially estimating the mean of Y conditioned on t, $E[y|t]$. However, quantile regression replaces the target function $E(y|t)$ with the quantile of Y conditioned on t, denoted as $Q[y_\tau|t]$. For a quantile τ, the quantile regression model is written as $Y = g(\beta_\tau, \gamma_\tau, t)$, where β_τ, γ_τ are the quantile slope and intercept, respectively, which can be estimated by minimizing:

$$\sum_i \rho_\tau[y_i - g(\beta_\tau, \gamma_\tau, t)] \tag{2-1}$$

where ρ_τ is the tilted absolute value function (Koenker and Hallock 2001); β_τ and γ_τ are the quantile regression coefficient vectors to be estimated and τ is the quantile level. The details of the algorithm can be found in Koenker and D'Orey (1987); Tan and Shao (2017); Tan et al. (2018b); Yu et al. (2003), and has been implemented in the R package 'quantreg' (Koenker 2018) used in this study. A detailed description of quantile regression can be found in Barbosa (2008); Buchinsky (1991); Cade and Noon (2003); Koenker and Hallock (2001).

2.3.2 Composite analysis

As climate patterns dominate the regional climate variability of a specific area, composite analysis is used to investigate the relationship, if any, between sea ice concentration and climate patterns. In this study, composite values are calculated as the difference of the climate variables (SLP, SST, GPH, and UV) in the extreme positive and negative phases of climate patterns (AO, NAO, PNA, and Niño3.4). As an example, the composite of SLP is computed from the average observations over the five lowest AO years and the five highest AO years, and are denoted SLP_{-AO} and SLP_{+AO}, respectively. The composite value of SLP, $\delta SLP_{max} = SLP_{+AO} - SLP_{-AO}$, represents the effects of AO on SLP. Bootstrap resampling is used to generate the empirical distribution of the composite values. By resampling δSLP_{max} 5000 times from the sea ice concentration time series of each grid, we can obtain an empirical distribution of δSLP_{max}, with the cumulative probability distribution function denoted as $F(\delta SLP_{max})$. If $\delta SLP_{max} \leq F^{-1}(0.025)$ or $\delta SLP_{max} \geq F^{-1}(0.975)$, the composite of SLP with respect to AO is statistically significant at the 5th level, in which $F^{-1}(0.025)$ and $F^{-1}(0.975)$ denote the 2.5th and 97.5th quantile of δSLP_{max} at the 5th significance level, respectively. Detailed descriptions and the formulae can be found in Tan et al. (2016); Zhang et al. (2010).

2.3 Results

2.3.1 Changes in Arctic Sea Ice

Figure 2-1 shows the probability density functions and the regression coefficients of seasonal ASI. The winter and spring ASI are distributed more symmetrically than summer and autumn. In other words, the probability density functions of winter and spring sea ice extent (Fig. 2-1(1)a, d) have more bell curve characteristics but those of summer and autumn (Fig. 2-1(1)b, c) tend to skew towards low sea ice extent. The slopes of the regression lines for summer and autumn sea ice extent at low and high quantile levels are steeper than they are at medium quantile levels (Fig. 2-1(3)b, c). Comparing the seasons, the average regression coefficients of summer and autumn are much larger than those of winter and spring (Fig. 2-1(2)).

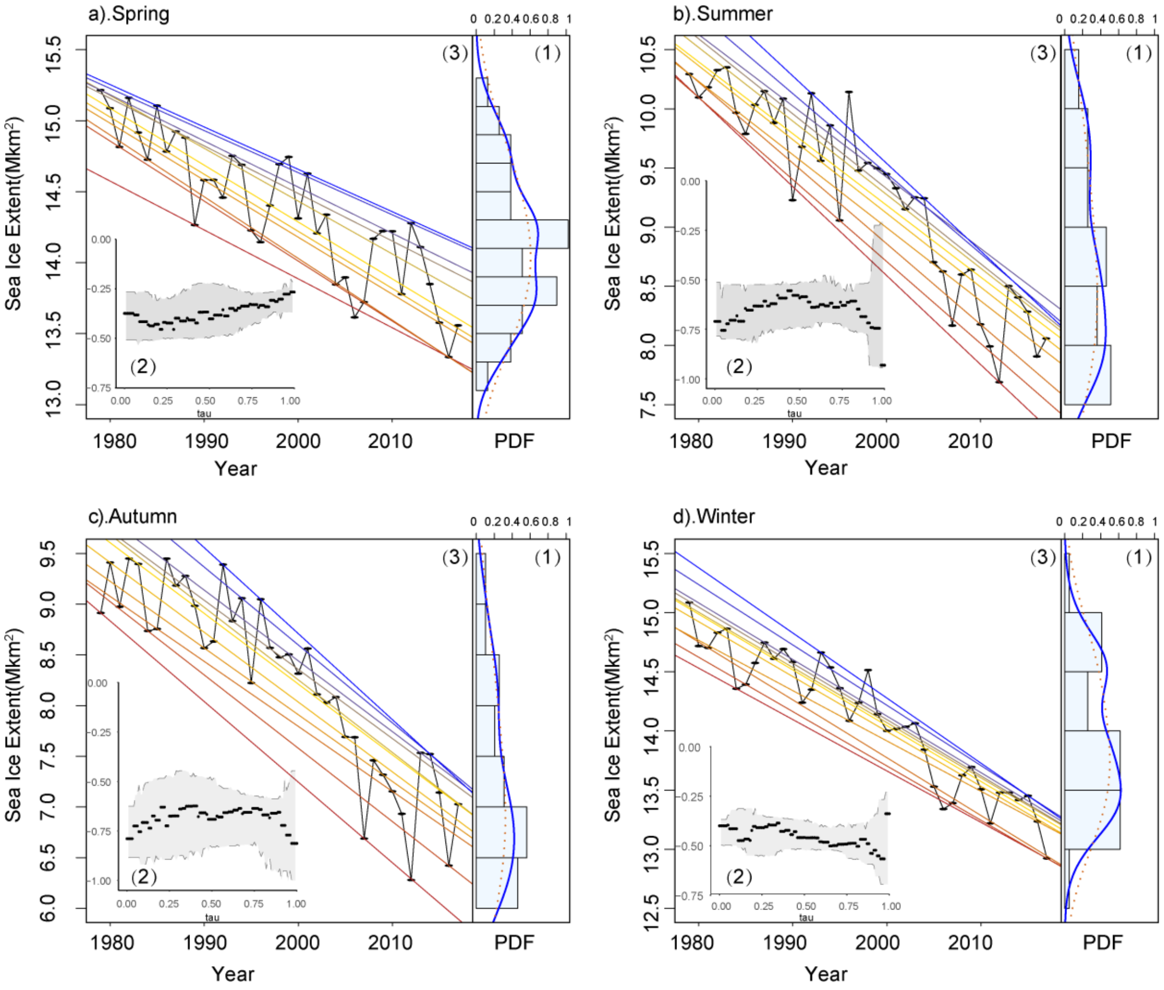

Figure 2-1. Quantile regression of seasonal Arctic sea ice extent a). spring, b). summer, c) autumn, d). winter. Within each panel, (1) is the histogram of the sea ice extent with an interval of 0.5 Million km^2 and the probability density (blue solid curve) and the adjusted normal distribution (orange dash line); (2) is the quantile regression coefficients and the confidence interval of (95th) varies with quantile levels (τ , from 0 to 1 by 1%); and (3) is the historical sea ice extent records (solid black scatter curve) and quantile regression line at 5th, 10th, 20th, 30th, 40th, 50th, 60th, 70th, 80th, 90th, 95th quantiles (from bottom to the top, from red to blue).

The regression coefficients of the gridded sea ice concentration at 5th, 50th, 95th that represent the extremely low, the medium, and the extremely high ice covers, show the spatial characteristics of changes in ASI. There are significant decreasing trends over the margins of the Arctic Ocean (Fig. 2-2), where the ice tends to be thinner and younger. The boreal summer sea ice over the Beaufort Sea westward to the Kara Sea shows decreasing trends over the study period (Fig. 2-2 f, g). Also during boreal summer, sea ice at the 95th quantile has smaller areas showing a decreasing trend (Fig. 2-2j, k) compared with the 50th quantile (Fig. 2-2f, g), while that at the 5th quantile has larger areas and regression coefficients (Fig. 2-2b, c).

During spring and winter, areas with decreasing ice concentrations are small and concentrated in the Barents Sea and the Sea of Okhotsk (Fig. 2-2e, h). The total areas with a decreasing trend in sea ice concentration do not differ much between the quantiles. However, decreasing trends of the 5th quantile in the Barents Sea were as large as 40% per decade, larger than those during the boreal summer. Based on trends of the sea ice extent, the decline of summer sea ice would be more likely to occur faster in the Chukchi Sea. Also, winter sea ice concentration in the Barents Sea is more likely to be much lower in ice concentrations than in other regions, which is in agreement with previous findings (Cavalieri and Parkinson 2012; Kay et al. 2011; Wang and Overland 2009).

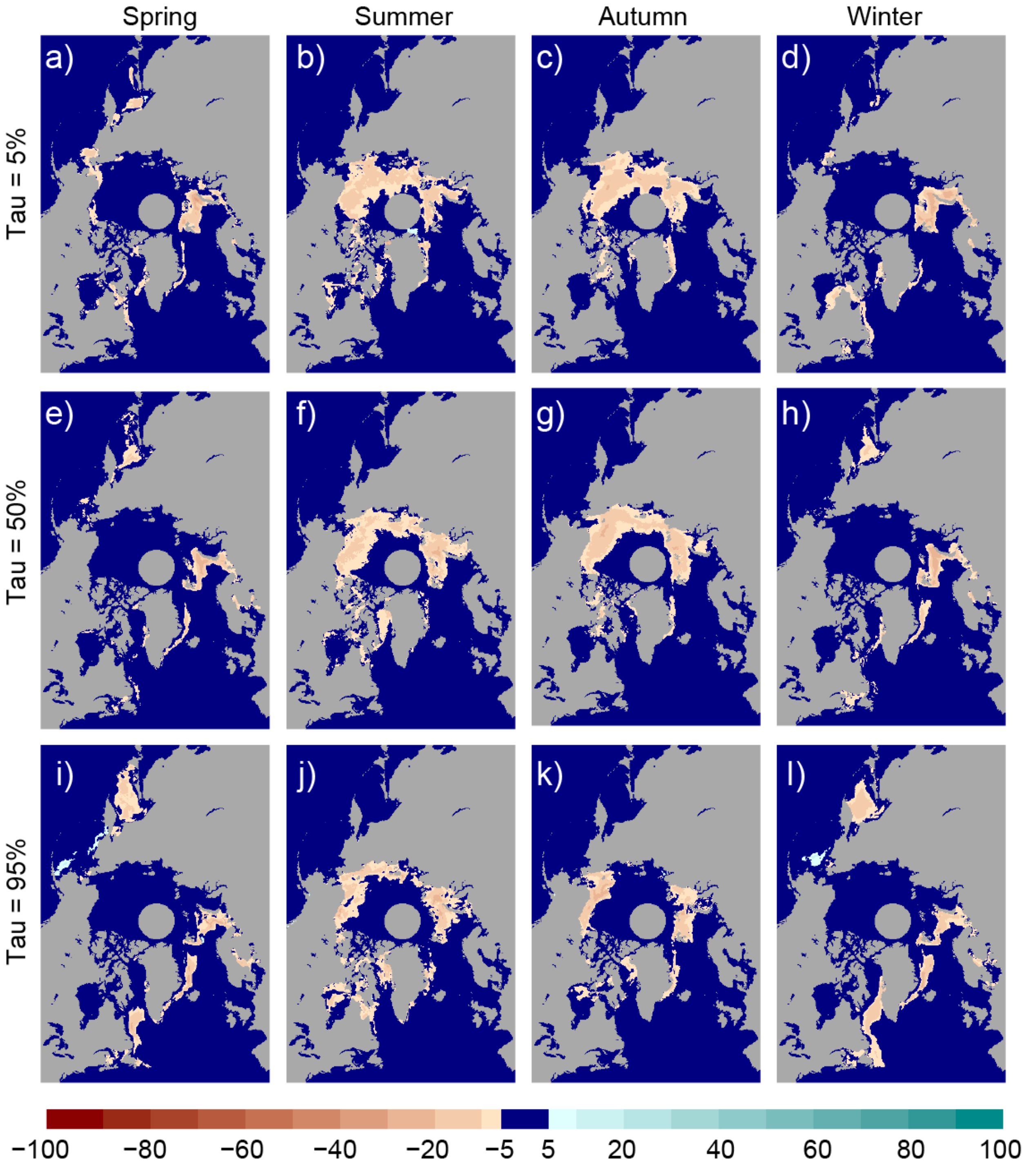

Figure 2-2. Trend coefficients (% per decade) with time as covariate derived from the classic quantile regression by quantile level and gridded sea ice concentration dataset for 1978-2016 seasonal average sea ice concentration. (a-l) spatial distribution of trend coefficients for τ =0.05 (a-d), τ =0.5 (e-h), τ= 0.95 (i-l). Columns show spring, summer, autumn and winter from left to right. Grids with the absolute trend coefficient of less than 0.5th per year are shaded in dark blue.

2.3.2 Effects of teleconnections with Climate Patterns on Arctic Sea Ice

Figures 2-3 to 2-6 show teleconnection trends by quantile levels and climate indices for seasonal sea ice concentrations. The difference in sea ice conditions between the 5th (95th) and the 50th quantiles show the difference in how sea ice covers responds to the influence of climate patterns under extremely low (high), and mean sea ice conditions.

1) Arctic Oscillation (AO)

Figure 2-3 shows the regression coefficients of sea ice concentration at the 5th, 50th, and 95th quantiles with seasonal AO indices as the covariate. During boreal winter-spring, AO has a negative relationship with the sea ice at the margins of the Arctic Ocean. Compared with the sea ice of the 50th quantile (Fig. 2-3e, h), both the 5th and 95th quantiles of sea ice concentration have larger areas that show a stronger relationship with AO, especially in the Sea of Okhotsk (Fig. 2-3i, l), Davis Strait (Fig. 2-3a, d, i, h) to Hudson Bay (Fig. 2-3d), as well as the Barents Sea (Fig. 2-3a, e, i). These regions are strongly affected by the extreme positive AO in winter, effects which the ordinary linear regression analysis underestimated (Fig. 2-3e-h). The effects of AO on the autumn sea ice concentration is also found to be strongly related to AO at the 5th and the 95th quantiles (Fig. 2-3c, k) more than the 50th (Fig. 2-3g). The 50th quantile of sea ice concentration has large areas positively correlated to the AO index in autumn (Fig. 2-3g) because both the AO index and sea ice experienced downward trends in the boreal summer-autumn of recent decades. However, the 5th quantile of sea ice in the Kara Sea and the Chukchi Sea are still negatively correlated to AO in summer (Fig. 2-3b).

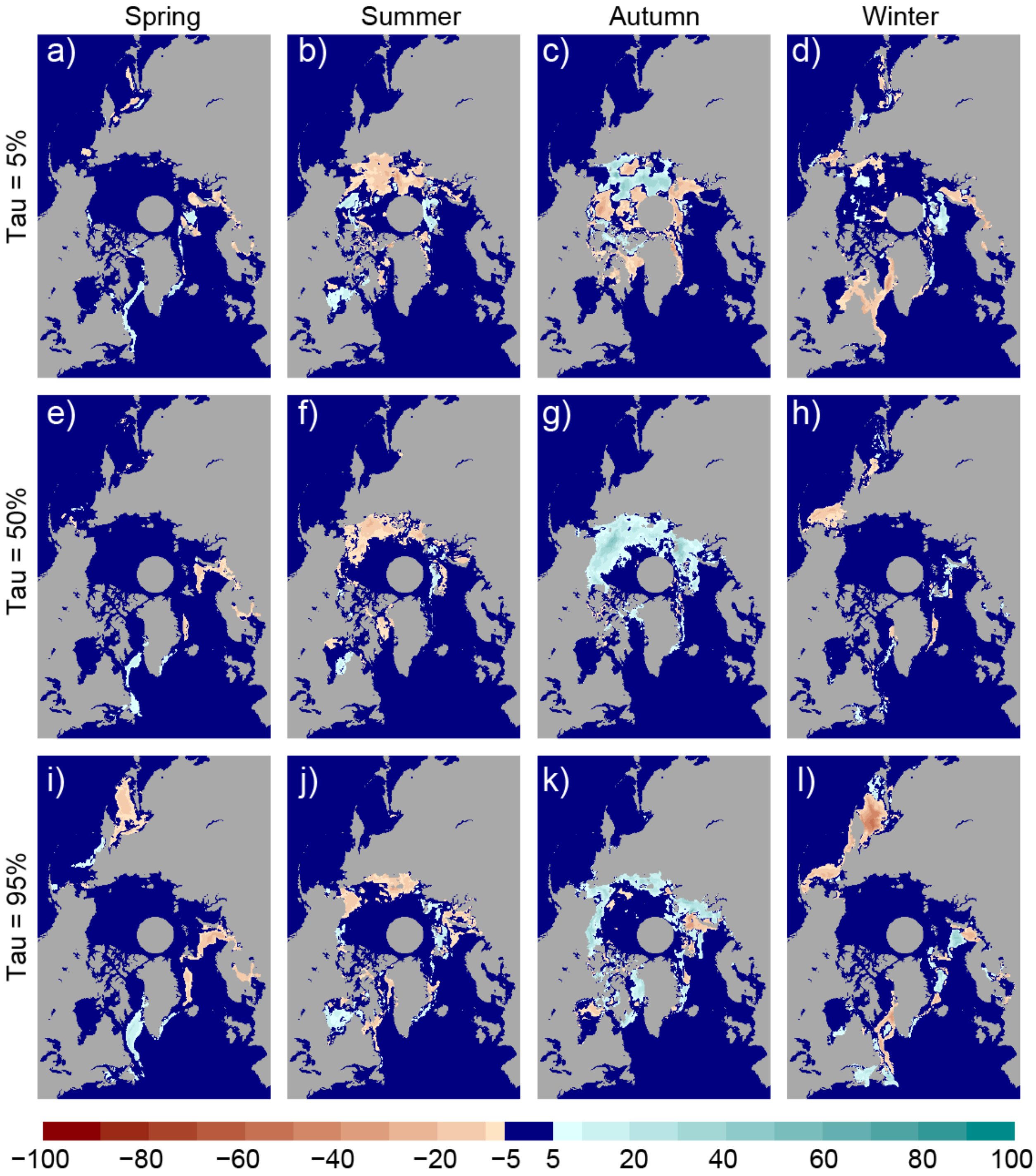

Figure 2-3, Trend coefficient (% per increasing of AO index by 1) with the AO index as covariate derived from the classic quantile regression by quantile level and gridded sea ice concentration dataset for the 1978-2016 seasonal average sea ice concentration. (a-l) spatial distribution of trend coefficients for τ =0.05 (a-d), τ =0.5 (e-h), τ= 0.95 (i-l). Columns show spring, summer, autumn and winter from left to right. Grids with the absolute trend coefficient of less than 0.5th per year are shaded in dark blue.

2) North Atlantic Oscillation (NAO)

In Figure 2-4, it was found that the responses of Arctic sea ice to NAO are different in the western and eastern Arctic Ocean at some quantiles. In boreal winter-spring when the NAO is strongest, a large area of sea ice at the 5th quantile in the Barents and Chukchi Seas has a strong negative relationship with the NAO, and that in Davis Strait it has a strong positive relationship (Fig. 2-4a, d) than at the 50th quantile (Fig. 2-4e, h). Sea ice at the 95th quantile of the Sea of Okhotsk and the Barents Sea has a significant decreasing trend with the NAO index. Again, the results show that modeling the sea ice concentration with the NAO index as the covariate would underestimate the decreasing trend in these regions. A large area of summer sea ice has a positive relationship with the NAO index (Fig. 2-4f), which may be partly due to the downward trend of the summer NAO itself in recent decades. In autumn, the relationship between NAO and sea ice at low quantile sea ice is negative on the East Siberian Sea but positive on the other regions (Fig.2-4c).

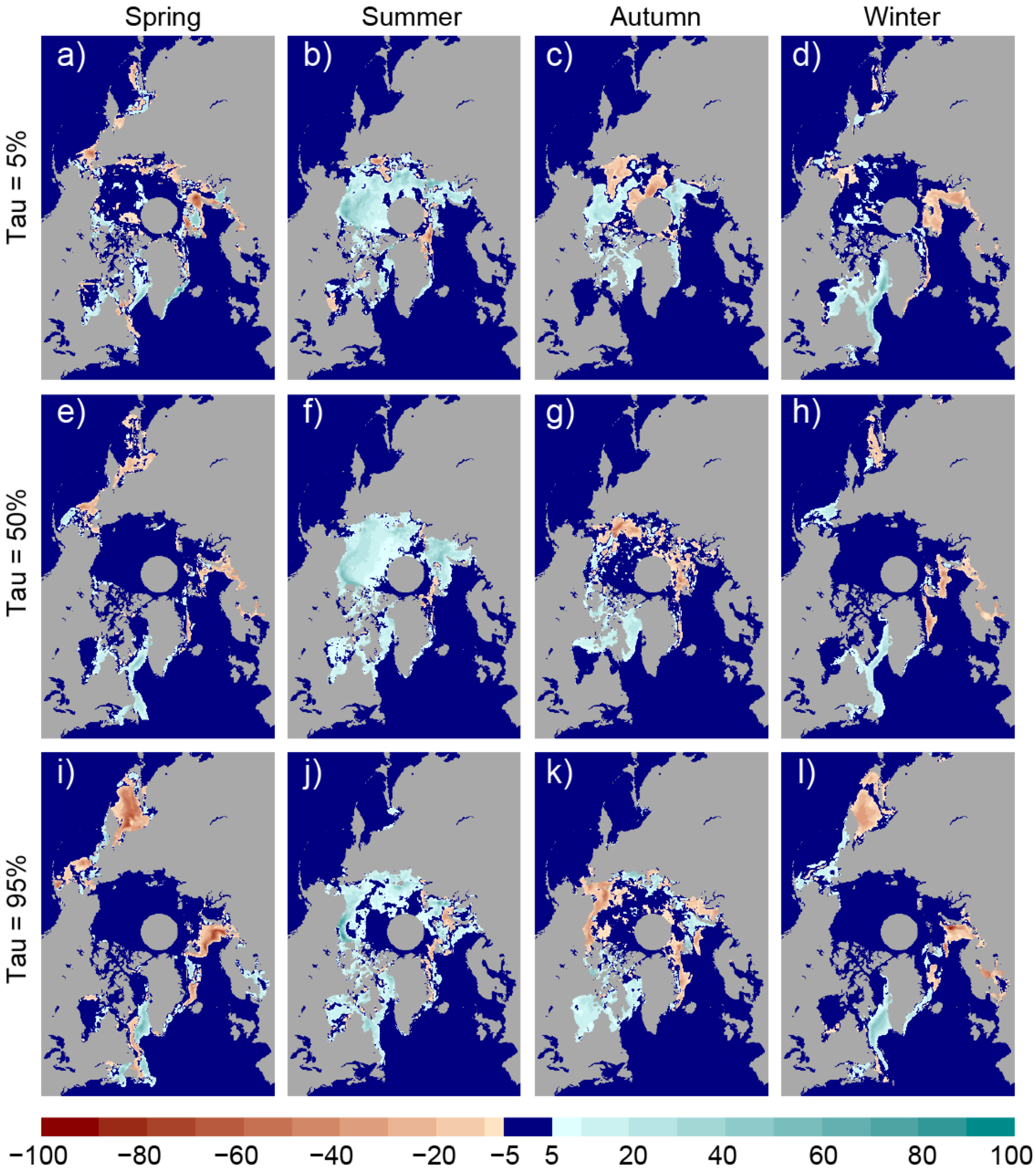

Figure 2-4. Same as Fig. 2-3, but for the NAO index.

3) Pacific North American Pattern (PNA)

Figure 2-5 shows the regression coefficients between Arctic sea ice with PNA as the covariate. From the coefficients of the 50th quantile, it is evident that a large area of summer and autumn sea ice from the Beaufort Sea westward to the north of Barents Sea has a negative relationship with the PNA (Fig. 2-5f, g), and this result agrees with the findings of L'Heureux et al. (2008). In the 5th quantile, the decreasing trend in the Chukchi Sea is strong, but the trends are positive in the Beaufort and Laptev Seas (Fig. 2-5b, c). These summer and autumn spatially distributed regression coefficients imply that a strong positive PNA phase may lead to summer and autumn sea ice loss in the Chukchi Sea, but not so in the Beaufort and Laptev Seas. In winter, sea ice in the Barents Sea has a strong negative relationship with PNA at the 5th and 95th quantiles (Fig. 2-1d, l) but does not have any significant relationship with PNA at the 50th quantile (Fig . 2-5h).

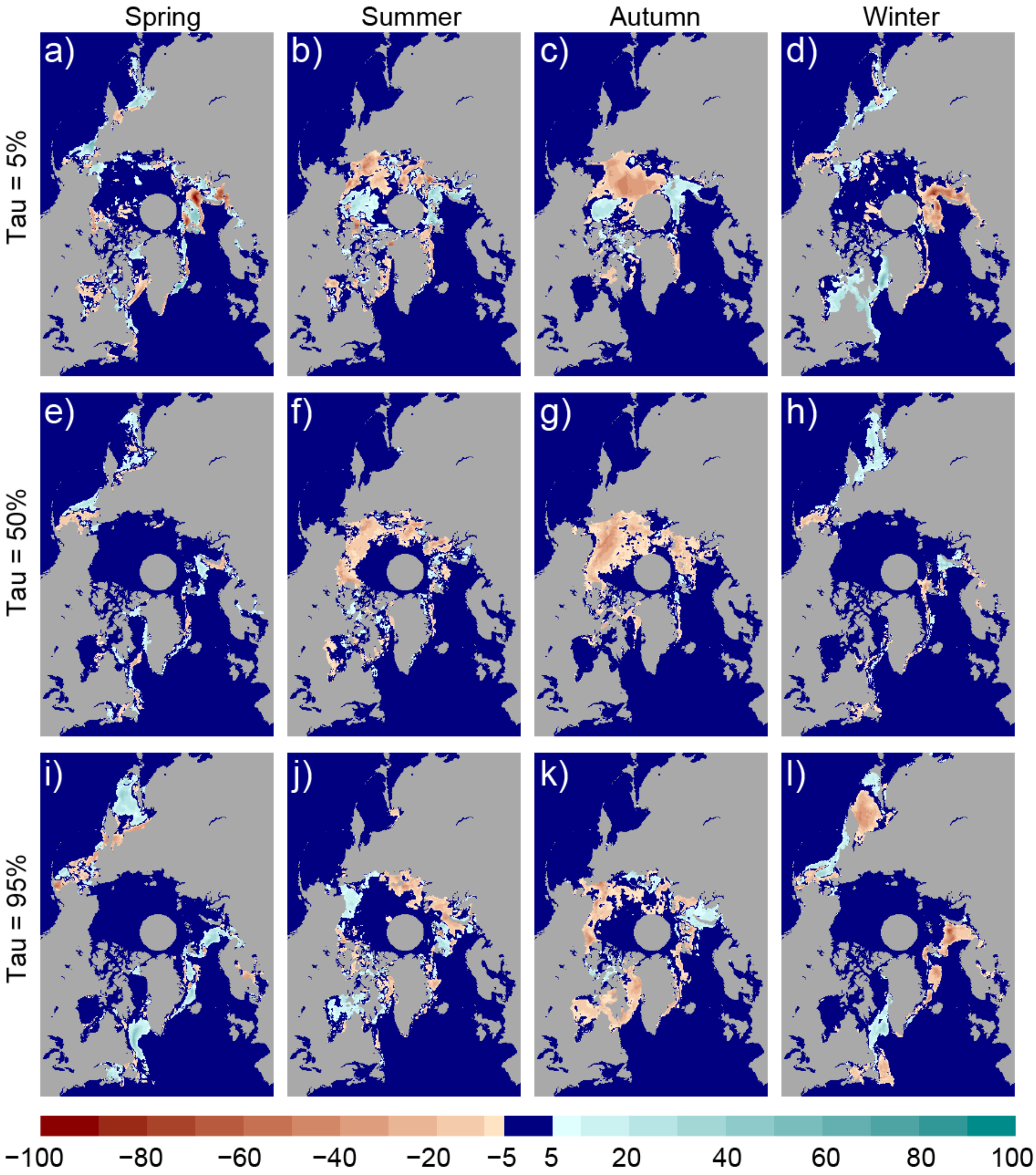

Figure 2-5. Same as Fig. 2-3, but for the PNA index

4) ENSO

ENSO, which originates from the tropical Pacific, has a weaker relationship with Arctic sea ice than other climate patterns (Fig. 2-6). From the west of Beaufort Sea westward to the East Siberian Sea, sea ice is positively related to Niño 3.4 at low quantiles in summer and autumn (Fig. 2-6b, c), while at the 95th quantile, the coastal sea ice is found to be negatively related to Niño 3.4. There is very little relationship between sea ice and ENSO at the 50th quantile, regardless of season.

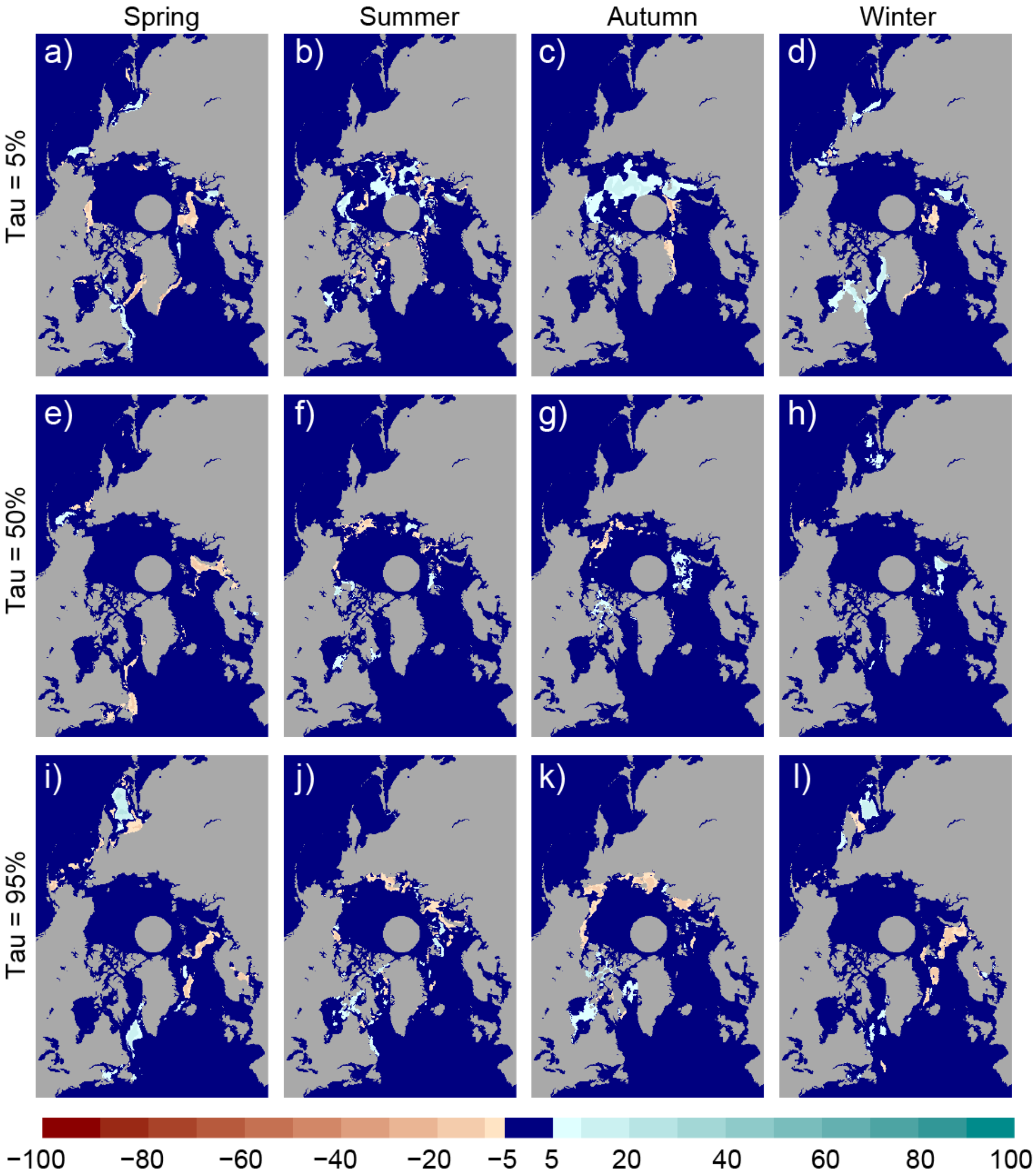

Figure 2-6. Same as Fig. 2-3, but for the Niño 3.4 index

2.3.2 Effects of Combined Climate Patterns on Arctic Sea Ice

ASI is teleconnected to climate patterns in a much more complex manner than a simple linear, univariate correlation. From the above univariate quantile regressions, we found that the AO and NAO have similar relationships with ASI, while the relationships with PNA and ENSO are progressively weaker. Therefore, a multivariable quantile regression model was used to project the effects of combined climate patterns on the extremely low sea ice concentrations. Since the AMO and PDO are found to be non-linearly related to the Arctic (Zhang et al. 2018), the model also considers the AMO and PDO as in-phase with each other according to their phase relationship (Li et al. 2016a; McCabe et al. 2004). The 95th and 5th quantiles of the climate indices were chosen arbitrarily to represent the extremely positive and negative phases of the climate patterns. The projected anomalies of sea ice concentration under the extreme phases of climate patterns, minus the long-term averages (1979-2018), are presented in Figure 2-7.

The spring and winter sea ice concentration anomalies under +AO/+NAO are found to be lower than the multiyear average (Fig. 2-7a1, b1) as expected. When AMO and PDO are both in the extremely positive phase at the same time with +AO/+NAO, the sea ice concentration is lower (Fig. 2-7a2, b2). Similar conditions in sea ice concentrations are found during boreal summer with active PNA and ENSO. The summer and autumn sea ice concentration is slightly lower than the multiyear average with extremely positive PNA and El Niño (Fig. 2-7c1, d1). Combined with simultaneously positive AMO and PDO, the summer and autumn sea ice concentration tends to be lower than with only a positive PNA or a positive El Niño (Fig. 2-7c2, d2). These findings indicate that the extremely positive AMO and PDO can further enhance the negative relationships between winter ASI with AO/NAO, and for summer ASI with PNA/ENSO.

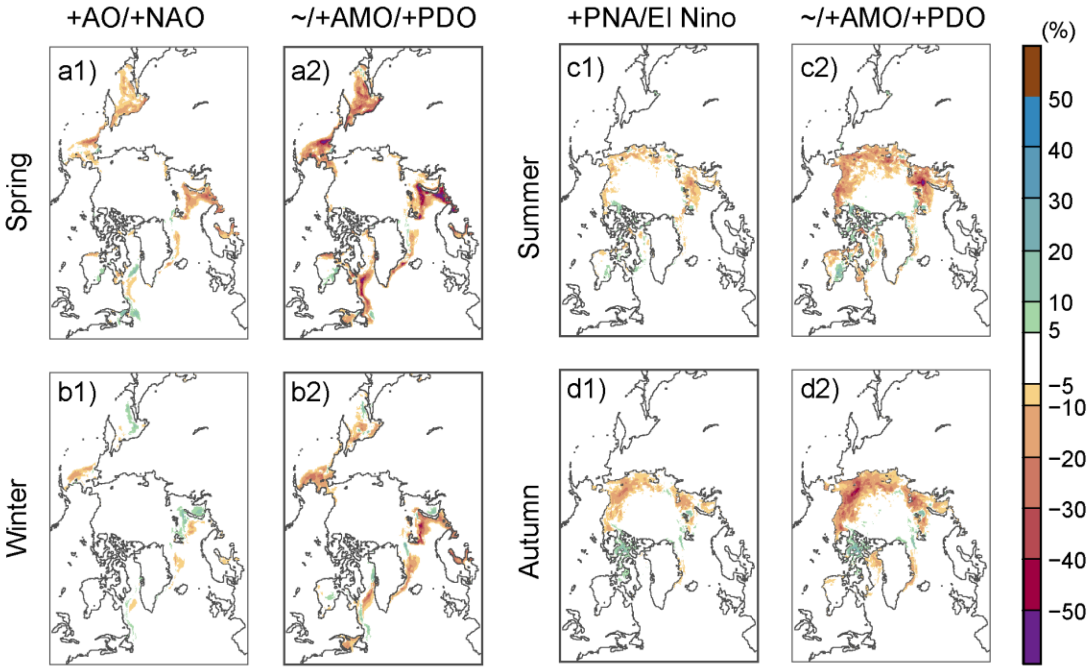

Figure 2-7. The seasonal sea ice anomalies projected by the multi-variate quantile regression. For spring (a1) and winter (b1) sea ice under concurrently positive AO and NAO, while the summer (c1) and autumn (d1) sea ice under concurrently positive PNA and El Nino. The seasonal sea ice was projected with additionally positive AMO (95th quantile) and positive PDO (95th quantile) (*2).

2.4 Discussion

Since strong relationships between large-scale climate variability and ASI quantiles have here been quantified, the seasonal influence of climate patterns under positive and negative phases on ASI was further investigated. The atmospheric circulation mechanisms that may give rise to the teleconnection patterns observed between ASI and AO, NAO, PNA, and ENSO over 1978-2017 were analyzed by a composite analysis of climate variables, respectively.

2.4.1 Atmospheric circulation mechanisms for the teleconnection with AO

The composite results show that the sea level pressure (SLP) over Asia, the western Siberian Sea, and the Chukchi Sea tends to be lower during positive AO boreal winters, resulting in a northerly wind that brings cold and dry air to Asia (Fig. 2-8b1).

Although AO has a relatively weak temporal variability in winters, quantile regression shows that there is a complex spatially-distributed response of ASI to AO in summer (cf. Fig. 2-3f, g). The composite analysis of climate variability also demonstrates this teleconnection. Lower SST and GPH over the North Pacific and North Atlantic Ocean during a positive AO phase favors the growth of ASI. On the other hand, SLP over the Arctic is higher during negative AO than during positive AO, and the former favors clear sky conditions. Less cloud cover allows more downwelling shortwave radiative fluxes that enhance surface (and potentially basal) melting of ASI (Kay et al. 2008). The wind field composite shows dominant anticlockwise wind anomalies over the Arctic Ocean during positive AO autumns that could promote sea ice export through Fram Strait, resulting in less Arctic sea ice.

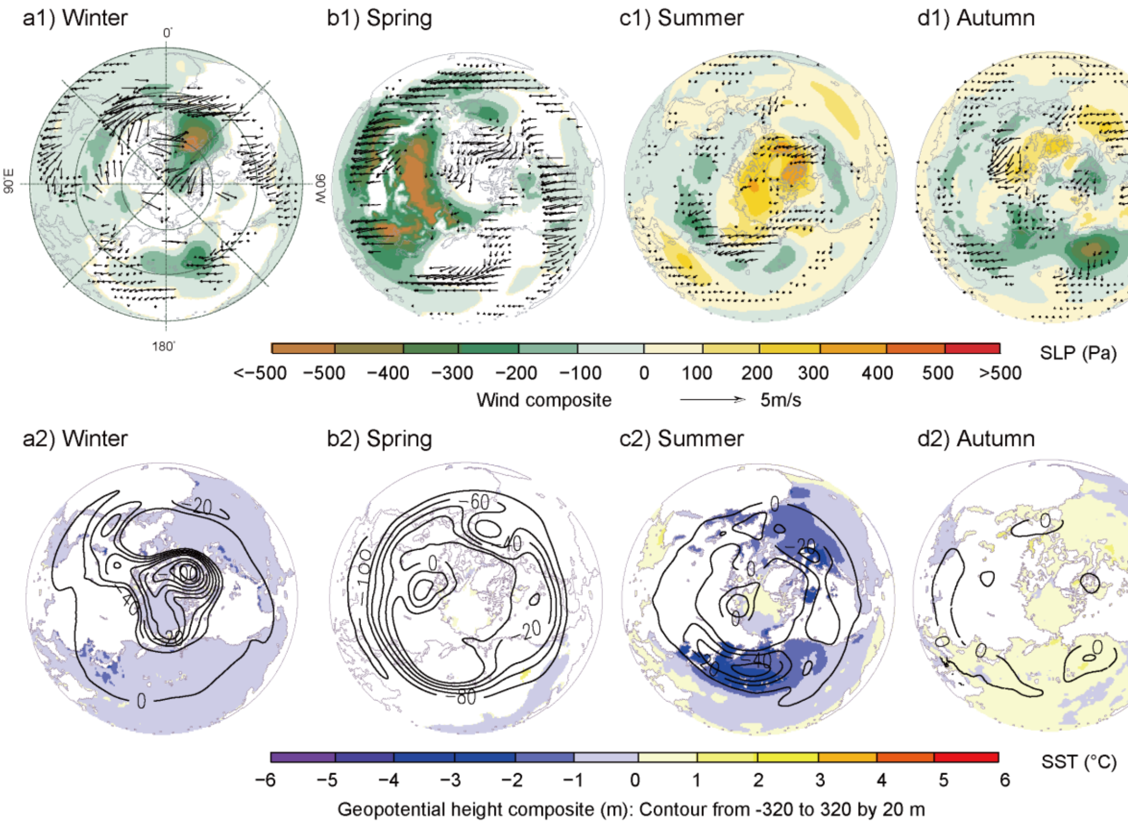

Figure 2-8. Composite of winter (a1,a2), spring(b1,b2), summer(c1, c2), autumn (d1, d2) sea level pressure (Pa) (*1), 500-hPa wind field (m/s; vectors) (*1), 500-hPa geopotential height (m; contour with numbers)(*2), and surface air temperature (°C; shaded) (*2) during years with extremely high (positive) and low (negative) phases values of the AO index.

2.4.2 Atmospheric circulation mechanisms for the teleconnection with NAO

As predicted by the quantile regression, seasonal sea ice over the Labrador Sea and north of Greenland is higher under positive NAO (cf. Fig. 2-4a, d) due to the enhanced southerly winds (Fig. 2-9a1, b1), which is consistent with the findings of Hurrell and Deser (2010). Sea ice in the Barents Sea is lower during strong positive NAO winters and springs (cf. Fig. 2-4a, d, e, h, i, l). Ottersen and Stenseth (2001) found that the NAO, SST in the Barents Sea, and inflow from the Atlantic are interrelated as proposed by ÅDlandsvik and Loeng (1991): under a positive NAO phase, there is a strong Icelandic low (Fig. 2-9a1) and enhanced cyclonic circulation that increases the inflow of warm water into the Barents Sea (Fig. 2-9a2, b2), which in-turn enhances upwelling heat fluxes and induces low SLP. However, under a positive NAO summer, the SLP over the Arctic region tends to be higher (Fig. 2-9c1), which leads to anticyclonic circulation anomalies over the Arctic Ocean that favor a low sea ice extent through ice export (Stroeve et al. 2016).

Sea ice concentration over the Eastern Siberian and the Chukchi Seas tends to be lower during positive NAO autumns (cf. Fig. 2-4c, g, k), and is attributed to the near-surface anticyclonic wind over the Arctic. Since the summers of 2007, low-level circulations over the Arctic has been much more anticyclonic than in prior years for unknown reasons (Ogi and Wallace 2012). The effects of the NAO on boreal summer sea ice is complicated for there are multiple mechanisms at play. This complex interplay warrants further research.

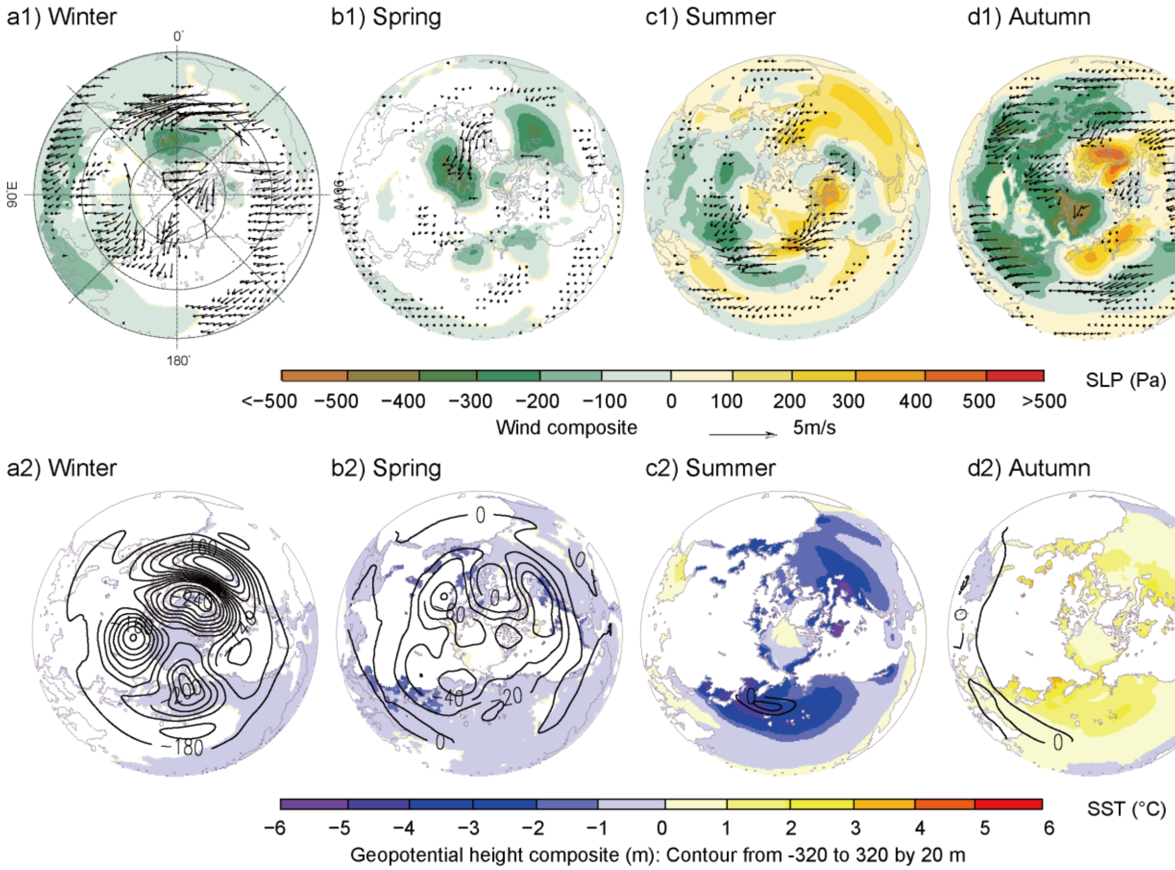

Figure 2-9. Same as Fig. 2-8, but for the NAO index.

2.4.3 Atmospheric circulation mechanisms for the teleconnection with PNA

The composite analysis of the seasonal wind fields show a strong anticyclone over the Laptev and Barents Seas during positive PNA years (Fig. 2-10a1, b1, c1, d1) that drives the Arctic sea ice to the Atlantic, resulting in reduced ASI. A positive PNA also enhances poleward shifting waves with alternating centers of anomalous pressure that turn northeastward over the North Pacific Ocean, over western-central Canada, and then southeastward over central-eastern North America. This circulation pattern increases heat intrusion to the Arctic (L'Heureux et al. 2008), which may lead to the earlier onset of ASI melting by ~2-3 days per decade (Wang et al. 2013). The strong high pressure over the Chukchi Sea (Fig. 2-10d1) during positive PNA autumns leads to strong southerly winds through the Bering Strait, resulting in less Arctic sea ice, giving rise to a negative relationship between ASI and the PNA index (cf. Fig. 2-5c, g, k).

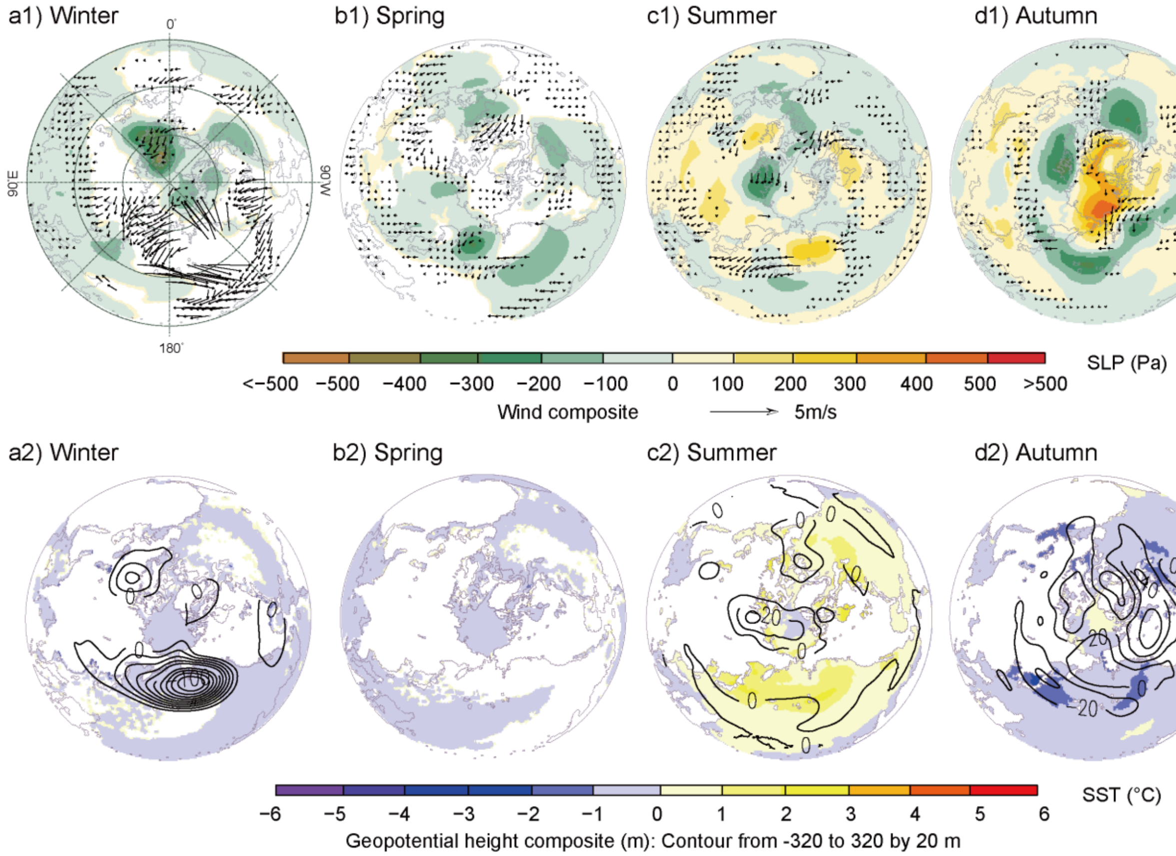

Figure 2-10. Same as Fig. 2-8, but for the PNA index.

2.4.2 Atmospheric circulation mechanisms for the teleconnection with ENSO

The quantile regression coefficients between ASI and Niño 3.4 are relatively modest compared to those for AO, NAO, and PNA, which may be partly because ENSO needs more time to teleconnect with the ASI (Hyo-seok et al. 2015). Furthermore, the atmospheric circulation is significantly different during El Niño and La Niña episodes, and the average Arctic SST during winter tends to be colder during El Niño but warmer during La Niña events (Fig. 2-11a2), as shown by Lee (2012).

During strong El Niño winters, there is an enhanced low pressure over Iceland and a strong anticyclone over the Laptev and Barents Seas (Fig. 2-11a1). Liu et al. (2004) found that ENSO has similar effects on the Eastern Arctic as the AO, in that sea ice expands during the negative phase (La Niña) and shrinks during the positive phase (El Niño), while the Western Arctic sea ice shrinks during La Niña but expands during El Niño. In autumn, the strong low pressure over the Barents Sea and high pressure over southern Greenland favors a strong southward wind through Fram Strait (Fig. 2-11d1), which may accelerate the export of sea ice to the North Atlantic.

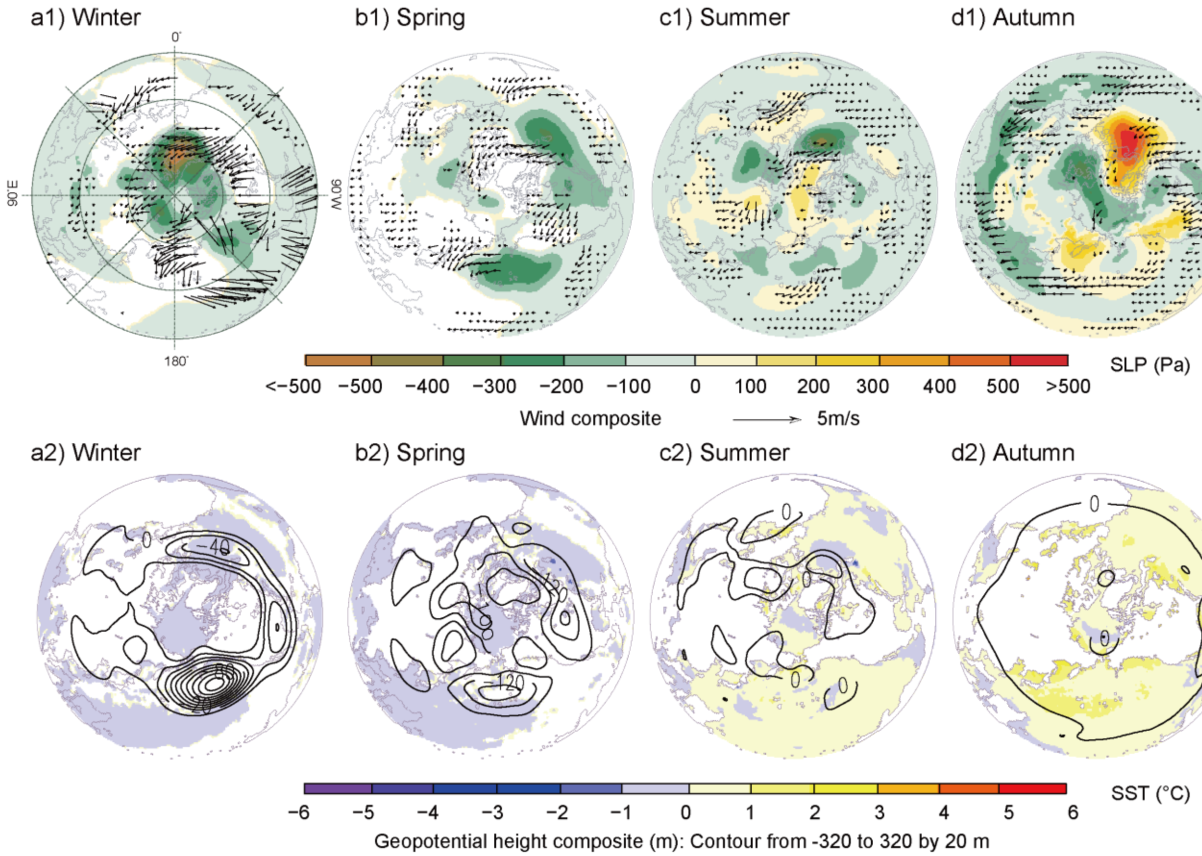

Figure 2-11. Same as Fig. 2-8 but for the Niño 3.4 index.

2.5 Conclusions

This study extends the application of quantile regression to the problem of Arctic sea ice variability and the co-variability of sea ice with climate patterns. Through this new analysis technique, the trends of Arctic sea ice are determined to be that the sea ice of low quantiles decreases faster than the average, especially in most areas of the Beaufort Sea westward to the Kara Sea. Arctic sea ice of low quantiles is also found to have stronger teleconnections with climate patterns than the average. A projection of Arctic sea ice through a multivariate quantile regression model demonstrates that particular combined climate patterns have a stronger influence on Arctic sea ice than an individual climate pattern. The physical mechanisms behind these teleconnections were investigated through a composite analysis of climate variables (SLP, SST, GPH, UV). The significantly different climate variables under the influence of extreme positive and negative phases of the respective climate indices reveals the existence of forcing mechanisms behind the teleconnections between Arctic sea ice and the climate patterns. These findings aim to improve the understanding of Arctic sea ice variability, and its complex relationship with large-scale climate patterns and, hopefully, benefit the prediction of Arctic sea ice.

Chapter 3. Non-stationarity of the streamflow of major northern river basins of Siberia at multi-time-scales and its teleconnection with climate patterns

3.1 Introduction

As the warming of climate continues since the mid-Twentieth Century, hydrologic changes have been detected in river basins worldwide, including Arctic river basins. The discharge of Arctic rivers contributes more than one third of freshwater into the Arctic Ocean (Rachold et al. 2004), which affects the salinity stratification (McPhee et al. 1998), sea ice formation (White et al. 2007), and oceanic thermohaline circulation (Bintanja et al. 2018; Kattsov et al. 2007), which together constitute an essential linkage with the heat and mass balance of the Arctic atmosphere.

Recent studies show an increasing trend in the discharge of most northern rivers, including the largest Arctic rivers in Siberia, especially in winter and spring, over recent decades (McClelland et al. 2006; Peterson et al. 2006; Peterson et al. 2002; Rood et al. 2017; Serreze and Etringer 2003; Su et al. 2018; Ye et al. 2003). Under a warmer Arctic atmosphere, the hydrologic cycle becomes more intensive (Déry et al. 2009), resulting in a wetter and warmer atmosphere, widely observed permafrost degradation, greening vegetation, more severe hydrologic extremes (Bring et al. 2016; Dirmeyer et al. 2013; Elmendorf et al. 2012; Han et al. 2018; Macias-Fauria et al. 2012; Tape et al. 2006; Wagner et al. 2011), higher groundwater storage (Reginald and Vladimir 2009), subsurface flow connectivity enhancement (Walvoord and Kurylyk 2016; Watson et al. 2013), shorter snow-cover duration and less maximum winter snow storage in mountainous Siberia (Bulygina et al. 2009), more forest fires resulting from increasing summer dryness (Groisman et al. 2007) and higher active layer moisture storage (Smith et al. 2007). Changes of river streamflow is significantly affected by increasing precipitation and land surface changes (Nijssen et al. 2001a; Nijssen et al. 2001b; Serreze et al. 2002b; Yang et al. 2003; Yang et al. 2002), with a higher discharge rate (Peterson et al. 2002; Zhang et al. 2012) and different spatial-temporal distributions of flow patterns.

Non-stationarity means the statistical properties of a time series represented by parameters of the probability distribution of the time series varies with time. It has been widely observed that under the influence of global warming and anthropogenic activities, we can no longer assume hydrologic processes of river basins to be stationary over time. Therefore, non-stationary analysis has been widely conducted in river basins under the influence of significant human activities (Kyselý et al. 2010; Laurent and Parey 2007; Li and Tan 2015; Tan and Gan 2016). The presence of non-stationarity in hydrologic processes could increase the risk of flooding in flood plains, and infrastructure design could become obsolete because underlying forcing mechanisms have shifted, resulting in changes that are beyond what have been previously considered to be natural variations (Milly et al. 2008).

In northern Eurasia, which has historically had little human activity, non-stationary analyses have rarely been conducted (Su et al. 2018; Xu et al. 2020). From studies conducted in the early 2000s about the streamflow variance of Siberian river basins, researchers detected an increase in streamflow and human activities, (such as dam regulation and industrial and agricultural water use) and show modified monthly and seasonal streamflows (Berezovskaya et al. 2004; Fukutomi et al. 2003; Yang et al. 2004a; Yang et al. 2004b; Yang et al. 2003; Yang et al. 2002; Ye et al. 2003). Partly due to limited observations, so far only a few studies have been conducted to address recent changes in the hydrologic regimes of Siberian river basins (Tananaev et al. 2016; Yamamoto-Kawai et al. 2009).

Besides climate change, climate patterns could also influence hydrologic processes of northern river basins. For example, the sea level pressure over Siberia is significantly influenced by the Arctic Oscillation (AO), the Pacific/North America Pattern, and ENSO (Zhang et al. 2020). In Siberia, when the winter AO is in its positive phase, both the winter Siberian High and the East Asian winter monsoon tend to be weaker than normal (Bingyi and Jia 2002). Under the positive phase of AO, temperature tends to be higher, while eastern Siberia tends to be drier when El Niño is in its positive phase (Balzter et al. 2007). The temperature and precipitation of Siberia are negatively correlated with the Siberian High central intensity (Gong and Ho 2002).

The objective of this study is to comprehensively analyze the non-stationary characteristics of streamflow in major Siberian river basins, namely, the Ob, Yenisei, and Lena river basins at multi-time-scales and to determine the possible teleconnections with climate patterns. In this study, the MK test is used to estimate the trends of streamflow and the effects of auto-correlation and long-term-persistence are also investigated using the Hurst test. A wavelet coherence analysis is used to investigate the influence of climate patterns (including the AO, PNA, NP, and ENSO) on the streamflow of these river basins (Gan et al. 2007).

This paper is organized as follows: The streamflow data and large-scale climate patterns are described in section 3.2; the technical details of the Mann-Kendall (MK) test analysis, change point detection, and wavelet analysis are described in section 3.3; trend detection, auto-correlation, long-term persistence, change points, and the correlation with climate patterns through wavelet analysis are given in section 3.4; discussion of trend analysis associated with hydrologic changes and teleconnection patterns are given in section 3.5; and conclusions in section 3.6.

3.2 Data

3.2.1 Study area and streamflow data

The study sites selected are the three largest river basins of Siberia: Ob River Basin (ORB), Yenisei River Basin (YRB), and Lena River Basin (LRB). Lena River, the easternmost of the three Siberian rivers, originates from the Baikal Mountains south of the Central Siberian Plateau and flows northeast into the Laptev Sea. Yenisei River, the largest river flowing into the Arctic Ocean, originates from Mongolia, and flows through Lake Baikal and ends in the Kara Sea. Ob River is the westernmost of the three Siberian rivers, and originates from the Altay Mountains and flows into the Kara Sea. These three rivers contribute more than one third of the total freshwater discharge into the Arctic Ocean. Therefore, hydrologic changes in these key northern river basins due to climate warming and teleconnections with climate patterns will have significant implications to water and energy fluxes in the Arctic. Their location and the surrounding topography are shown in Fig. 3-1 and a summary of the surrounding land surface type is given in Table 3-1.

The river discharge of Siberian regions has been observed systematically, and the observed data have been quality controlled and archived by the Russian Hydrometeorological Services (Shiklomanov et al. 2000). The 1936 to 1999 streamflow data are available from the R-ArcticNet (v. 2.0) (Regional Hydrographic Data Network for the Pan-Arctic Region) in CD-ROM (Lammers et al. 2016). Most stations have records ending around 1999. A total of 160 stations within the river basins with more than 30 years of continuous monthly streamflow observations were chosen in this study. Detailed information about these stations are summarized in Supplementary 1. In addition, daily streamflow for the basins have been collected continually until now under the direction of the Arctic and Antarctic Research Institute, and they are available from ArcGRO

(Shiklomanov 2018). The streamflow of YRB were measured at 67.43°N, 86.48°E from 01/1936 to 12/2018; the streamflow of LRB measured at 70.68°N, 127.39°E from 01/1935/01 to 2018/12; the streamflow of ORB measured at 66.63°N, 66.60°E from 01/1930 to 12/2018. The data used to detect the change points of the river basin discharge are monthly and seasonal streamflow of each river basin from stations located within the river basin boundary.

Due to low population and slow economic development in northern, high-latitude areas of the Arctic, human impacts tend to be minor compared with low and mid-latitude areas (Vörösmarty and Sahagian 2000). The total water consumption in major river basins of Siberia subjected to the largest anthropogenic impact is unlikely to produce noticeable effects on the streamflow into the Arctic Ocean (Shiklomanov 1997; Shiklomanov et al. 2000; Yang et al. 2004a).

Table 3-1. Summary of three large Siberian river basins

	Area (10^3 km^2)	Length (km)	Mean Annual Runoff** (km^3)	Permafrost Extent	Land Types (%)				
					Cropland	Forest	Wetland	Grassland	Others
ORB	2975	3650	402	4%-10%	36	30	11	10	13
YRB	2554	3487	573	36%-55%	13	49	3	18	18
LRB	2430	4400	524	78%-93%	2	84	1	3	10

*Data from (Yang et al. 2004a; Yang et al. 2004b; Yang et al. 2002; Ye et al. 2003)

** The mean annual runoff of ORB, YRB, and LRB are from 7142 stations, 6656 stations, and 6342 stations, located from the outlets of respectively. Information of stations are listed in Appendix 1

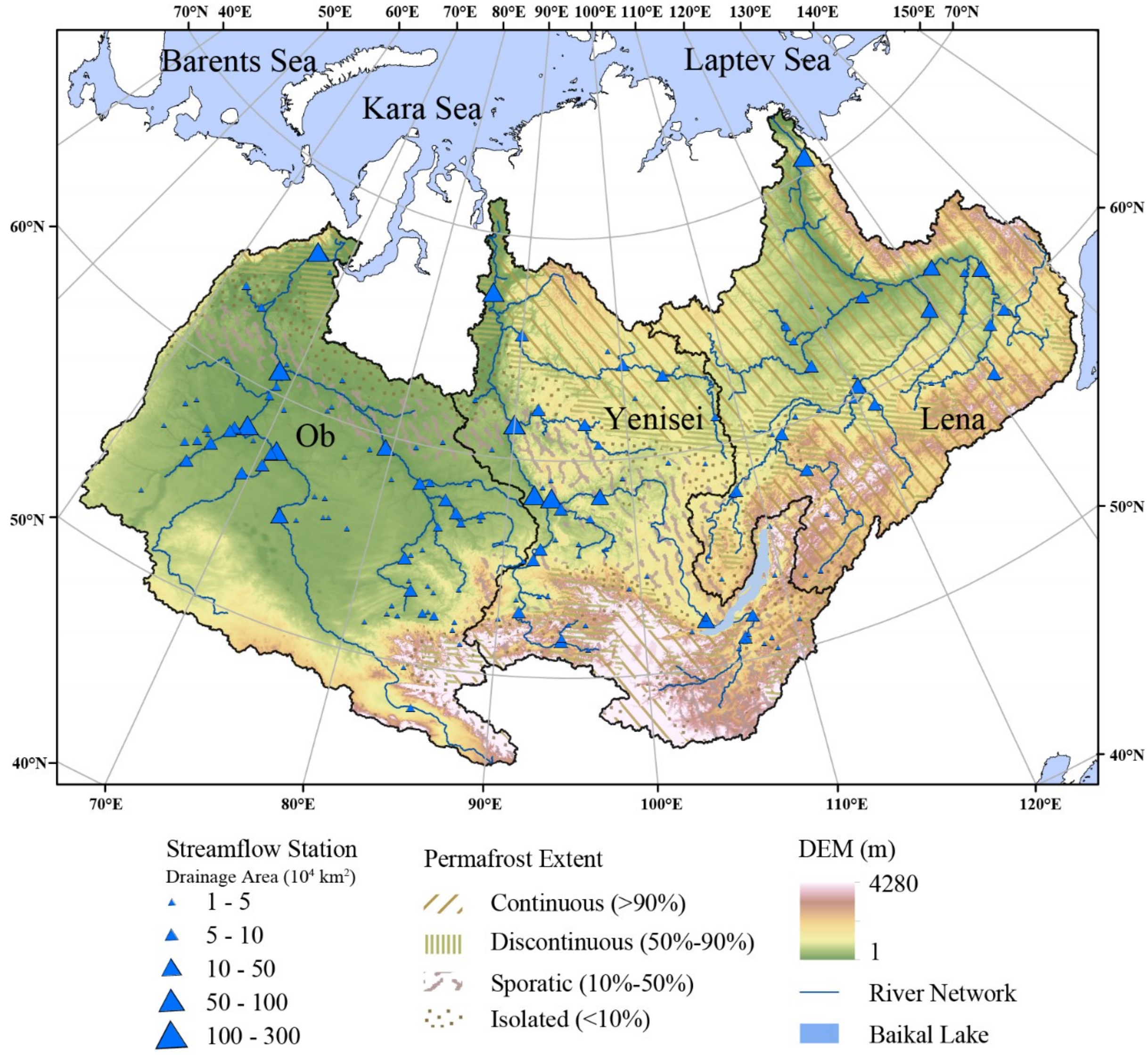

Figure 3-1. Geophysical location of the study area, the distribution and drainage area of streamflow stations, and the permafrost extent of Ob, Yenisei, and Lena river basin. The station information is listed in Appendix 1

3.2.2 Climate Indices

We investigated possible teleconnections between streamflow of three Siberian river basins and the Arctic Oscillation (AO), the North Pacific Oscillation (NP), the Pacific/North American Pattern (PNA), and ENSO based on correlations estimated between deseasonal monthly river discharge with the long-term monthly average discharge removed and divided by the standard deviation of the long-term discharge of the month and these climate indices. The AO index represents the first leading mode of the mean geopotential height anomalies at 1000 hPa, with a positive index representing a lower than normal pressure over the Arctic. The NP is defined in terms of opposition in sign of mean temperature anomaly between western Alaska-eastern Siberia and western Canada (Rogers 1981). The PNA index represents the variability of opposite geopotential height anomalies centered between the Aleutian and the Hawaiian islands. A positive phase of PNA coincides with a lower autumn sea level pressure over Northern Eurasia in autumn (Zhang et al. 2020). ENSO (El Niño) represented by the Niño3.4 index is considered active if a 5-month running mean sea surface temperature anomalies in the Niño 3.4 region of the Tropical Pacific exceeds 0.4°C for 6 months or more (Trenberth 1997). Climate indices were downloaded from the Global Climate Observing System, https://www.esrl.noaa.gov/psd/gcos_wgsp/Timeseries/.

3.3 Research Methodology

3.3.1 Temporal Trend Analysis

The Mann-Kendall (MK) test (Kendall 1955), the most popular and rank-based, nonparametric test for temporal trends, is chosen to estimate trends in precipitation and streamflow time series of pan-Arctic basins. However, the significance of the trend of a time series with a positive (negative) auto-correlation may be overestimated (underestimated) (von Storch 1999). The lag-1 auto correlation (AR1) is the correlation between values that are one time period part. Therefore, the “trend-free pre-whitening” (TFPW) procedure will be applied to remove any short-term serial correlation (Yue et al. 2002). Meanwhile, the presence of long-term persistence (LTP) may lead to an underestimation of the auto-correlation but an over-estimation of the probability that the MK test detects a significant trend (Cohn and Lins 2005; Su et al. 2018). LTP indicates long-term autocorrelation in a time series, or the presence of long-term variability in the background climatic environment, and can be used as a "fingerprint" in hydrologic or climate models for re-constructing a time series (Koutsoyiannis and Montanari 2007). The LTP of a time series, which can be shown by its scaling and fractal properties that describe the self-similar behavior over a certain range, is also related to deterministic trends or change points of that time series. Thus the LTP properties of precipitation and streamflow can be represented by the Hurst exponent H (Hurst 1951), which ranges from 0 to 1, such that $H < 0.5$ shows a lack of LTP, while $H > 0.5$ shows the presence of LTP. Thus, a modified MK test will be also used to detect the trend of a time series with its LTP estimated from the Hurst exponent (Hamed 2008).

In this study, the Mann-Kendall test is performed in three ways: (i) the regular Mann–Kendall (MK1) without autocorrelation, (ii) Mann–Kendall with a lag-1 autocorrelation (AR) and trend-free pre-whitening (MK2), and (iii) Mann–Kendall with LTP (MK3). The Mann–Kendall test is applied to the streamflow data using the above three approaches. By comparing results obtained from MK1, MK2 and MK3, we can examine the effects of AR and LTP on the trends of streamflow data.

3.3.2 Change-point analysis

A change-point analysis based on the nonparametric Pettitt test (Pettitt 1979) (a robust method for detecting abrupt change points in a continuous time series (Villarini et al. 2012) was conducted on the mean and variance of precipitation and streamflow time series. The Pettitt test is a rank-based test that examines whether two samples come from the same population through building a Mann-Whitney statistic that allows detection of a single change-point in the mean of the variable of interest at an unknown point in time, which makes it more robust against outliers and skewed distributions than parametric tests. Even though there could be more than one change-point, we assume that there is no more than one change-point in order to not segment the time series into too many subseries, which could have negative effects on the trend analysis results.

The p-value of the test statistic is calculated using an approximate limiting distribution of the Kolmogorov-Smirnov goodness-of-fit statistic. (Muggeo 2003; Villarini et al. 2012).

3.3.3 Wavelet analysis

This study investigates the possible teleconnection between river discharge and certain climate patterns by wavelet analysis, including a Continuous Morlet wavelet transformation, a global wavelet spectrum (GWS), a scale-averaged wavelet power (SAWP) and the wavelet coherence (WTC). In a continuous Morlet wavelet transformation, a time series of monthly river discharge with seasonality removed is decomposed into time-frequency fields, with the variance of wavelet coefficients of various frequency bands summarized by a GWS. Based on the results of GWS, fluctuations over certain periods are filtered out by SAWP and are correlated with climate indices in the corresponding frequency bands. Then the WTC with climate indices as covariates is conducted to investigate the possible effect of climate patterns on the river discharge data over time. Details of these methods can be found in various studies (Jevrejeva et al. 2003; Mwale and Gan 2004; Tan et al. 2016).

3.4 Results:

3.4.1 Temporal Trend of Streamflow Data

The regular Mann-Kendall test was used to estimate the possible temporal trend in the streamflow of the three basins at annual, seasonal, and monthly time scales, in which the seasonality within the monthly streamflow time series have been removed in the preprocessing that minus long-term mean value and divided by the long-term standard deviation value. Results were presented in Figure 3-2. From Figure 3-2a, we find that the annual streamflow of stations located at the downstream and the main branches shows statistically significant positive trends, while the upstream stations of ORB and LRB show negative trends. As expected, at the monthly time scale, streamflow time series have higher variance spatially. Monthly streamflow of small subbasins with less than 10×10^4 km^2 drainage areas at the mid- and upstream parts of ORB have significant trends, but only few stations at the middle of YRB have significant increasing trends (Fig. 3-2b).

Figure 3-2c-f show stations with significant trends in the seasonal streamflow time series. In ORB and LRB, streamflow of upstream rivers have decreased in spring and summer (Fig. 3-2c, d) but increased in winter and autumn (Fig. 3-2e, f). In these areas, there are several large dams and relatively larger water use along the river valleys than other regions, resulting in reduced summer peak flood and the release of water for power generation over the winters (Yang et al. 2004a; Yang et al. 2004b). Climate warming leads to more rainfall and less snowfall, which has contributed to higher winter streamflow. With relatively less human activities but higher permafrost coverage than others, the trends of streamflow in LRB should reflect the hydrologic response of LRB to the impact of climate change. The streamflow in winter seasons shows increasing trends without water release from reservoirs. The summer streamflow also shows an increasing trend in reservoir-free sub-basins, while the streamflow in areas with a reservoir has decreased. Therefore, reservoir regulation is partly responsible for the observed seasonal changes, especially in winter.

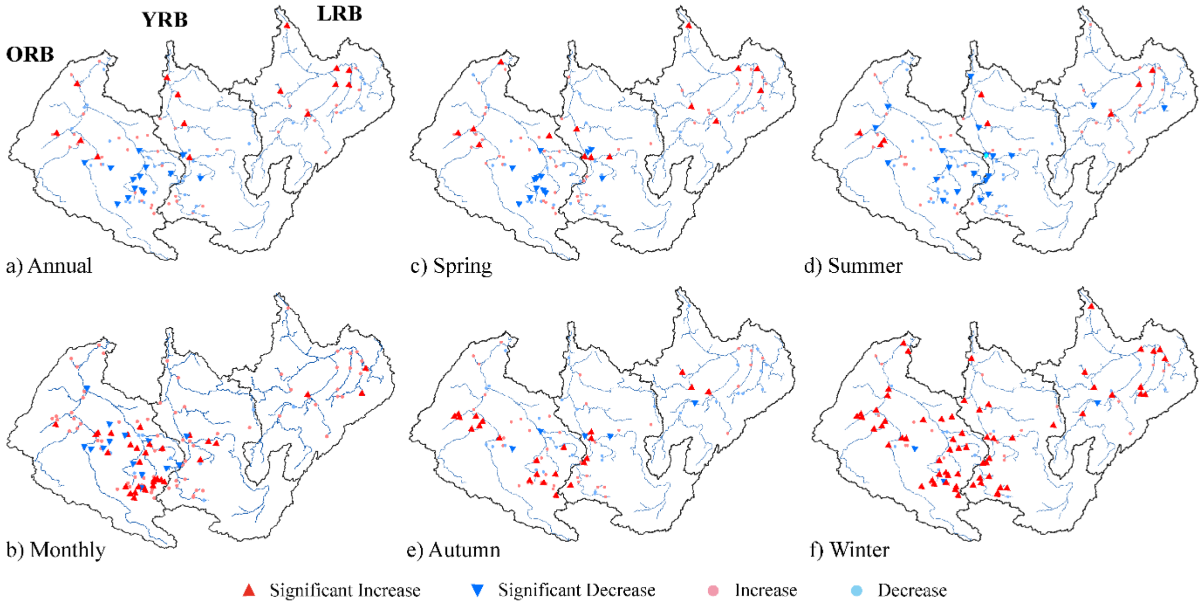

a) Annual c) Spring d) Summer b) Monthly e) Autumn f) Winter

Figure 3-2. Temporal trend of the monthly, seasonal, and annual streamflow of the Siberian river basins from the regular MK1 test (the significance of 0.05 was used).

3.4.2 Lag-one Autocorrelation and Long-Term Persistence (LTP)

From the MK2 and MK3, we estimate the LTP and lag-one auto-correlation (AR1) in the annual and seasonal streamflow. Figure 3-4 shows the spatial distribution of stations with time series showing LTP and AR1. Most stations that have a significant trend (Fig. 3-2) also have LTP and AR1 (Fig. 3-3), and almost all stations that have AR1 also have LTP. LTP exists in nearly all stations that have a significant trend no matter whether it is increasing or decreasing, while AR1 is found in stations located in the upper stream of ORB, in the mainstream of YRB, as well as in the middle stream of LRB (Fig. 3-3a). In spring, stations with LTP are mainly located in the plain area in ORB and in the western part of YRB (Fig. 3-3b). Compared with spring, there are more LRB stations that show LTP, and more stations in the upper stream of YRB have AR1 (Fig. 3-3c). In autumn, most ORB stations that have LTP and AR1 are in the upper stream, but those in YRB are located along the mainstream (Fig. 3-3d). Stations in the upper stream of ORB that show an increasing trend in winter streamflow also have significant AR1, while stations in the middle stream of LRB also have AR1 (Fig. 3-3e). The winter discharge of all three basins have AR1 and LTP. Therefore, given that the stations that have a significant trend almost all have LTP or AR1, it is necessary to further analyze the contributor of the trend of the streamflow.

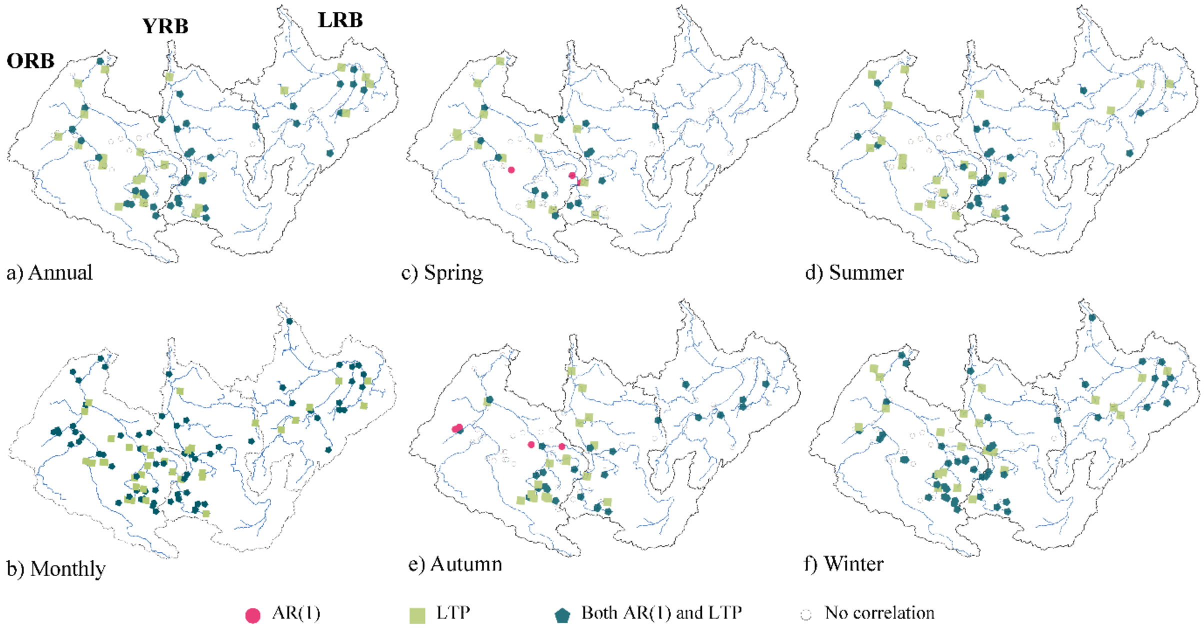

Figure 3-3. Spatial distribution of AR1 and LTP in the annual and seasonal time series from the MK2 and MK3 test (the significance of 0.05 was used).

3.4.3 Change points of the Streamflow

The Pettitt test was applied to the deseasonal monthly streamflow to detect the abrupt change point and their significance, shown in Figure 3-4. Among 160 stations analyzed, 40 stations are detected with statistically significant change points in their monthly streamflow time series, and most of them occurred between 1960 and 1985 (Fig. 3-4a). The streamflow of ORB, YRB, and LRB have been detected with significant change points at 1969, 1984, and 1979, respectively (Fig. 3-4b, c, d). Further, after the change points, all the streamflow of ORB, YRB and LRB had increased. The largest reservoir in ORB, Bukhtarma reservoir was completed in 1960 with max capacity of 49.8 km^2 (Yang et al. 2004a). YRB has the most number of reservoirs among the three basins, and most of them were first filled in 1960s to 1970s (Adam et al. 2007), while the stations at the reservoir outlets had abruptly changed in 1984. In LRB, the largest reservoir, Vilyuy reservoir was completed in 1967 to provide hydropower for industrial use, with max capacity 35.9 km^2 (Ye et al. 2003). Considering the timing of reservoirs operation and their capacity, the abrupt change point detected in the discharge of the whole river basins is the combined results of dam regulation, and climate change that the attribution of these two factors requires the dam operation dataset.

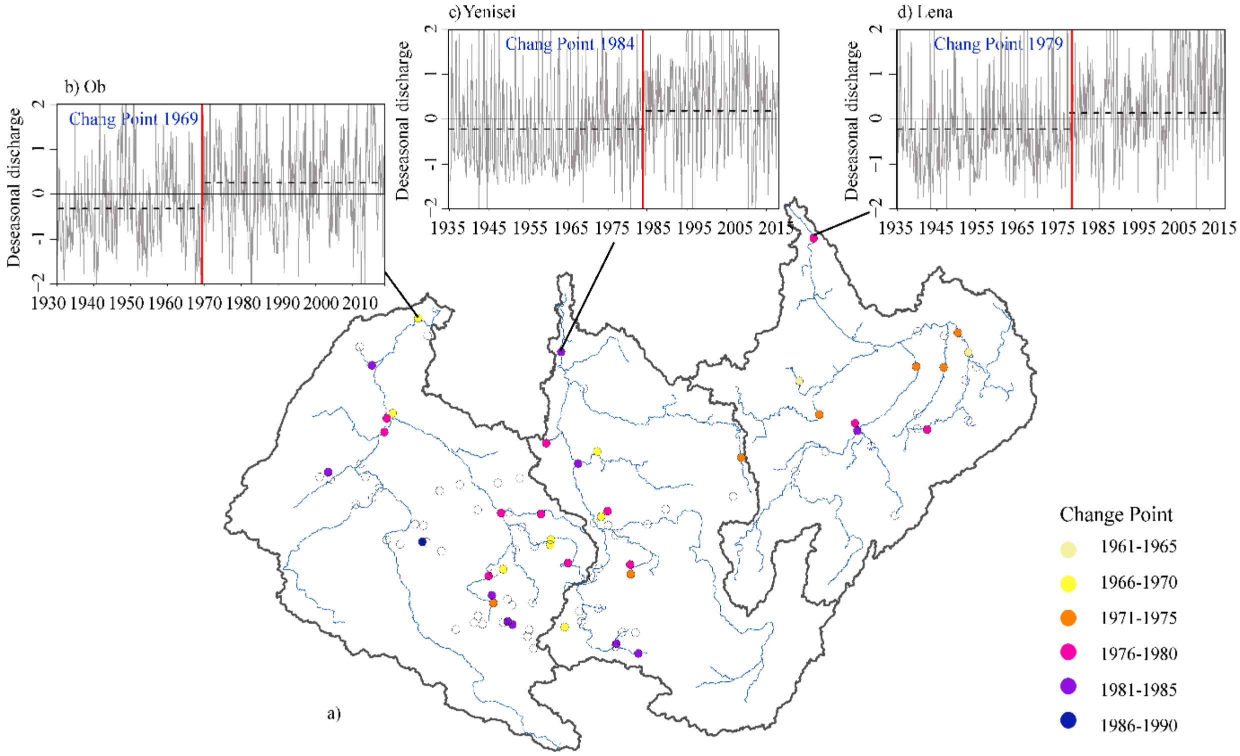

Figure 3-4. Significant change point detected through Pettitt test: a) spatial distribution of change point in the standardized deseasonal monthly streamflow, b, c, d) the time series of deseasonal monthly discharge of the whole ORB, YRB, and LRB, and their significant change points (the significance of 0.05 was used).

3.4.4 Wavelet analysis of Monthly Discharge

The Morlet wavelet was used to decompose the deseasonal monthly discharge of the three Siberian river basins into time-frequency fields, from which the periodicity of the discharge could be investigated at multi-time-scales. Figure 3-5 shows the local wavelet spectra of the deseasonal monthly discharge. In ORB, there is a strong periodicity of 4-16 months (annual) that is significant during 1930 to 2018 and the periods longer than 64 months were also significant since the 1950s (Fig 3-5a). In YRB, significant interannual oscillations at the 64-128 month time-scales are detected between 1935 and 2018 (Fig 3-5b). In LRB, significant interannual oscillations at 64-128 month and interdecadal time-scales (longer than 256-month time scales) (Fig 3-5c). Therefore, these three scale bands at annual, interannual and interdecadal (1-16 months, 64-128 months, and >256 months) oscillations were selected to compute the SAWP.

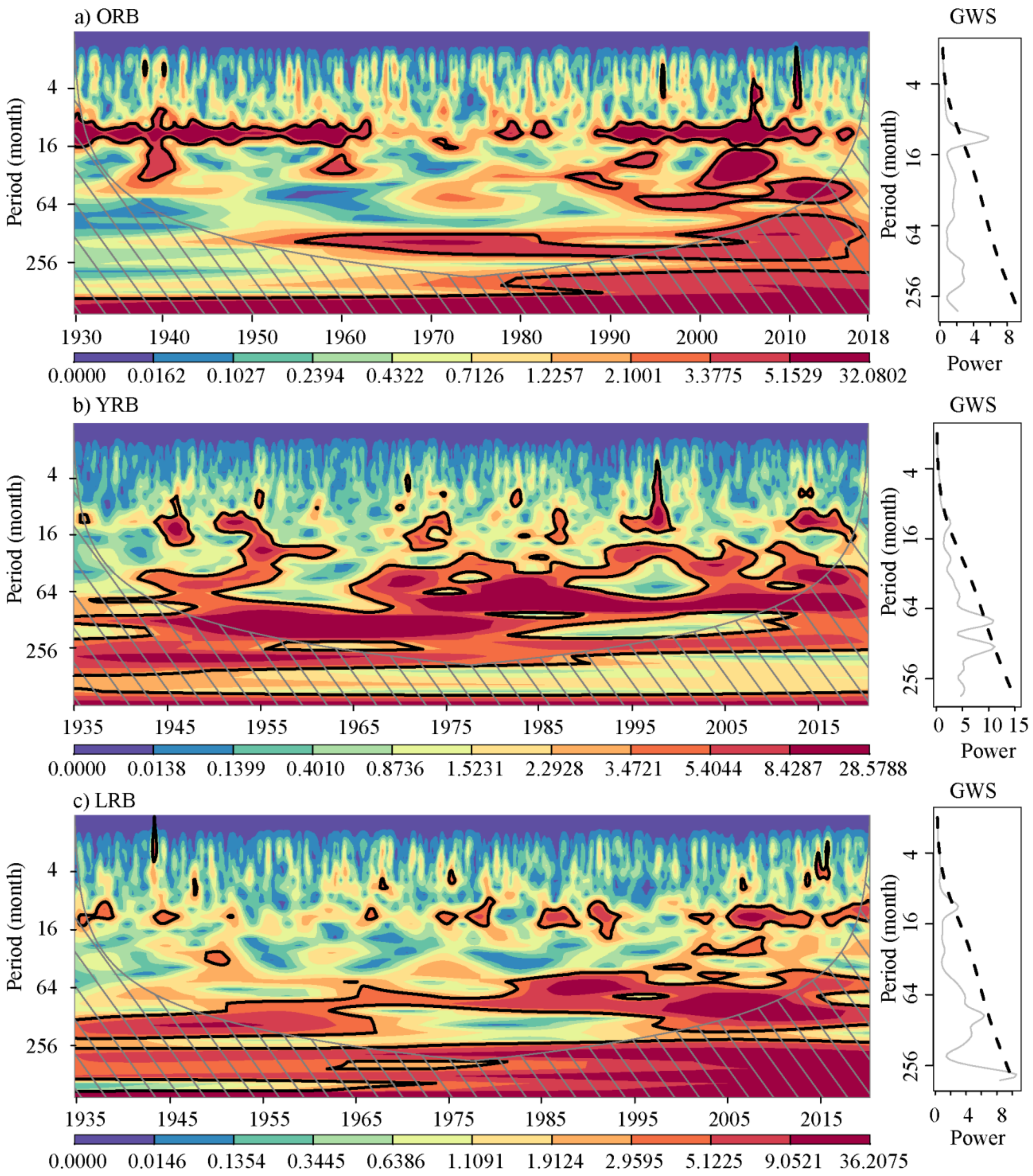

Figure 3-5. Continuous Morlet wavelet spectrum and global wavelet spectrum (solid grey line) with 95% confidence level (dashed line) of the monthly discharge of the three largest Siberian basins are presented. The color bar shows the wavelet power, while the thick black contours depict the 95% confidence level of local

power relative to a white noise background. The grey slash is the cone of influence beyond which the energy in contaminated by the effect of zero padding.

The SAWP of the deseasonal monthly river discharge at 1-16 month, 64-128 month, and >256 month time-scales are shown in Figure 3-6. At the 1-16 month time-scales (Fig. 3-6a), the variance of the monthly discharge are larger after 1990s than before. At the 64-128 month time-scales, all the monthly discharge of the three basins show increasing trend after 1990s (Fig. 3-6b). At longer than 256-month time-scales, YRB and LRB show increasing trends while ORB shows a decreasing trend (Fig. 3-6c).

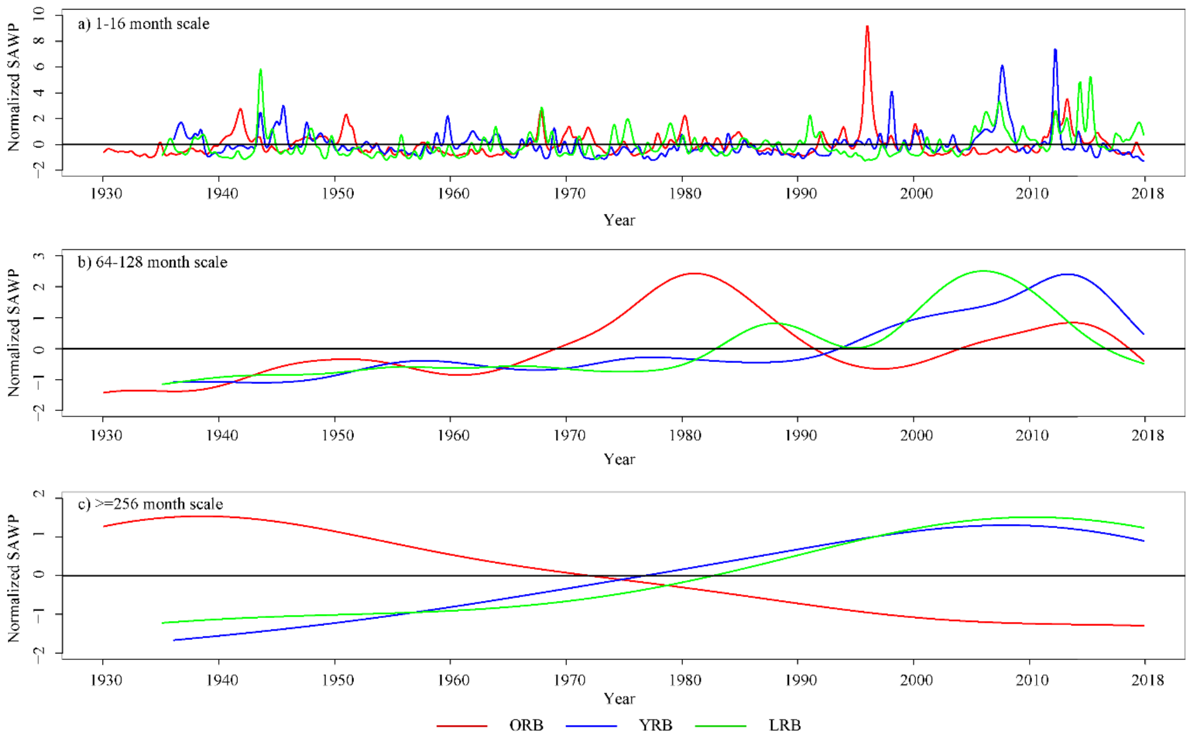

Figure 3-6. SAWP at 1-16 month (annual), 64-128 month (inter-annual) and longer than 256 month scales (inter-decadal) of the discharge of the three river basins.

3.4.5 Wavelet Coherence between Monthly Discharge and Climate Indices

The Pearson correlation coefficients between climate indices and SAWP of monthly discharge at multi-time-scales were estimated (Table 3-2). We found that NP and Nino 3.4 have significant positive correlation with deseasonalized monthly discharge of YRB at 1-16 month time-scales, while AO and NP have significant positive correlation with that of LRB. AO and PNA have significant positive correlation with monthly discharge of ORB at both 64-128 month time-scale and longer than 256-month time-scales. For LRB, AO, PNA, and Nino 3.4 have significant negative relationship with the monthly discharge at higher than 256-month time-scales. These significant correlations confirmed the existing of relationship between the climate pattern and the discharge at certain temporal-scales.

Table 3-2. Pearson's correlations between the SAWP of wavelet decomposed monthly discharge and climate indices for selected scales. Statistically significance correlations at the 5% significance level are in bold text.

Basin	Scale	AO	NP	PNA	NINO 3.4
ORB	1-16 month	0.038	**0.126**	0.059	**0.102**
	64-128 month	**0.071**	-0.009	**0.087**	0.032
	>=256 month	**0.139**	-0.041	**0.099**	**0.087**
YRB	1-16 month	**0.133**	**0.201**	-0.051	0.022
	64-128 month	**0.072**	-0.031	**0.099**	0.005
	>=256 month	**0.133**	-0.032	**0.099**	**0.079**
LRB	1-16 month	0.009	0.040	-0.003	0.055
	64-128 month	0.014	-0.046	0.039	0.011
	>=256 month	**-0.141**	0.036	**-0.099**	**-0.096**

The wavelet coherence was used to estimate the phase relationship between the climate patterns and river discharge of the three Siberian basins. The monthly climate index was used as covariates. For ORB, NP has significant relationship with the river discharge at around 16-month time-scales during 1990s and after 2000s (Fig. 3-7c), and NP also has a strong relationship with the discharge of ORB at interdecadal time scales from the 1970s to the 1990s. The discharge of YRB has a strong relationship with NP at an annual scale over the whole study period.

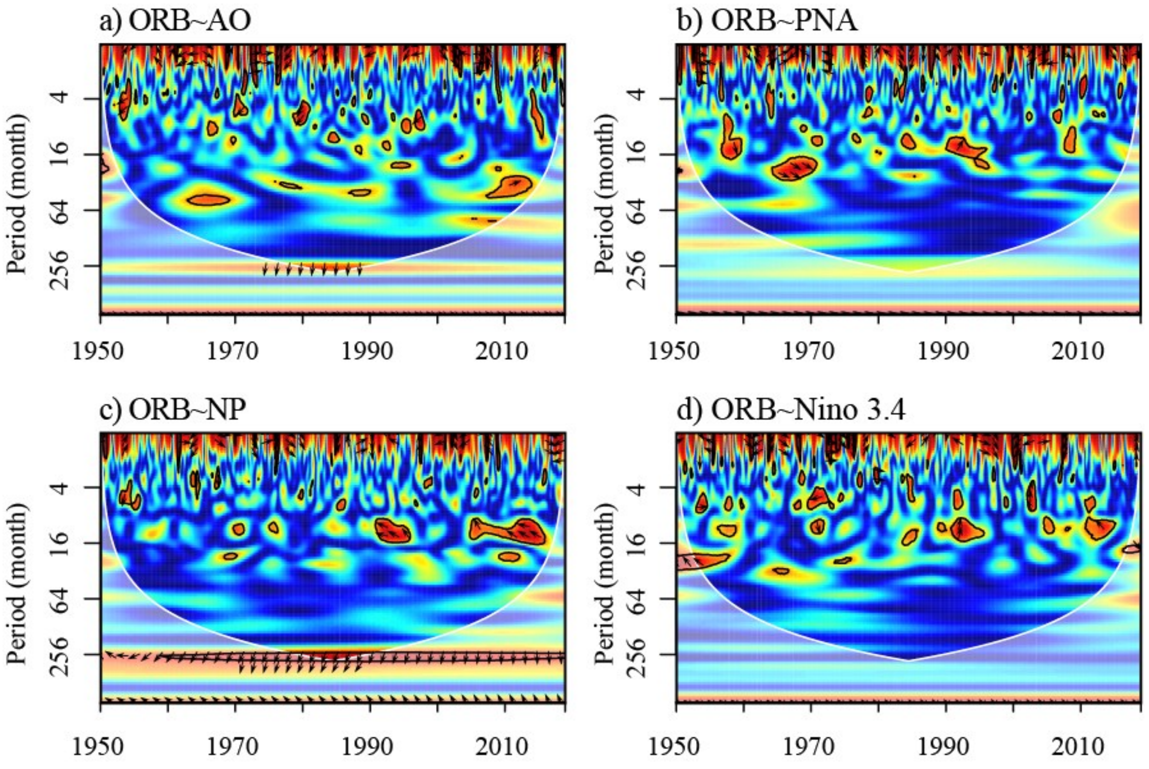

Figure 3-7. In WTC spectra and phase difference between the monthly river discharge of ORB and four climate indices, the thick black contours enclose periods with statistically significant coherence relative to a red noise process at 5% significant level. The phase difference is plotted only for time periods and scales with coherence over 0.7. The right (left) pointing arrows indicate that the two signals are in phase (antiphase), arrows pointing down (up) means that climate indices lead (lag) discharge by 90°.

For YRB, there is a significant relationship at about the 16-month time-scale between NP and the monthly discharge since the late 1970s, which were in-phase before the end of the 1960s but were anti-phase since the end of the 1970s. Nino 3.4 is also significantly teleconnected to the YRB discharge at annual time scale. Nino 3.4 led YRB discharge by 90° before the 1970s, but led YRB by 270° after the 1990s. Compared with NP and Nino 3.4, AO and PNA have relatively weaker relationships with the YRB discharge at the 16-month time scale.

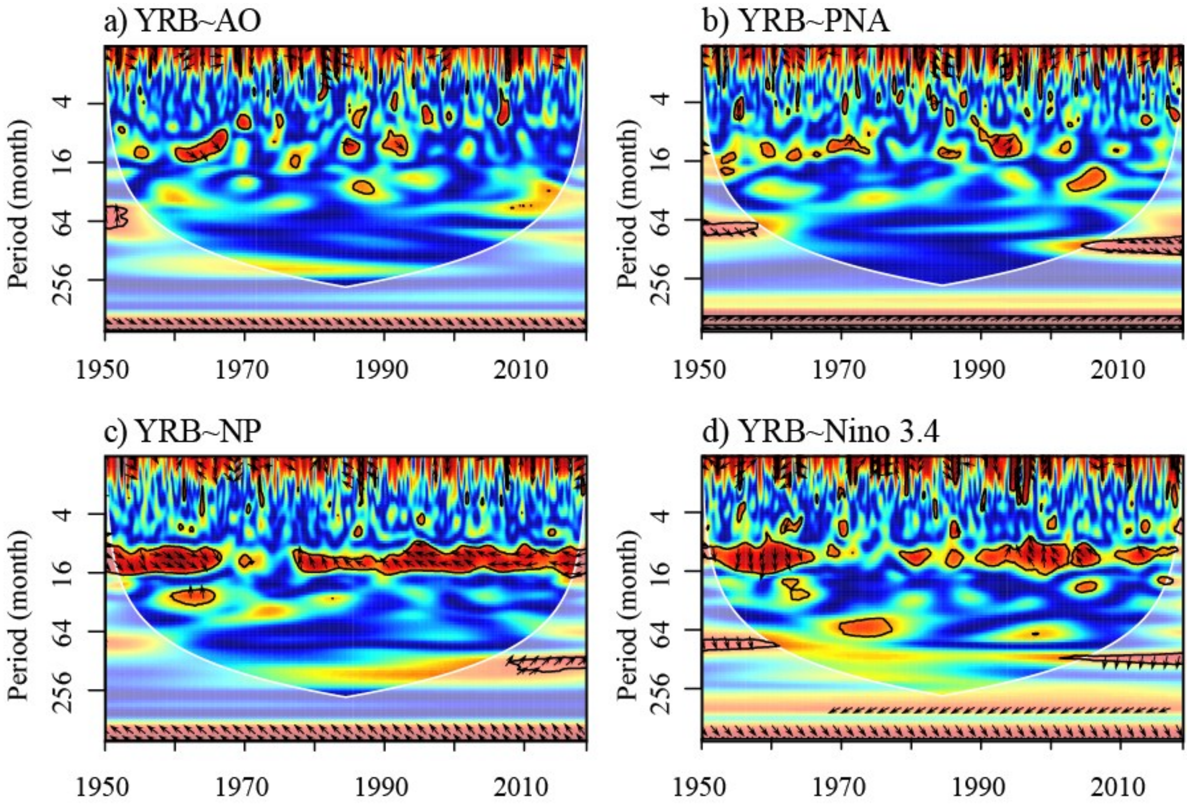

Figure 3-8. Same as Figure 3-7, but for YRB

There were significant in-phase relationships between AO and the monthly discharge of LRB since the late 1970s at about 64-month time scale. In the 1990s, PNA led the LRB discharge by 90° at about 64-month time scale. NP was significantly teleconnected to the LRB discharge at about 16-month time-scale intermittently, that was in-phase before 1980s but anti-phase there after. At about 64-month scale, NP had a strong in-phase relationship with LRB discharge since 1980s. As for Nino 3.4, there was an intermittent significant anti-phase relationship with the LRB discharge at 16-month time scale.

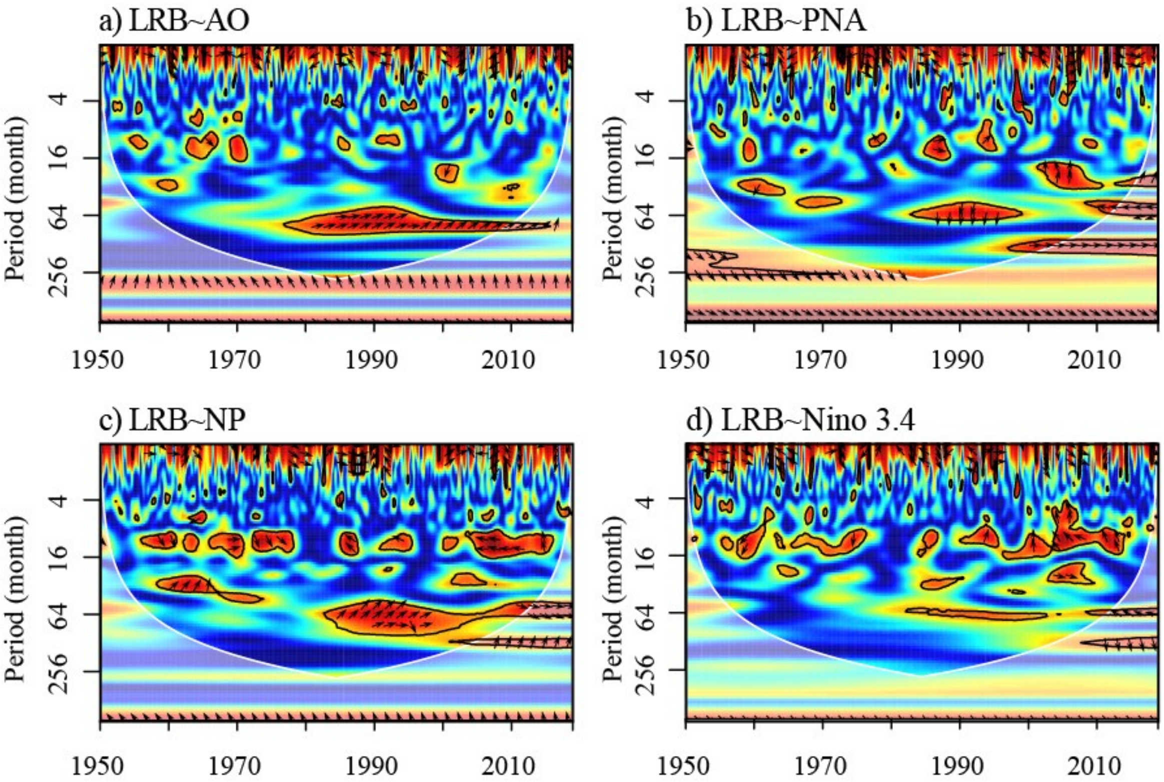

Figure 3-9. Same as Figure 3-7, but for LRB

These findings demonstrate that the variability of the discharge of Ob, Yenisei and Lena river basins are teleconnected to certain climate patterns at multi-time-scales, which is largely dependent on the variability of climate patterns. Limited by the length of the time series of streamflow, the influence of climate patterns at decadal and higher time scales cannot be fully examined. The multidecadal variability of the discharge of Ob and Kolyma rivers have been shown from reconstructions, and apparently they are similar with that of climate patterns originated from the North Atlantic, North Pacific, and the Northern Hemisphere (MacDonald et al. 2007). If longer dataset will be available, we will be able to more thoroughly analyze the periodicity and the non-stationarity of the streamflow of Siberia subjected to the impact of warming and climate patterns.

3.5 Discussions of Results

We have detected significant increase in the discharge of three large Siberian river basins at multi-time scales, which are related to changes in precipitation in recent decades. Extreme precipitation events have been occurring more frequently since the 1980s (Ye et al. 2017a; Ye et al. 2017b). Rainfall rates are increasing at the expense of snowfall rates(Screen and Simmonds 2011). Such recent changes in precipitation has resulted in changing variability of river discharge over different seasons. Numaguti (1999) found different water recycling processes over Eurasia, such that the winter precipitation is mainly supplied by evaporation from oceans, but summer precipitation mainly by evaporation from the continental land surface. Under a warmer atmosphere in the Arctic since the 1980s, which has been warming at about double the global average, known as Arctic Amplification attributed to ice-albedo and other feedback mechanisms (Pithan and Mauritsen, 2014), the more intensive recycling of water between the atmosphere and the land surface should contribute to recent hydrologic changes in Siberian river basins. Warming leads to higher frequency and intensity of precipitation events, along with higher atmospheric precipitable water precipitation (Ye 2008). However, Ye and Cohen (2013) found that warmer fall and spring will delay the onset and hasten the end of snowfall season, and reducing the length by about 6.2 days per ^{o}C increase in mean temperature over the Arctic.

The variations of surface air temperature over Eurasia during 1980-2000 were found to correlate to the variability of AO (Rigor et al. 2000). During the negative phase of AO, the upper-level air flow convergence was enhanced, which is concurrent with an anomalous anticyclonic flow over the Urals around 500hPa (Gong and Ho 2002). The atmospheric circulation variation in Pacific sectors had caused the atmospheric shift over North Eurasia, contributing to seasonal changes of Siberian river discharges. (Savelieva et al. 2000).

The pan-Arctic region is covered with permafrost extensively, which is sensitive to air temperature, with an active layer on top, undergoing annual freeze and thaw cycle. The distribution of permafrost can modify the hydrologic conditions through the soil moisture, connectivity of inland waters, streamflow seasonality, and the partitioning of water stored above and below ground (Walvoord and Kurylyk 2016). The development of continuous permafrost over the Great Siberian river basins can also contribute to higher water mass (Muskett and Romanovsky 2009). In the 2000s, the abrupt warming of top soil and the deepening active layer thickness in the Lena River basin were observed in response to increasing rainfall, which was partly caused by enhanced cyclonic patterns (Iijima et al. 2016). In the Lena river basin, which has the highest permafrost coverage of the three basins, the maximum/minimum discharge ratios had decreased over 1942-1998 partly due to higher base flow, which is consistent with the degradation of permafrost (Ye et al. 2009). The enhanced infiltration and deeper flowpath over the Yukon River basin are found to be the result of degradation of permafrost (Walvoord and Striegl 2007). Besides, the distribution, structure, composition and growth rate of vegetation also adjust to the thawing of permafrost (Torre Jorgenson et al. 2013; Zhang et al. 2005), which could have a critical impact to hydrologic processes. Researches has found the increasing of the Normalized difference vegetation index (NDVI) over the high-latitude river basin during the growing season consistent with the discharge variations (Xu et al. 2016).

Hydrologic responses over high-latitude river basins to climate warming impact are complex and spatially they can be dramatically different at local and landscape scales (Torre Jorgenson et al. 2013). Besides climatic factors, anthropogenic activities such as dam regulations will increase winter discharge at the expense of summer discharge (Yang et al. 2002; Ye et al. 2009), but dam regulations generally will not affect the annual variability of streamflow (McClelland et al. 2004). Affected by ground ice and topography, permafrost thawing is expected to accelerate under increased surface runoff caused by increasing precipitation (Jorgenson et al. 2010). Along with increased precipitation, evapotranspiration will also increase (Park et al. 2008). Therefore in high latitudes, under simultaneous increase of evapotranspiration and precipitation, changes in hydrologic variability could be complex.

3.6 Conclusions

In this study, from applying non-stationary analysis to the annual, seasonal and monthly streamflow time series of three major Siberian river basins, Ob (ORB), Yenisei (YRB), and Lena river basins (LRB), statistically significant non-stationarities were detected. The streamflow of these Siberian river basins exhibit extensive increasing trends at multiple time-scales, except the seasonal streamflow from the upstream of ORB and YRB, which suffer from the impacts of dam regulation, agricultural and industrial water use. Most streamflow stations show significant change points during the 1970s to 1980s. From the wavelet analysis, significant periodicities at annual, inter-annual, and interdecadal time scales were detected in the streamflow of the three northern Siberian river basins. The significant correlation between these streamflow data and climate patterns at different time scales were also detected, which could be the result of different forcing mechanisms. The results of this study provide some new insight into the hydrologic changes of Siberian river basins under the amplified impact of climate warming in the Arctic, and into their teleconnections with climate oscillations.

Chapter 4. Streamflow of great Pan-Arctic river basins in Siberia: Modeling and Impacts of Climate Change

4.1 Introduction

Streamflow is the largest single source of freshwater to the Arctic Ocean. It delivers 38% of the total freshwater flux (Serreze et al. 2006) and is critical to the stratification of the Arctic Ocean (Durocher et al. 2019; Hamman et al. 2017; Yang et al. 2016) and to the formation of Arctic sea ice . With global climate change, the rate of warming over the Arctic is twice the global average because of a variety of positive feedbacks resulting known collectively as Arctic Amplification. Affected by the warmer atmosphere, the streamflows of pan-Arctic river basins have changed and most show an increasing trend (McClelland et al. 2006; Rood et al. 2017). In the lower Ob regions, streamflow increased during mid-summer and winter months, which is associated with increases in summer precipitation and winter snow cover (Yang et al. 2004c). In North America, the spring peak timing of the Mackenzie river basin has advanced by several days (Yang et al. 2015), while the peak volume of Siberian rivers has increased (Nijssen et al. 2001a).

An increase in streamflow is the combined result of changes in precipitation and land surface. A series of studies have revealed that precipitation over north Eurasia has trended towards a greater number of more intense events (Chernokulsky et al. 2018; Chernokulsky et al. 2019). The warmer temperature and moister atmosphere are found to dominate the increase of the precipitation intensity and amount (Ye et al. 2015), the efficiency of precipitation (Ye et al. 2014), and the more frequently occurring convective rainy days (Ye et al. 2017a; Ye et al. 2017b). At the same time, the dry spell increases with air temperature, while wet spell decrease during summer (Ye 2018). The wildfires in Fort McMurray, 2016, for example, could be attributed to the low winter snowpack combined with an extremely warm and dry spring (Tan et al. 2018a).

For the land surface, the permafrost mass changes over the large Siberian rivers, such as Ob, Lena, and Yenisei, were found to have increasing trends under a warmer atmosphere, which is associated with long-term hydrological changes (Steffen et al. 2012). The water storage of (Wang et al. 2012)North America was also found to increase over the past decades (Wang et al. 2012). The melting of excess ground ice in permafrost contributes to the thickening of the active layer over the discontinuous permafrost regions in the central Lena basin (Landerer et al. 2010). Vegetation greening is also a significant response of the pan-Arctic river basins to the warmer atmosphere (Esau et al. 2016; Varlamova and Solovyev 2016). In the Mackenzie river basin, a higher Normalized Difference Vegetation Index (NDVI) and a longer growing season were linked with a higher streamflow (Xu et al. 2016).

Given such complex factors including precipitation, evaporation, runoff yield and confluence, topography and human activities, it is challenging to achieve accurate streamflow forecasting (Kumar et al. 2013). An accurate representation of the streamflow flux is critically important to understanding local hydrological processes and to the improvement of ocean models in GCMs (Hamman et al. 2017; Nummelin et al. 2015). However, there have been few studies that have simulated the streamflow of the pan-Arctic river basins at the basin-scale using hydrological models. The Hydrologiske Byrån avdeling för Vattenbalans (HBV) was applied to the Mackenzie river basin and projected the future streamflow under different emission scenarios (Scheepers et al. 2018). Scheepers et al (2018) found that warmer temperatures and higher precipitation are the main causes of the increase in winter and spring streamflow of the Mackenzie river. The Variable Infiltration Capacity (VIC) hydrology model was used to estimate the effects of reservoirs operations on the streamflows of the Ob, Lena, and Yenisei rivers in 2007 (Adam et al. 2007), and in that study it was found that the changes in annual streamflow is more likely due to the direct effects of climate change, whereas the human impacts were more noticeable on the monthly and seasonal streamflows.

Although hydrological models assist in the physical understanding of hydrological processes, their data requirements and uncertainties limit their application, especially in the pan-Arctic river basin, where the length of observations is relatively short and the density of observational sites is small. Thus, the data-driven models that are based on data analysis are becoming more popular in streamflow prediction due to their simplicity, minimal information requirements and ease of real-time implementation (Adamowski and Sun 2010). Although they may lack the ability to provide physical information of hydrological processes, data-driven models are capable of accurately predicting streamflow (Zhang et al. 2015b). While data-driven stochastic models are often limited by assumptions of normality, linearity and variable independence (Chen and Singh 2018), another data-driven type of model based on machine learning (ML) shows strong potential for simulating complex hydrological processes. For example, Papacharalampous et al. (2019) conducted computational experiments to compare stochastic and ML methods regarding their multi-step ahead forecasting properties as applied to hydrological processes and suggested that the ML methods exhibit superior performance.

Among the numerous ML methods, Artificial Neural Networks (ANNs) are a widely used method for long-term hydrological simulations and forecasting (Ghumman et al. 2011; Kalteh 2013; Rajaee et al. 2019; Yaseen et al. 2015). But ANN still has some intrinsic disadvantages, such as slow convergence speed, less generalizing ability, arriving at a local minimum and over-fitting problems (Guo et al. 2011). Support vector machine (SVM) is based on the Vapnik Chervonenkis (VC)-dimension theory that measures the capacity of the learning machine (Boser et al. 1992) and on structural risk minimization of statistical learning (Cortes and Vapnik 1995). Compared with the conventional neural network method, SVMs have their own distinct advantages: first, SVMs have better generalization ability; second, the architectures and the weights of SVMs are guaranteed to be unique and globally optimal; third, SVMs are trained much more rapidly. Especially on a small sample size, SVMs have good performance because they are not concerned with probability measures or the law of great numbers. The essence of SVM is to transfer the original problem into solving a quadratic programming problem, it can theoretically obtain the global optimum result of the problem, while the ANN is easy to converge to local minimum (Guo et al. 2011). Thus SVMs have emerged as an alternative data-driven tool in many conventional neural network dominated fields (Wu et al. 2014).

For their advantage of good generalization behavior with non-stationary time series, SVMs have been widely used in the simulation and prediction of runoff at multi-scales in river basins with high human population. However, there have been few applications of ML models in the simulation of streamflow in northern river basins (Yilmaz and Muttil 2014), especially in the large river basins, due to the limited observations. Thus, the goal of this study is to evaluate the application of the ML method on streamflow simulations at the basin-scale and predict the future changes of streamflows from pan-Arctic river basins under different greenhouse gas emission scenarios. The performance of SVM on simulating the monthly streamflow at the outlets of four great pan-Arctic river basins: Mackenzie river basin, Ob river basin, Lena river basin, and Yenisei river basin, is here evaluated and compared with Artificial Neural Networks model (ANN) and Multi-variables Linear Regression (MLR) model. We concentrate on the ability of these models to match the low flow during the freezing months and the spring peak timing and volume. The root mean squared error (RMSE), the Nash-Sutcliffe efficiency (NASH), R-squared (R^2), and the mean absolute error (MAE) are all used to qualitatively evaluate the performance of each of these models in each of the river basins. The validated models are then used to predict the monthly streamflow based on four CMIP5 GCMs: ACCESS 1.0, CanESM2, HadESM2-ES, and MPI-ESM, under RCP 4.5 and RCP8.5 climate change scenarios. The relative changes of the streamflow and the trends of the streamflow are quantified for these two scenarios..

This paper is organized as follows: the streamflow data and hydro-climatological variables as predictors are described in section 4.2; the technical details of the SVM model are described in section 4.3; the training and testing of SVM, ANN, and MLR models are given and compared in section 4.4; the predicted streamflow under RCP 4.5 and RCP 8.5 emission scenarios are provided in section 4.5; conclusions are given in section 4.6.

4.2 Study area and Data Sources

4.2.1 Streamflow data

The study area includes the four largest river basins that drain into the Arctic Ocean: the Mackenzie river basin in North America; the Ob' river basin; the Lena river basin, and the Yenisei river basin (abbreviated these four river basins as MOLY). The total drainage area of MOLY is 10,439,000 km^2, of which the Mackenzie river basin (MRB) has 1,805,000 km^{2,} the Ob river basin (ORB) has 2, 975, 000 km^{2,} the Lena river basin (LRB) has 2. 430, 000 km^2, and the Yenisei river basin (YRB) has 2, 554, 000 km^2. The average streamflow of MOLY is 57, 663.68 m^3/s, in which the Mackenzie river releases freshwater at a rate of 9, 127.48 m^3/s into the Beaufort Sea in the Arctic Ocean; the Ob river releases freshwater at a rate of 12, 660.82 m^3/s into the Kara Sea, the Lena river releases freshwater at a rate of 17, 221.51 m^3/s into Laptev Sea, and the Yenisei river releases freshwater at a rate of 18, 653.88 m^3/s into the Kara Sea.

In this study, the discharge of each basin is determined. Only the station that is closest to the outlet of the basin is considered. The lengths of observation are different among MOLY: ORB has the longest observational records, which began in 1930; the streamflow of LRB has been measured since 1935; the streamflow of YRB has also been measured since 1935, and; the streamflow of MRB has been measured since 1979. The monthly streamflow observations before 1999 were obtained from R-ArcticNet (v. 2.0) (Regional Hydrographic Data Network for the Pan-Arctic Region) in CD-ROM (Lammers et al. 2016). The long-term monthly streamflow of the Siberia basins have been observed systematically, and the observed data have been quality controlled and archived by the Russian Hydrometeorological Services (Shiklomanov et al. 2000). After 1999, under the direction of the Arctic and Antarctic Research Institute, the daily streamflow data are measured until the present and are available from ArcGRO (Shiklomanov 2018). The locations of the streamflow measurement stations of MOLY are shown in Figure 1: YRB is observed at Igarka (67.43°N, 86.48°E); LRB is measured at Kyusyur (70.68°N, 127.39°E); ORB is measured at Salekhard (66.63°N, 66.60°E); MRB is measured at Tsiigehtchic (67.45°N, 133.74°W). The monthly streamflow from the beginning of the measurement until 2018/12 were used in this study. MRB has 564 monthly streamflow records from 1979/01 to 2018/12. ORB has 1068 monthly streamflow records from 1930/01 to 2018/12. LRB has 1008 monthly streamflow records from 1935/01 to 2018/12. YRB has 996 monthly streamflow records from 1936/01 to 2018/12.

Figure 4-1. The locations of the main pan-Arctic river basins, and the stations where the streamflows of each basin were measured, denoted as red spots. In this study, the Mackenzie river basin, the Ob' river basin, the Lena river basin, and the Yenisei river basin are considered. https://www.arctic.noaa.gov/Report-Card/Report-Card-2018/ArtMID/7878/ArticleID/786/River-Discharge

4.2.2 Hydro-climatological predictors

In this study, the hydro-climatological variables: precipitation, temperature and potential evapotranspiration were extracted from CRU-TS 4.03, which has a spatial resolution of 0.5°×0.5° resolution (Harris 2020). CRU-TS 4.03 has records from 1901/01 to 2018/12, which is longer than reanalysis dataset, such as NCEP/NCAR Reanalysis I and ERA-Interim. And CRU-TS 4.03 also has relatively higher spatial resolution than NCEP/NCAR Reanalysis I and ERA-Interim. Predictors that were used to calibrate and validate the statistical and machine learning models are monthly precipitation (Pre, in mm), potential evapotranspiration (PET, in mm), near-surface temperature (Ta, in ºC), near-surface temperature maximum (Tmax, in °C), and near-surface temperature minimum (Tmin, in °C) all at 0.5° resolution. The time series of the basin-scale are the average of grids that lie within the basin. The temporal length of data used for the predictors is the same as the monthly streamflow records.

4.3 Methods

4.3.1 Support Vector Regression Model

The Support Vector algorithm was developed as a class of nonlinear search algorithms based on a statistical learning theory (Cortes and Vapnik 1995). Support Vector Regression (SVR) was then developed by including regression techniques (Drucker et al. 1997). On a small sample, SVM can have good performance for it was not consider probability measure or the law of great numbers that makes SVM different with the previous statistical method. The essence of SVM is to transfer the original problem into solving a quadratic programming problem. It can theoretically obtain the global optimum result of the problem, while Artificial Neural Network (ANN) is easy to converge to local minimum. Besides, the computing rate of SVM is significantly faster than ANN (Guo et al. 2011). A general overview of SVM is as follows.

The procedure of a SVM estimator (f) of a regression is written as:

$$f(x) = \langle \omega \cdot \varphi(x) \rangle + b, \text{ with } \omega \epsilon X, b \epsilon R \tag{4-1}$$

where, ω and b denote a weight vector and bias, respectively. $\varphi(x)$ is a transitive function, which maps the input space into a high-dimensional particular space. The objective function of a lenticular optimization with ε function, which can be explained as:

$$Min_{w,b,\xi,\xi^*} \frac{1}{2} \|w\|^2 + C \sum_{k=1}^{N} (\xi_k + \xi_k^*)$$

Subject to: $$\begin{cases} y_k - \langle \omega \cdot \varphi(x) \rangle - b \le \varepsilon + \xi_k \\ \langle \omega \cdot \varphi(x) \rangle + b - y_k \le \varepsilon + \xi_k^*, k = 1,2, \ldots, N \\ \xi_k, \xi_k^* \ge 0 \end{cases} \quad (4\text{-}2)$$

where, ξ_k, ξ_k^* denote slack variables, ε denotes the size of intensitive tube that is equivalent to the approximation accuracy placed on the training data points(Kalteh 2013), and constant C is a positive trade off factor between the approximation error and the weight vector $\|w\|$. The model was tuned using the Bayesian optimization approach implemented through the MlBayesOpt package in R (Adankon et al. 2011). The structural risk minimization approach, the basis of SVR designed to minimize errors of the fitting function is more efficient than the traditional approach than used by machine learning algorithms such as ANN. This is the one that makes SVM behave better than others when the training data is limited and avoids leading to the local optimal solutions (Chitralekha and Shah 2010).

4.3.2 Model training and validation strategy

ANN and MLR were compared with SVM to simulate the monthly streamflow from the four pan-Arctic river basins in this study. A grid searching algorithm was used to calibrate the ANN and MLR models, described as follows. For the duration of the streamflow time series, which are different within the different basins, 80% of randomly selected monthly streamflow records of each were used to train the three models, and the remaining 20% of monthly streamflow records were used to test the models. Therefore, in MRB, the number of months of streamflow observations used for training are 449, and those for testing are 113; in ORB, 852 months of observations were used to train the models, and 214 months were used to test the models. For LRB, 805 months of observations were used to train and 202 months were used to test the models. For YRB, 795 months of observation were used to train and 199 months were used to test the models.

Four metrics were evaluated to assess the performance of these models in simulating the monthly streamflow of four pan-Arctic river basins: the root mean squared error (RMSE), the Nash-Sutcliffe efficiency (NASH), R-squared (R^2), and the mean absolute error (MAE). The higher NASH and R2 represent the better performance of the model, while the higher RMSE and MAE represent the weak simulating ability of the model.

4.4 Results

4.4.1 Correlation between predictors and streamflow

The long-term time series of precipitation (Pre), potential evapotranspiration (PET), maximum temperature (Tmax), minimum temperation (Tmin), and mean temperature (Ta) were obtained from CRU TS 4.03 for MOLY with large drainage for each basins. Each hydro-climatological variable is an area-average of grids values within the outline of the basins. The correlations between predictors were estimated by Pearson correlation analysis, with results given in Table 4-1. Although the maximum and minimum temperature have very high correlation relationships, they have different effects on the streamflow. Given that pan-Arctic river basin are mostly driven by snow-melt, the minimum and maximum have critical effects on the melting and freezing of river ice. Therefore, they were both considered as predictors. In addition, their correlation with streamflow (R) are all statistically significant.

Table 4-1. List of predictors used in this study and their cross-correlations from Pearson correlation.

	R	Pre	PET	Tmax	Tmin	Ta	R	Pre	PET	Tmax	Tmin	Ta
			Mackenzie						Ob			
R	1	0.801	0.610	0.706	0.738	0.723	1	0.745	0.562	0.660	0.678	0.670
Pre		1	0.773	0.752	0.764	0.760		1	0.738	0.796	0.817	0.807
PET			1	0.917	0.884	0.903			1	0.940	0.915	0.929
Tmax				1	0.992	0.998				1	0.995	0.999

	R	Pre	PET	Tmax	Tmin	Ta	R	Pre	PET	Tmax	Tmin	Ta
Tmin					1	0.998					1	0.999
Ta						1						1
	Lena						Yenisei					
R	1	0.735	0.533	0.584	0.610	0.598	1	0.724	0.627	0.597	0.605	0.602
Pre		1	0.832	0.850	0.872	0.862		1	0.795	0.848	0.873	0.862
PET			1	0.907	0.896	0.903			1	0.923	0.901	0.914
Tmax				1	0.994	0.999				1	0.994	0.998
Tmin					1	0.998					1	0.998
Ta						1						1

4.4.2 Performance of SVM compared with ANN and MLR models

The performance of three models were evaluated by R2, NASH, MAE, and RMSE, and the results are summarised in Table 4-2. The performances of both ANN and SVM are better than that of MLR with lower MAE and RMSE, and higher R2 and NASH. Between ANN and SVM, SVM behaves better than ANN with better metric and, in addition, the calibration of SVM is much faster than ANN.

Table 4-2. Goodness of fit of ANN, MLR, and SVM models in the test group

	R2	RMSE	MAE	NASH		R2	RMSE	MAE	NASH
	Mackenzie					Ob			
ANN	0.959	4.842	0.198	0.917	ANN	0.907	6.377	0.267	0.820
MLR	0.903	7.296	0.318	0.812	MLR	0.773	9.523	0.500	0.598
SVM	0.959	5.091	0.198	0.908	SVM	0.947	4.852	0.167	0.896
	Lena					Yenisei			
ANN	0.948	3.365	0.200	0.895	ANN	0.905	9.365	0.217	0.785
MLR	0.786	6.448	0.405	0.615	MLR	0.710	14.400	0.455	0.492
SVM	0.970	2.552	0.131	0.940	SVM	0.891	9.186	0.247	0.793

The monthly streamflow simulations using ANN, MLR, and SVM during the test period are shown in Figure 4-2, in which the time series of the monthly streamflow and the error from the observations are also given. From the performance metrics, the behaviour of MLR is good, which means MLR can match the streamflow at the average scale. Figure 4-2. *1 shows that the shapes of the simulated streamflow generally match the observations as well as the timing of the spring peak and low flood during the freezing months. However, the time series curves are generally either higher or lower than the observations, and the scatters are distributed dispersedly in the error panels (Fig. 4-2. *2), in all four river basins. Especially over the low values, the simulated flood does not vary with the input variables. The performance metrics of ANN are better than those of MLR. From Figure 4-2. *1, the simulated low flood during the freezing months matches observations well. However, from the error panels, the simulated peak floods were overestimated constantly for all four basins (Fig. 4-2. *2). In addition, the intermediate values of simulated streamflow have a large error (Fig. 4-2. *2). To improve the performance of ANN, more variables as predictors may be needed, such as the snow water equivalent. As for SVM, it can match the low flood well over the timing and magnitudes (Fig. 4-2. *1). Although ANN missed the peak flood occasionally, the peak flood simulated by SVM is distributed evenly and is close to the observed values in the error panels (Fig. 4-2. *2). The performances of SVM were different between basins but were generally better than either ANN or MLR. Among the four river basins, the simulated streamflow from YRB has slightly larger errors than the other three basins and the peak flood is underestimated but still better than ANN and MLR (Fig. 4-2. d2). Comparing the relative error of the simulated peaks, SVM produces more simulated peaks with smaller relative errors than ANN and MLR, (Fig. 4-3). Therefore, SVM has generally better performance than ANN or MLR in the simulation of monthly streamflow from the pan-Arctic river basins and better captures the peak and low floods.

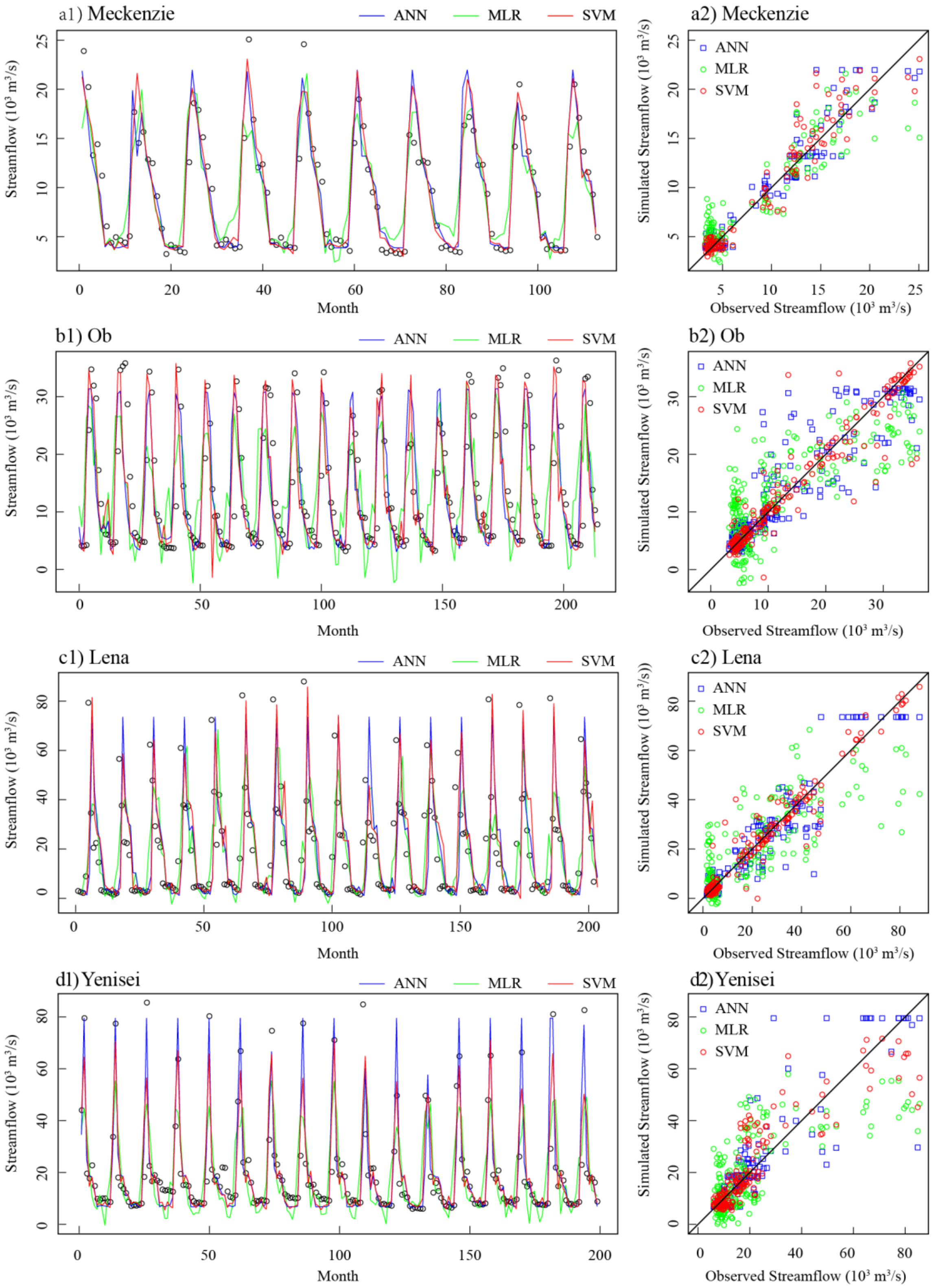

Figure 4-2. The simulation of monthly streamflow from ANN, MLR, and SVM in the test period. The left panels (*1) shows the times series of monthly streamflow, in which the black circles show the observations while solid

lines in color denote the simulated monthly streamflow from ANN, MLR, and SVM, respectively. The right panels (*2) show the streamflow simulation error from the three models in the test period for the four river basins, in which the black diagonal line represent y=x.

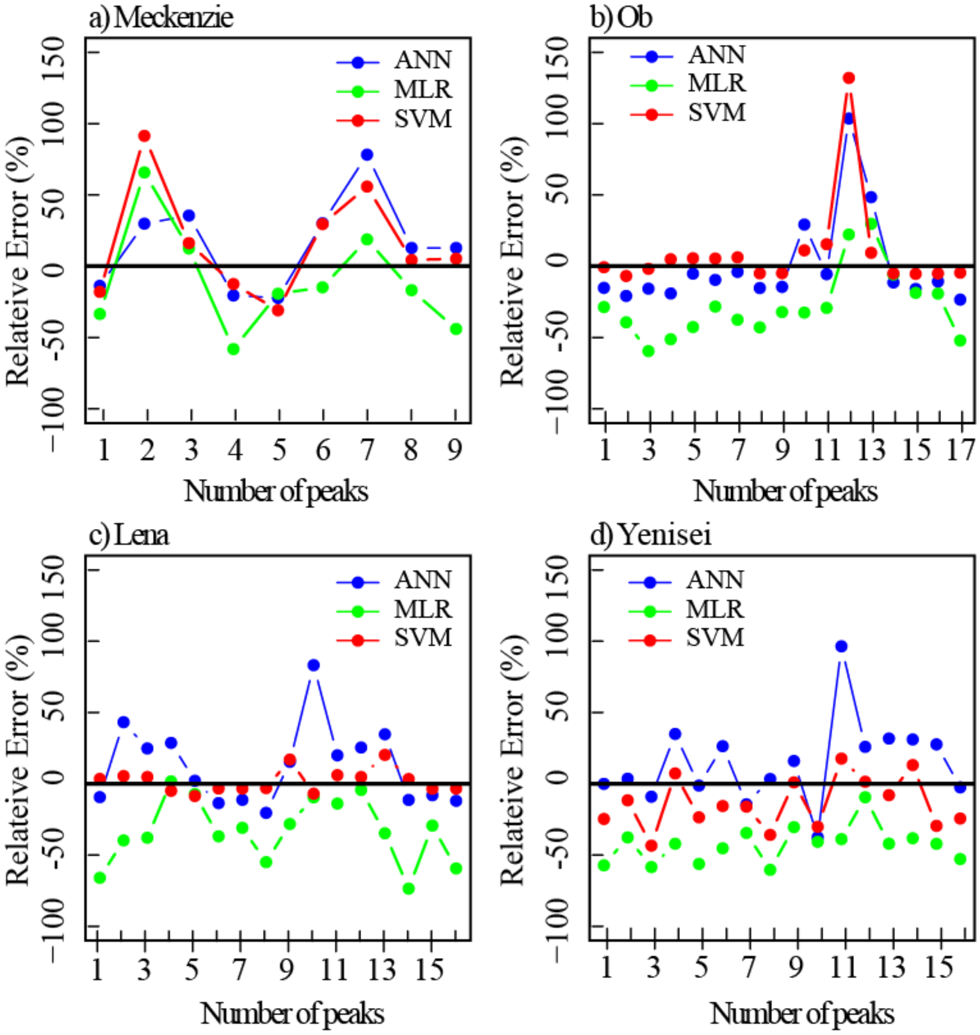

Figure 4-3 The relative errors of the simulated peak floods of the four river basins in the test months.

4.5 Projected changes in future flood derived from SVR models

The monthly streamflow from 2006 to 2100 were predicted based on four CMIP5 GCMs: ACCESS 1.0, CanESM2, HadESM2-ES, and MPI-ESM, under RCP 4.5 and RCP8.5 climate scenarios. The precipitation and temperature were firstly bias-corrected and downscaled to 0.5°×0.5° spatial resolution based on the CRU-TS 4.03 dataset. PET was estimated using the

Penman Monteith equation through the SPEI package of R (Vicente-Serrano et al. 2010). The time series of each predictor was area-averaged as the input of the validated SVMs. The monthly streamflow from 2006 to 2100 was predicted based on the four CMIP5 GCMs and the ensemble mean values are presented in Figures 4-4 and 4-5.

The predicted annual flow patterns for 2020s, 2050s, and 2080s under RCP 4.5 and RCP 8.5 climate scenarios are presented in Figure 4-4. The simulated monthly streamflow time series from 2006 to 2100 with seasonality removed are presented in Figure 4-5. It can be noted from Fig. 4-4 that under both RCP4.5 and RCP8.5, the spring peak floods of the four river basins show earlier timing of the spring peak flood in the annual flow patterns with the air temperature increasing, with differences in the magnitudes of the peak floods. And with the increasing of carbon emission, the spring peaks also increases for the pan-Arctic river basins such that the predicted spring peaks under RCP 8.5 scenarios is higher than that under RCP4.5 scenarios during the 2020s, 2050s, and 2080s, except in the Ob river basin. The effects of land cover changes on the streamflow may be the reason for the different changes of streamflow between Ob river and Lena river and Yenisei river that are located nearby. The permafrost extent of the Ob river basin is lower than that of the Lena or Yenisei river basins so that the effects of thawing permafrost under warming of the atmosphere on the streamflow are weaker.

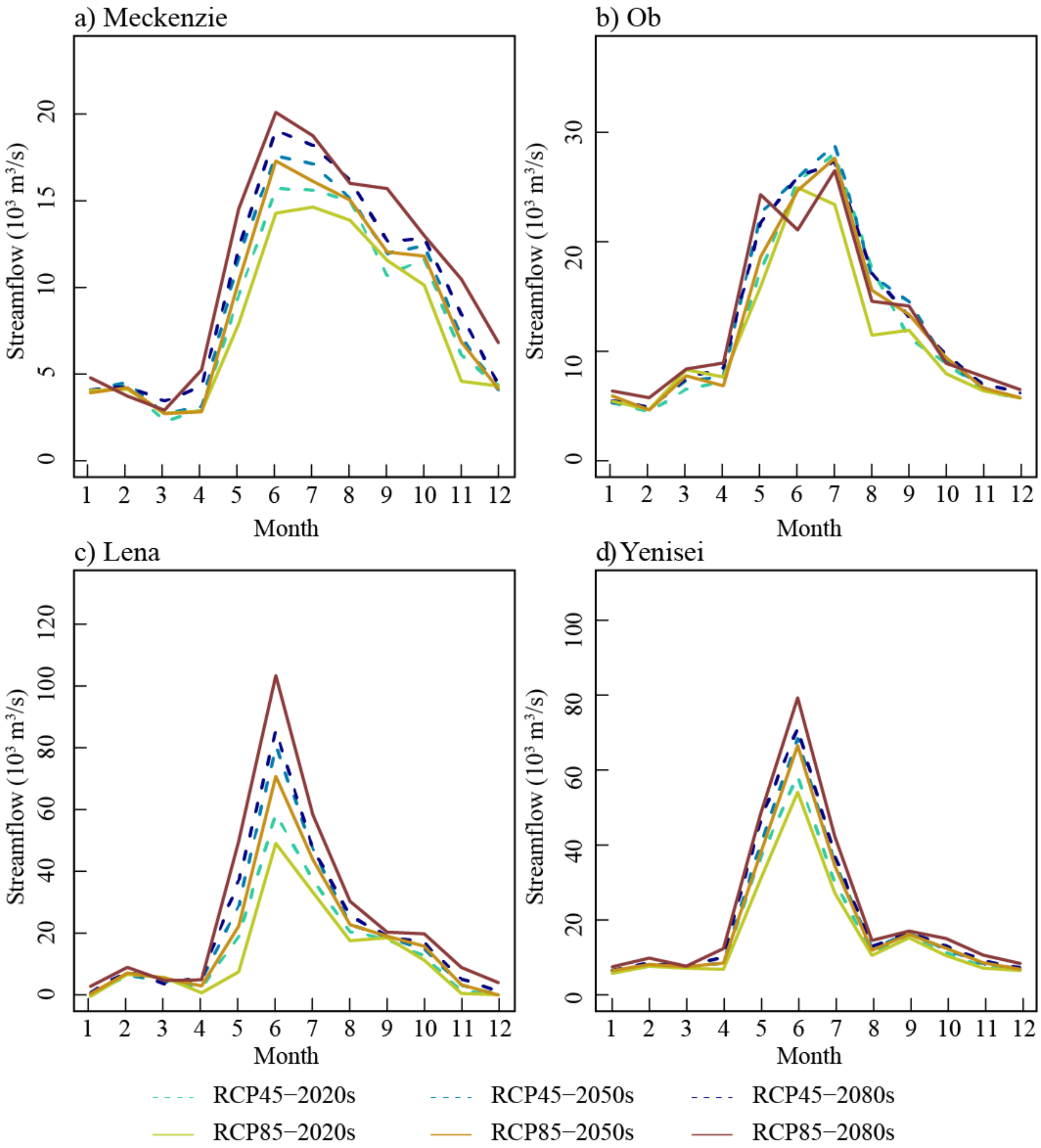

Figure 4-4. Monthly streamflow for 2020s, 2050s, and 2080s predicted from four GCMs under RCP45 and RCP85 for a) Mackenzie river, b) Ob River, c) Lena River, and d) Yenisei river. Dashed lines and solid lines show average monthly predicted streamflow from four CMIP5 GCMs: ACCESS 1.0, CanESM2, HadESM2-ES, and MPI-ESM, under RCP45 and RCP85 scenarios, respectively.

In Figure 4-5, the time series of monthly streamflow with seasonality removed from the four pan-Arctic river basins shows an increasing trend from 2006 to 2100. The magnitudes of these trends were different between the basins and between the different climate scenarios. For MRB, LRB, and YRB, the streamflow under RCP8.5 increases faster than under RCP4.5 that until the end of 2100, the streamflow increased by 100% under RCP8.5 comparing with the beginning of 2006, while for ORB, the streamflow increases at a similar rate under RCP4.5 and RCP8.5 that the streamflow increases by around 50%.

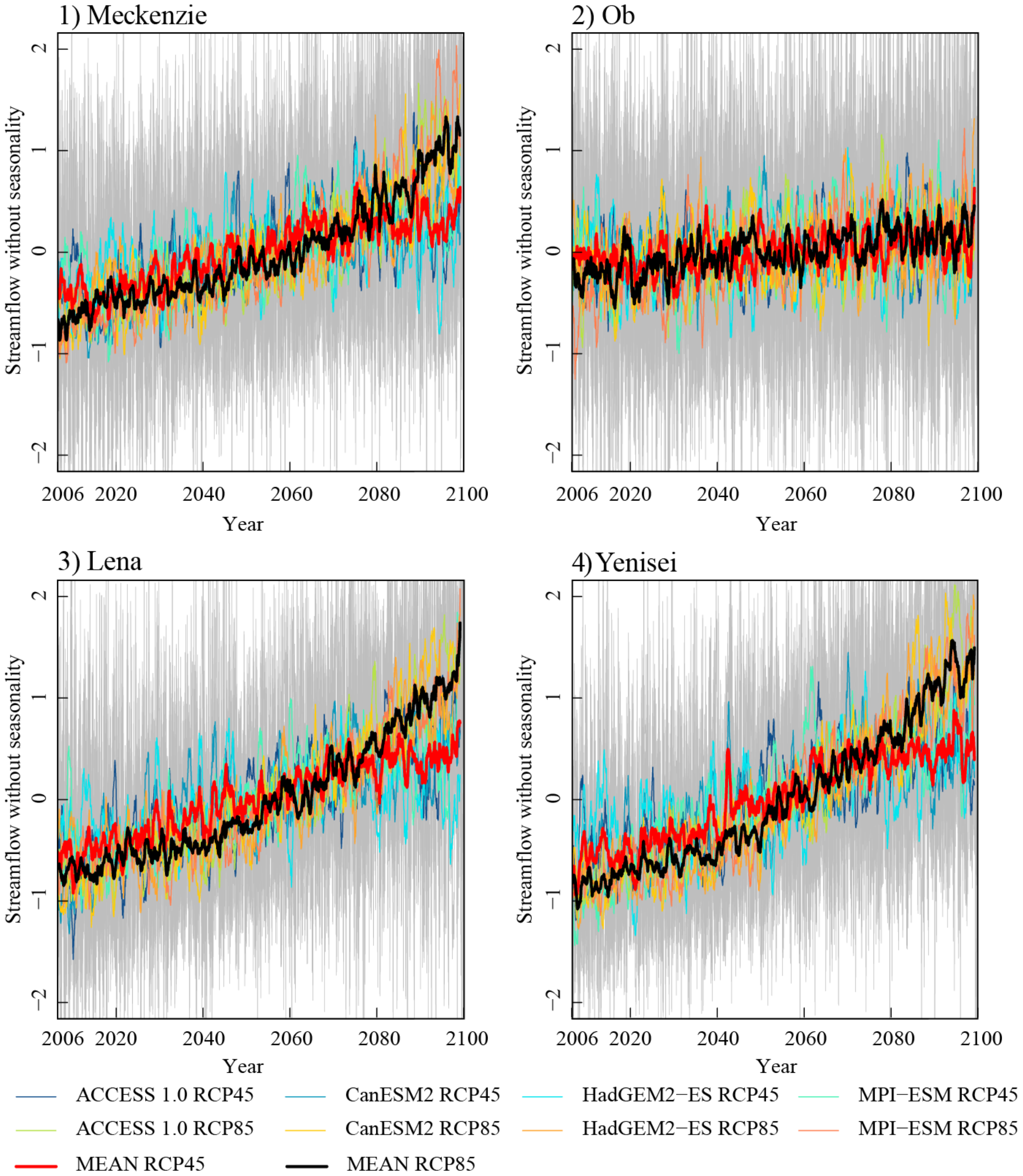

Figure 4-5. The predicted monthly streamflow from 2006 to 2100 by SVM. The grey curves are the predicted monthly streamflow (with seasonality removed) based on the four CMIP5 GCMs. The seasonality was removed by subtracting the monthly mean and divided by the monthly standard variation. Curves in color were the 12-month moving average of the seasonality-removed monthly streamflow predicted from four GCMs under

RCP4.5 and RCP8.5, respectively. The red and black curves denote the ensemble means of the 12-month moving average of monthly streamflow predicted from the four GCMs under RCP4.5 and RCP8.5, respectively.

4.6 Conclusions

Under global warming and climate change, streamflows around the world have changed but to different extents. The pan-Arctic river basins contribute more than one third of the freshwater into the Arctic Ocean, freshwater that plays an important role in the oceanic circulation. However, due to the limitation of observations, streamflow simulations and predictions over the pan-Arctic river basins are inadequate. Different with the hydrological models that have high requirement on the hydrological and climatological parameters, the machine learning models are faster and easier to calibrate and validate. Therefore, widely-used machine learning models were applied to the simulation of streamflows from the pan-Arctic river basins. This study evaluated the performance of the widely-used machine learning model, Support Vector Regression model, on the simulation of monthly streamflow at the outlets of four great pan-Arctic river basins: Mackenzie river basin, Ob river basin, Lena river basin, and Yenisei river basin. Its performance was compared with Artificial Neural Network model and Multi-Variable Regression model. Results show that SVM and ANN have similar capabilities on the monthly streamflow, and both are better than MLR, but the calibration and validation of SVM is several times faster than ANN. Then the validated SVMs were used to predict the monthly streamflow based on four CMIP5 GCMs: ACCESS 1.0, CanESM2, HadESM2-ES, and MPI-ESM, under RCP4.5 and RCP8.5 climate scenarios during the periods of 2006 to 2100. The predicted streamflow shows a significant increasing trend for all four river basins but with different magnitudes. These increasing trends were amplified by the increasing of air temperature and carbon emissions under RCP8.5 than under RCP4.5. The results show that with the increasing temperature, the monthly streamflow of the four great pan-Arctic river basins have significantly increasing trends and with the increasing carbon emission, the increasing trends were amplified. In the annual streamflow patterns, the spring peak flood of each basin occurs earlier and has higher volumes with higher air temperature and carbon emissions. Amongst the river basins, the increasing trends are different. These differences may be the result of the different spatial-temporal land surface within basins, such as the permafrost, vegetation, and snow cover. Further research to attribute the changes of streamflow could be the simulation of the spatial changes of land cover and the relationship with hydro-climatology, which have high requirements on hydrological and climatological datasets.

Chapter 5. Probabilistic Characteristics of extreme wet and dry spells over Siberian river basins using Copulas functions

5.1 Introduction

Wet spells and dry spells, defined as episodes of consecutive rainy or non-rainy days (Ratan and Venugopal 2013), characterize the day-to-day variability of precipitation (Li et al. 2016b). They have been widely studied in recent decades as an important indicator of extreme events that have significantly changed globally under climate change (Froidurot and Diedhiou 2017; Gitau et al. 2018; Nabeel and Athar 2018; Sun et al. 2017; Vinnarasi and Dhanya 2016). Long dry spells during winter in the Mediterranean Basin tend to be a natural hazard with strong socioeconomic impacts (Raymond et al. 2018), and they have shown an increasing trend in the mean duration, spatial extent and frequency in recent years (Raymond et al. 2019). In tropical regions, a major contribution to seasonal rainfall for arid regions comes from 1-5 day wet spells, while for humid regions, this contribution could come from wet spells of durations as long as 30 days (Ratan and Venugopal 2013). In China, good regression relationships were found between the number of dry/wet spells and spell length, as well as precipitation amount and wet spell length (Li et al. 2017). At smaller spatial scales, the variability of wet and dry spells clearly reflects the impact of natural climate variability on the water availability over a region. At annual time scale, significant increasing trends have been detected in general and the characteristics of wet spells in many parts of the world have become more extreme. When El Niño is active, dry spells during the Asian southwest monsoon season tend to get drier (Li et al. 2016b). In recent years, durations of wet spells exhibit a statistically significant increasing trends over central European Russia, especially during winters when the mean duration of wet spells has increased by 15%-20%, although summer wet spells have become shorter over northern Russia (Zolina et al. 2013). Ye (2018) has analyzed the characteristics of wet and dry spells over Siberia and its relationship with air temperature using a simple linear regression. Ye (2018) shows that both the durations of the mean and extremes of summer dry periods have increased with air temperature at about 7.0% (0.24 day/◦C) and 7.7% (0.86 day/◦C) respectively, but those of wet periods have decreased at about 1.3% (-0.02 day/◦C) and 2.2% (-0.10 day/◦C), respectively. She also found that locations with longer durations of dry spells tend to experience faster rates of warming, which implies the likelihood of worsening drought severity in drier and/or warmer locations for all seasons in Siberia.

Copulas function have been widely used in the probability analysis of hydrology variables. The advantage of low constraints on the choice of marginal distribution that allows the marginal distributions belong to different families makes Copulas functions being widely used to model the multivariable joint distribution (Mirabbasi et al. 2012; She et al. 2016; Yu et al. 2014). Moreover, copulas are also flexible in describing the dependence structure, extending to multi-variables, and allowing for separate analysis of marginal distributions and dependence structure (Chen et al. 2015). Arya Farid and Zhang (2017) used the copula method for modeling the water quality time series. Qian et al. (2018) used the copula method for extreme precipitation simulation. Yin et al. (2018) assessed the implication of climate change to the future quantiles of flood peak and volume in Ganjiang river basin, China. Sarhadi et al. (2016) proposed a dynamic risk analysis method for droughts by combining Bayesian theory with copula functions that could capture time-varying risks of suffering from extreme drought. These studies indicate that the copula method can be an effective tool for the stochastic simulation of hydrological data.

The objective of this study is to analyze the probabilistic characteristics of the dry and wet spells in three great Siberian river basins from the aspect of duration and temperature, and assess the risk of suffering from extreme dry and wet spells. In this study, four continuous probability distribution were fitted to the temperature of the dry and wet spells, including the two-parameter Gamma, generalized extreme value (GEV), three-parameter lognormal and Weibull distribution; two-parameter negative binomial distribution and Poisson distribution were employed to fit the duration of dry and wet spells. Then three types of Archimedean copulas: Frank, Gumbel, and Clayton copulas function, were employed to fit the empirical joint probability distribution of the duration and temperature of dry and wet spells. Based on their performance estimated by RMSE, the best copulas function were used to generate the conditional and joint probability distribution under scenarios of extreme duration and temperature. The risk of suffering from extreme dry and wet spells were revealed by the return period. From the spatial distribution of the conditional and joint return period, the regional likelihood of suffering from extreme dry and wet spells were revealed.

This chapter is organized as follows: the dry/wet spells of the study area are introduced in section 5.2; the details of the copulas function are described in section 5.3; the details of the marginal distribution fitness and the joint copulas, as well as the return periods under four extreme scenarios are given in section 5.4; and conclusions are shown in section 5.5.

5.2 Study Site and Data

5.2.1 Study area and dry/wet spells

Three major Siberian river basins, the: Ob, Yenisei, and Lena river basins, located west of the Ural Mountains, are selected as the study sites. Figure 5-1 shows the digital elevation maps of these sites. Most or the areas are plains lower than 500m above sea level with small mountainous areas located at the southern and the western ends. 221 climate stations with longer than 30 years of continuous daily precipitation and temperature observations (less than 1 month of missing observations) are selected for this study, as shown in Figure 5-1. Stations outside the outline were also used for spatial interpolation to avoid marginal effect. Consecutive days with precipitation higher than 0.1 mm were recorded as wet spells and the average daily temperature of these rainy days is the corresponding temperature of the wet spell. Previous studies considered both1mm and 0.1 mm as threshold to define the wet spells and have similar results(Zolina et al. 2013). Since Russia has a significant number of days with less than 1mm rainfall, this study uses 0.1mm as threshold to define wet spells. Similarly, the duration of a dry spell is the number of consecutive dry (no rain) days and the average daily temperature is the temperature of the dry spell.

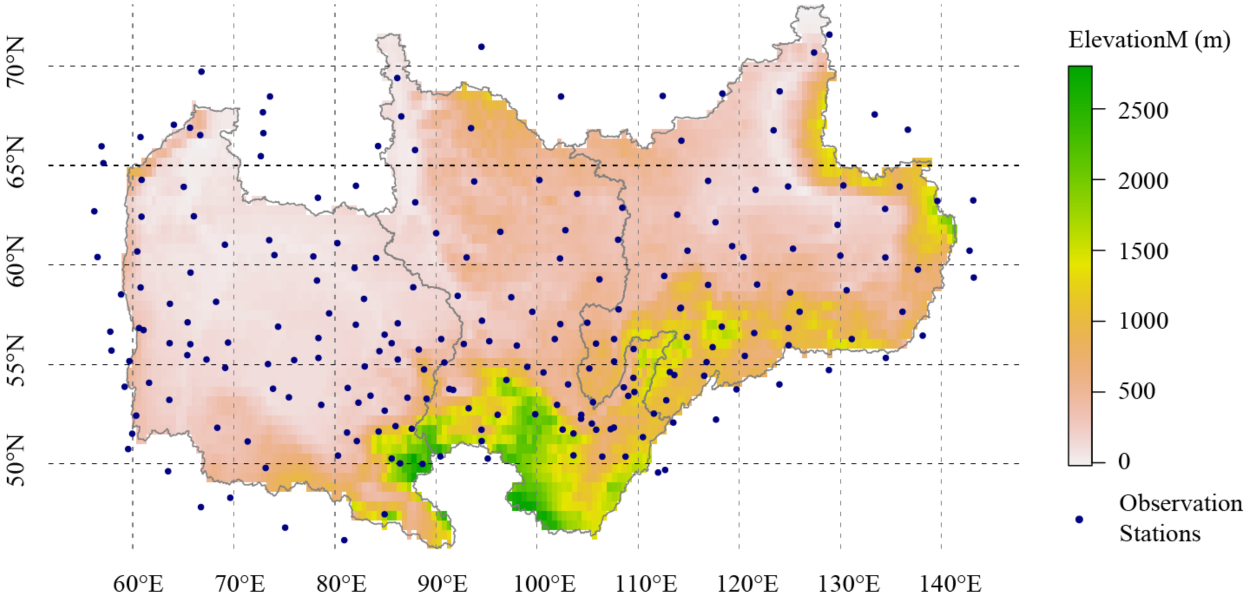

Figure 5-1. DEM of the study area and the locations of weather stations

The mean temperature and duration of the dry and wet spells are plotted as scatterplots. From figure 2, it is obvious that both mean duration and temperature of dry spells are generally higher than that of wet spells and the relationship between duration and temperature of dry spells is predominantly positive, while that of wet spells is negative.

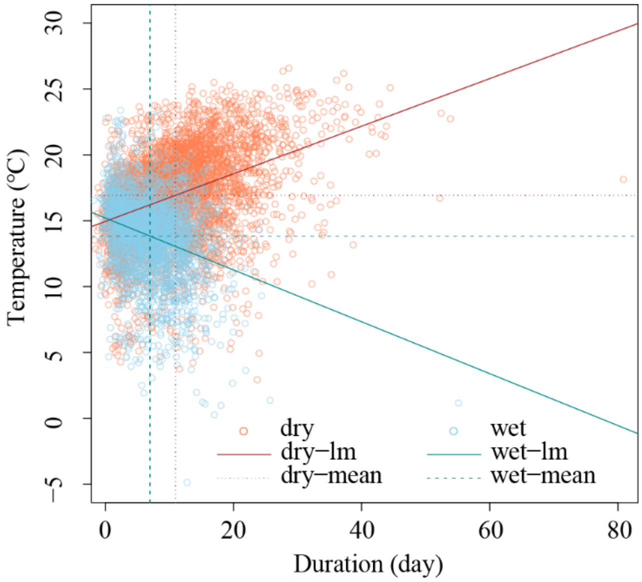

Figure 5-2. Scatterplot of the mean duration and mean temperature of dry and wet spells from 221 stations that each scatter represent a station. The solid lines, denoted as "dry-lm" and "wet-lm", indicate the linear regression lines of the duration and temperature of dry and wet spells, respectively. The dashed and dotted lines, denoted as "dry-mean" and "wet-mean", indicate the mean duration and temperature of all 221 stations for dry and wet spells, respectively.

The mean duration and temperature of the dry and wet spells are presented in Figure 5-3. The mean duration of dry spells observed in the 221 stations is 3.15 days, and the mean temperature is 15.07 °C (Fig. 5-2). Further, Figure 5-3a shows that the duration of dry spells ranges from one to five days although most are 3 or longer (except in the Stanovoy Range). The variability of the mean temperature of dry spells ranges from about 10 °C in the northeast to 25 °C in the southwest. For wet spells, the mean duration is 2.56 days, and the mean temperature is 14.98 °C (Fig. 5-2). From figure 3b, the mean temperature of wet spells decreases from the southwest to the northeast, similar to that of dry spells. The durations of wet spells are longer over the Stanovoy Range, which is opposite to the dry spell durations.

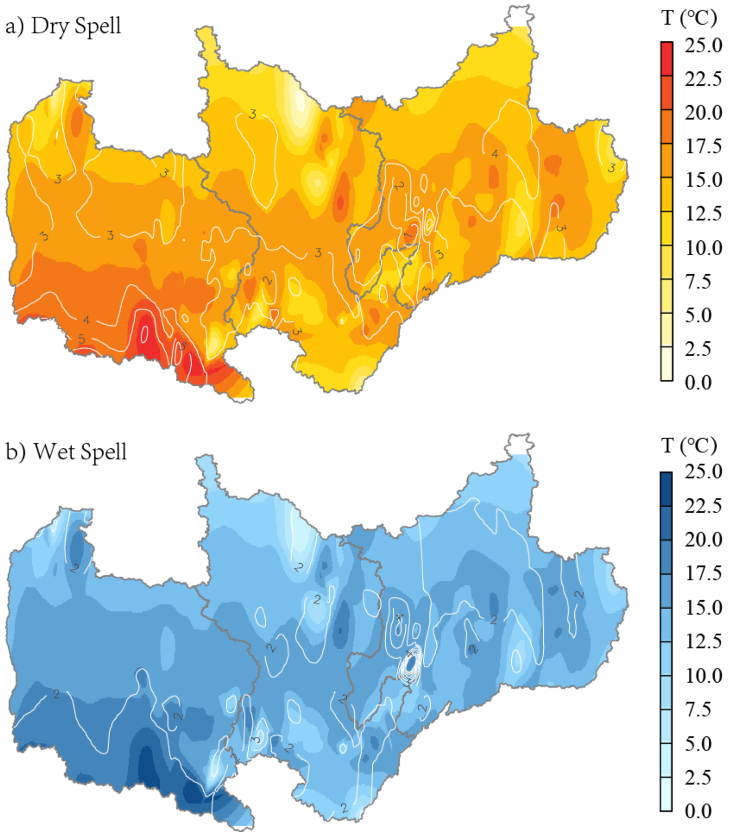

Figure 5-3. The spatial distribution of the duration and mean temperature of the dry and wet spells over the three Siberian river basins, the Ob, Yenisei, and Lena river basins. The mean temperature is shaded, while contours in white indicate the mean duration (days) of dry and wet spells.

5.2.2 Marginal distributions for duration and temperature of dry and wet spells

Several continuous probability distributions are tested as the marginal distributions of the temperature of dry and wet spells, which include two-parameter Gamma, generalized extreme value (GEV), three-parameter lognormal and the Weibull distribution. Two discrete probability distributions are tested as marginal distributions of the duration of dry and wet spells, which include a two-parameter negative binomial distribution and a Poisson distribution. Parameters of these probability distributions are estimated by the maximum likelihood method, which is relatively robust compared to methods such as the method of moment. The goodness-of-fit of these probability distributions (PD) is evaluated by the Kolmogorov–Smirnov's statistic Distance

(Zhang et al. 2015a) at a 95 % confidence level to reject or to accept a PD fitted to a set of data. The PD with the highest goodness-of-fit based on K-S Distance statistics is selected for each climate station.

5.3 Bivariate Copulas

Introduced by Sklar (1959), copulas can link univariate marginal distributions to multidimensional distributions. According to the theorem, if two random variables x and y follow the arbitrary marginal distribution functions $\mathrm{F}_x(\mathrm{x}) = \mathrm{P}[\mathrm{X} \leq \mathrm{x}]$ and $\mathrm{F}_y(\mathrm{y}) = \mathrm{P}[\mathrm{Y} \leq \mathrm{y}]$ separately (Chen et al. 2015), there must exist a copula C to combine the marginal distribution functions in a bivariate framework, with its general form as (Zhang et al. 2015a):

$$\mathrm{F}_{x,y}(\mathrm{x},\mathrm{y}) = C_p(\mathrm{F}_x(\mathrm{x}), \mathrm{F}_y(\mathrm{y})) \tag{5-1}$$

If the marginal cumulative probability distribution $\mathrm{F}_x(\mathrm{x})$ and $\mathrm{F}_y(\mathrm{y})$ are continuous, the copula function C_p is unique with the following joint probability density function:

$$\mathrm{f}_{x,y}(\mathrm{x},\mathrm{y}) = \mathrm{c}(\mathrm{F}_x(\mathrm{x}), \mathrm{F}_y(\mathrm{y}))\mathrm{f}_x(\mathrm{x})\mathrm{f}_y(\mathrm{y}) \tag{5-2}$$

where $\mathrm{f}_x(\mathrm{x})$ and $\mathrm{f}_y(\mathrm{y})$denote the density functions corresponding to $\mathrm{F}_x(\mathrm{x})$and $\mathrm{F}_y(\mathrm{y})$, respectively. c is the density function of C which can be expressed as follows:

$$\mathrm{c}(\mathrm{u},\mathrm{v}) = \frac{\partial^2 C(u,v)}{\partial u \partial v} \tag{5-3}$$

where u and v are the univariate cumulative distribution functions.

In hydrology, the Archimedean Copulas are the most widely used function, such as in the frequency analysis and risk management of floods (Li and Zheng 2016; Sraj et al. 2015), droughts (Sarhadi et al. 2016; Zhang et al. 2015a), extreme precipitation events (Zhang and Singh 2007), and risk management and water engineering (Arya Farid and Zhang 2017; Qian et al. 2018). There are three types of Archimedean Copulas, which include Clayton, Gumbel-Hougaard and Frank. The function of copulas and the relationship between the copulas parameter θ and the Kendall parameter τ are listed in Table 5-1. Copulas parameter θ measures the degree of association between the two marginal variables, while Kendall's τ describes the dependency between the two marginal variables.

Table 5-1. Functions and parameters of three types of Copula (Zhang et al. 2015a)

Copula types	Functions	Relationship between τ and θ
Clayton	$\mathrm{C(u,v)} = (u^{-\theta} + v^{-\theta} - 1)^{-1/\theta}$	$\tau = 1 + \frac{\theta}{\theta + 2}, \theta \in [1, \infty)$
Gumbel-Hougaard	$\mathrm{C(u,v)} = \exp\{-[(-lnu)^{\theta} + (-lnv)^{\theta}]^{-1/\theta}\}$	$\tau = 1 - \frac{1}{\theta}, \theta \in [2, \infty)$
Frank	$\mathrm{C(u,v)} = -\frac{1}{\theta}\ln[1 + \frac{(e^{-\theta u} - 1)(e^{-\theta v} - 1)}{e^{-\theta} - 1}]$	$\tau = 1 + \frac{4}{\theta}[\frac{1}{\theta}\int_{0}^{\theta} \frac{t}{e^{t} - 1} dt - 1], \theta \in R$

5.3.1 Goodness-of-fit tests

To evaluate the efficiency of copula functions and the cumulative sample distributions, the empirical copula function is introduced. If $(\mathrm{X}_i, \mathrm{Y}_i), (\mathrm{i} = 1, 2, \ldots, \mathrm{n})$ are samples from a two-dimensional distribution, $(\mathrm{X}_i, \mathrm{Y}_i)$, $\mathrm{F}_x(\mathrm{x})$ and $\mathrm{F}_y(\mathrm{y})$ are the empirical cumulative distribution functions of X and Y, respectively. The empirical copulas can be written as:

$$C_e(\mathrm{u,v}) = \frac{1}{n}\sum_{i=1}^{n} I_{[F_n(x_i) \le u]} I_{[F_n(y_i) \le v]}, u, v \in [0,1] \tag{5-4}$$

where n is the size of the time series, $I_{[*]}$is the indicator function, that is equal to 1 when $F_n(x_i) \le u$, or it equals to zero otherwise.

The root-mean-square error (RMSE), a measure of differences between values predicted by the empirical and the theoretical copula, is expressed as:

$$\text{RMSE} = \sqrt{\frac{1}{n}\sum_{i=1}^{n}[C_p(i) - C_e(i)]^2} \tag{5-5}$$

where n is the sample size , C_p is the calibrated value of the theoretical copula and C_e is the observation of the probability gained from the empirical copula. A small RMSE represents an efficient empirical model and vice versa.

5.3.2 Joint return period of the duration and the temperature

Let T denotes the extreme mean temperature and D the duration of a spell from the long-term of observation defined through quantile values. The return period with a longer than or equal to a certain duration and a warmer than or equal to a certain temperature can be defined as:

$$\mathrm{T}_D = \frac{E(L)}{1-F_D(d)}$$

$$\mathrm{T}_T = \frac{E(L)}{1-F_T(t)} \tag{5-6}$$

where T_D and T_T is the return period for the temperature and duration of the spells; $E(L)$is the expected extreme dry/wet spells inter-arrival time.

$$\mathrm{T}_{DT} = \frac{E(L)}{P(D\geq d, T\geq t)} = \frac{E(L)}{1-F_D(d)-F_T(t)+C(F_D(d),F_T(t))}$$

$$\mathrm{T}'_{DT} = \frac{E(L)}{P(D\geq d \text{ or } T\geq t)} = \frac{E(L)}{1-C(F_D(d),F_T(t))} \tag{5-7}$$

where T_{DT} is the return period for $D \geq d$ and $T \geq t'$, here t means the specific temperature value and T'_{DT} is the return period for $D \geq d$ or $T \geq t$.

5.4 Results

5.4.1 Marginal distributions of duration and temperature of dry/wet spells

For each climate station, the duration of dry and wet spells (in days) were first fitted with two discrete probability distributions, the Poisson and two-parameter negative Binomial distributions, while the temperature of dry and wet spells were fitted with four continuous probability distributions: two-parameter Gamma; generalized extreme value (GEV); three-parameter lognormal, and; Weibull distributions. The K-S distance between the fitted theoretical and the empirical cumulative probability distributions were calculated and presented as histograms, shown in Figure 5-4. The histograms of duration and temperature for dry and wet spells show that the temperature of both dry and wet spells for most stations is better fitted with a GEV than the other three probability distributions, while the duration is better fitted with a negative-Binomial than a Poisson distribution.

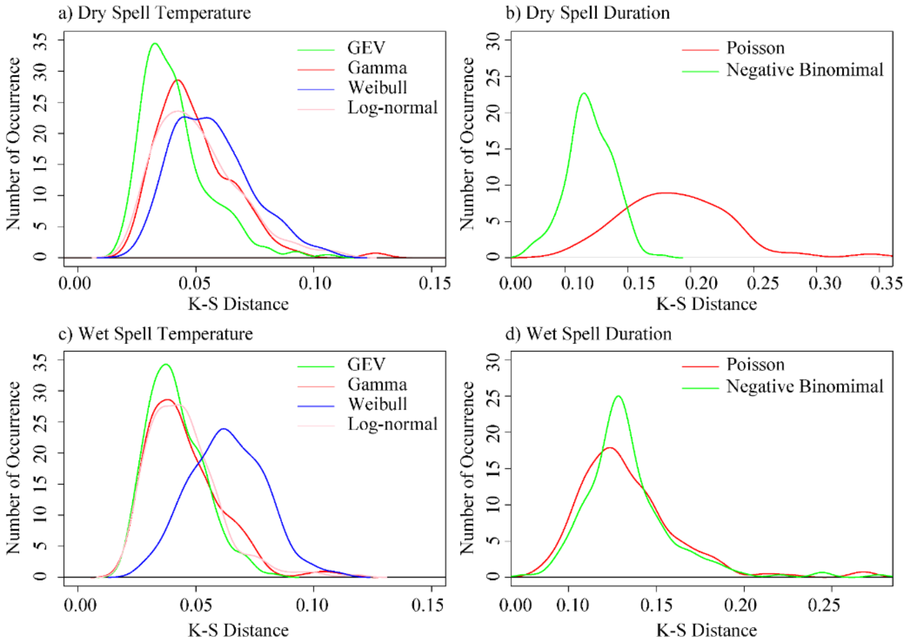

Figure 5-4. Histogram of K-S Distance between the theoretical cumulative distribution function (CDF) of and the empirical cumulative distribution function of duration and temperature of dry and wet spells.

Station No. 29313, located at 57.57ºE, 79.43ºN within the Ob river basin, is chosen to illustrate the procedures to fit the data with marginal distributions. The duration and the temperature of dry and wet spells were estimated from the 1966-2019 daily precipitation and temperature data of the three Siberian basins. In Table 5-2, smaller goodness-of-fit statistics (K-S distance) represent better fits and vice versa. The empirical cumulative and the fitted theoretical cumulative probability distributions are compared in Figure 5-5.

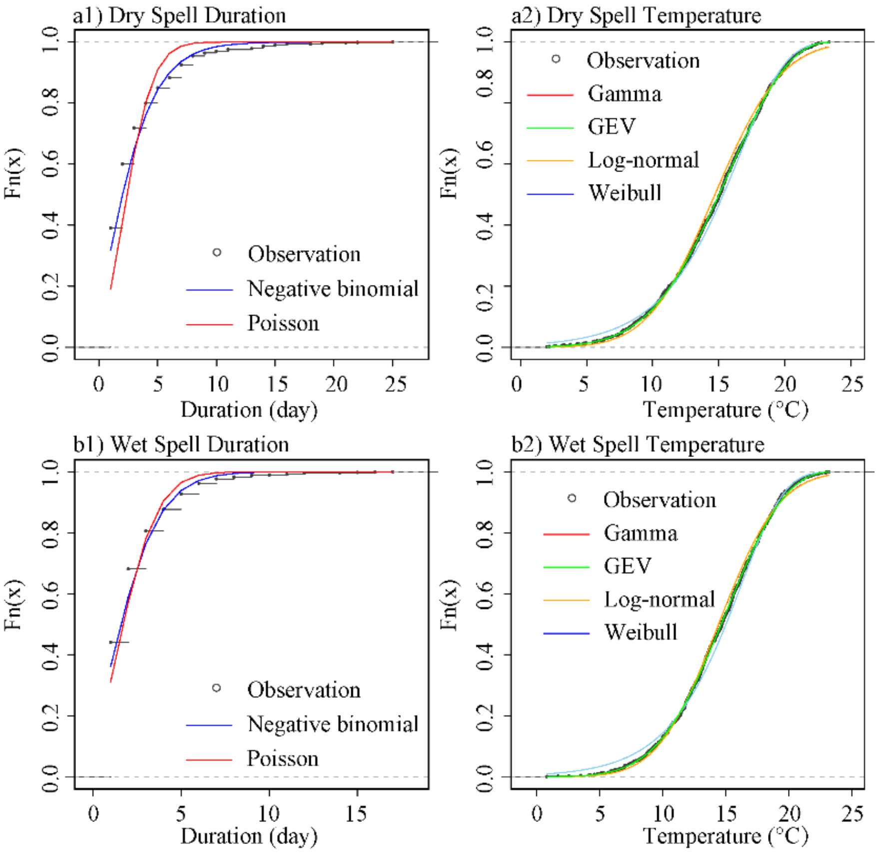

Figure 5-5. Marginal probability distribution of the duration (*1) and temperature (*2) of dry (a*) and wet (b*) spells at No. 29313 stations (57.57°E, 79.32°N). The duration time series were fitted with two discrete distributions, Negative-binomial and Poisson distributions, while the temperature time series were fitted with four continuous distributions: Gamma; GEV; Log-normal, and; Weibull distributions.

Compared to other probability distributions, the negative binomial and the GEV distributions produce the smallest K-S distance, which show that the negative binomial distribution is the best probability distribution to model the duration of extreme dry/wet spells and GEV is the best to model the temperature of extreme dry/wet spells.

Table 5-2. Goodness of fit based on K-S D for the duration and temperature at No.29313 station

Station	Spell	Duration		Temperature			
		Poisson	Negative-binomial	GEV	Log-normal	Weibull	Gamma
29313	Dry	0.213	0.133	0.039	0.065	0.075	0.047
57.57°E, 79.43°N	Wet	0.136	0.124	0. 023	0.391	0.060	0.026

Given the three-parameter GEV is selected as the theoretical probability distribution in modeling the temperature of dry and wet spells, the location, scale, shape parameters of GEV for each station are interpolated to obtain the spatial distributions of a*,b*, and c* shown in Figure 5-6. Overall, the location parameters of the GEV distribution fitted to temperature data increase from northeast to southwest and from coastal regions to the inland for both dry and wet spells with the highest value located in the northwest of the Altay Mountains (Fig. 5-6a1 and a2). The scale parameters increase from south to north and from inland to the coastal regions with the highest values located north of the mountainous region upstream of the Yenisei river basin (the Mungaragiyn-Gol Ridge) (Fig. 5-6b1 and b2). Most of the study areas have negative shape parameters that implies the mean temperature of dry and wet spells of the three Siberian river basins can be modeled by GEV Type III distribution with heavy tails.

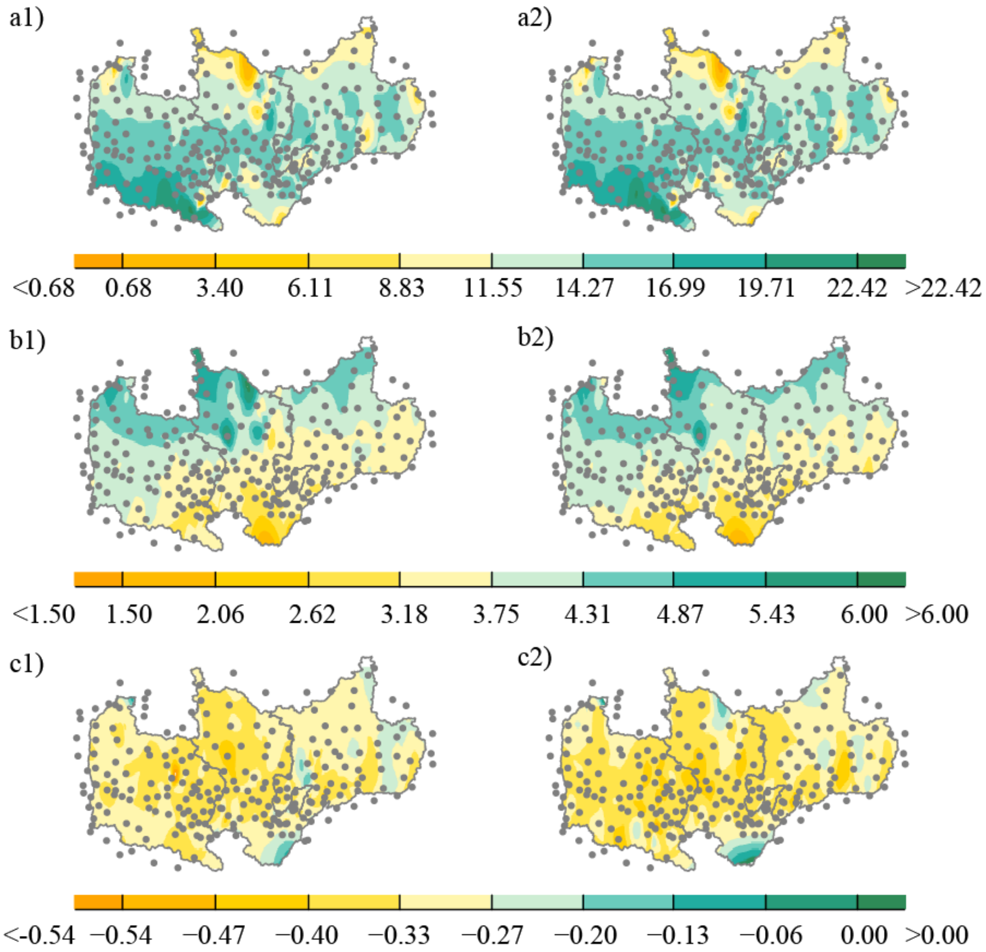

Figure 5-6. Spatial distributions of the parameters of the marginal distribution of duration and temperature of dry and wet spells. The left and right columns indicate dry and wet spells, respectively. a1, a2) panels are the location parameters of the GEV distribution fitted for the temperature of dry and wet spells, respectively; b1, b2) panels are the scale parameters of the GEV distribution fitted for the temperature of dry and wet spells, respectively; c1, c2) panels are the shape parameters of the GEV distribution fitted for the temperature of dry and wet spells, respectively.

5.4.2 Joint probability distributions of duration and temperature

The joint probability distribution of the duration and the temperature of the extreme dry and wet spells is determined by copulas. The Clayton, Frank and Gumbel-Hougaard are selected as candidates for the joint distribution of the duration and temperature of dry and wet spells. The parameters of these three types of copula function are estimated based on their relationships with the Kendall's rank coefficient, which together with the copula parameters of the 221 stations within and around the outline of the study area are listed in Appendix 2. Appendix 2 shows that for most stations, the Gumbel copulas produces the minimum error for the dry spells, while the Clayton copulas perform better than others for the wet spells. Therefore, Gumbel copulas are selected to develop the joint distribution of the duration and temperature of dry spells, while Clayton copulas are used to develop the joint distributions of duration and temperature of wet spells. The joint distribution of the N0. 29313 station in Figure 5-7 is used as an example.

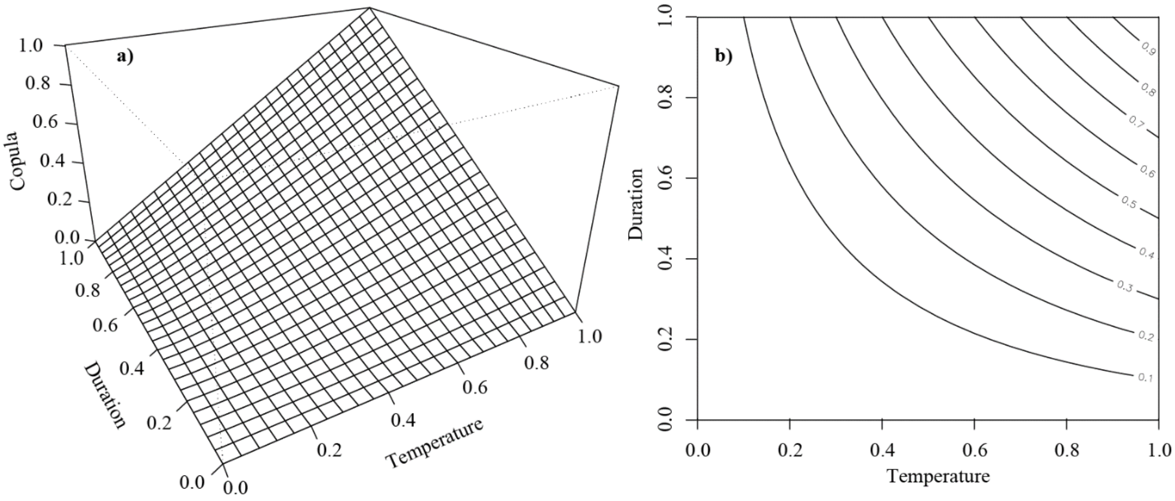

Figure 5-7. Surface plot and contours from the surface plot of the joint cumulative probability function of duration and temperature of dry spells at No. 29313 station modeled by Gumbel-Hougaard copula with the parameter θ= 1.265.

5.4.3 Spatial probability distributions of duration and temperature of dry/ wet spells of different return periods

The spatial probability distributions of the duration and temperature for dry and wet spells of certain return periods can be interpolated from the marginal probability distributions of the 221 climate stations, shown as shaded contours in Figures 5-8 and 5-9, respectively. According to Eq.

6, the return period of 5-years, 10-years, 20-years, and 50-years correspond to 80%, 90%, 95%, and 98% quantile of the marginal probability distribution. For 5-year return period, the mean temperature of dry spells for all stations is 18.28 °C, and the lowest value is 8.92 °C located in the Central Siberian Plateau at the downstream of Yenisei river basin, while the highest value is 25. 17 °C located in the northwest Altay Mountains. Figure 5-8. a1 shows that temperature increases from east to west while the 5-year return period duration increases from 3 days to 14 days with a mean value of 2.76 days. The highest duration is located in the northwest Altay Mountains, while the lowest values is located around the Stanovoy Range (Fig. 5-8. a2). For 10-year return period, the temperature of dry spells ranges from 10. 44°C to 26. 31 °C with mean value of 19.69 °C, and the duration ranges from 3.7 days to 21.2 days with a mean duration of 6.96 days. The spatial distribution of 10-year return period is similar to that of 5-year return period (Fig. 5-8. b1, b2). For 20-year return period, the temperature ranges from 11. 33 °C to 27. 25 °C, with a mean temperature of 20. 77 °C, and the duration ranges from 5 days to 27 days, with a mean duration of 9.21 days (Fig. 5-8. c1 and c2). The spatial distribution of 50-years return period duration is evenly distributed and the northwest of Altay Mountains has dry spells with relatively longer duration (Fig. 5-8. d2). From the spatial distribution of marginal probability distributions, it seems that the northwest of Altay Mountains and Dzhugdzhur Mountains, located at the southeast of Lena river basin are more likely to suffer from long duration of dry spells with relatively higher temperature, while Stanovoy Range has a relatively shorter duration and lower temperature during dry spells.

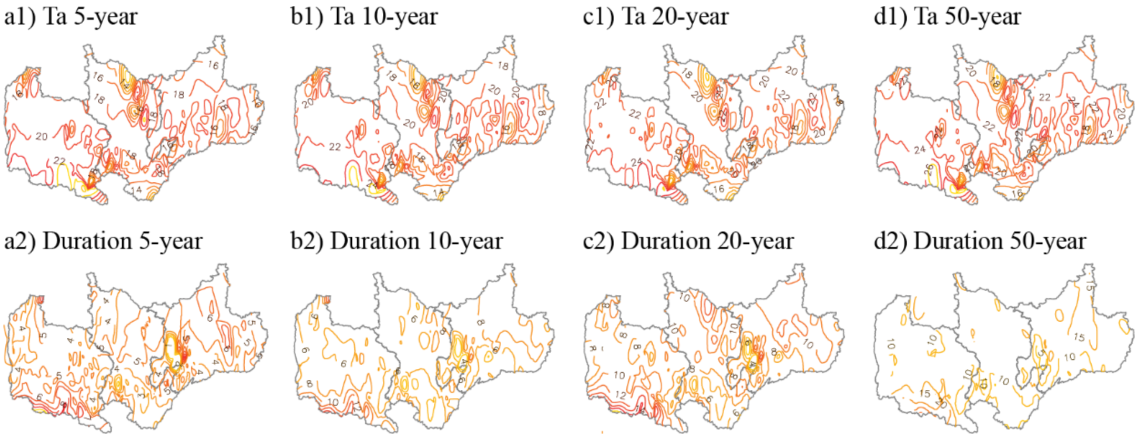

a1) Ta 5-year b1) Ta 10-year c1) Ta 20-year d1) Ta 50-year

a2) Duration 5-year b2) Duration 10-year c2) Duration 20-year d2) Duration 50-year

Figure 5-8. The spatial distribution of the return period of the duration and temperature of the dry spells of the three great Siberian river basins. a1, a2) 5-years return periods value of the mean temperature and duration of dry spells; b1, b2) 10-years return periods value of the mean temperature and duration of dry spells; c1, c2) 20-years return periods value of the mean temperature and duration of dry spells; d1, d2) 50-years return periods value of/ the mean temperature and duration of dry spells.

Figure 5-9 presents the temperature and duration of wet spells at 5-year, 10-year, 20-year, and 50-year return periods. The temperature at 5-years return period at site-scale varies from 8.8^{o}C to 25.4^{o}C with the mean value of 18.19^{o}C (Fig. 5-9. a1). For 10-years return period, the temperature of wet spells varies from 10.44^{o}C to 26.3^{o}C with average of 19.69^{o}C (Fig. 5-9. a2); that of 20-years return period ranges from 11.33^{o}C to 27.25^{o}C with average of 20.77^{o}C (Fig. 5-9. a3); and that of 50-years return period have a range of 12.52^{o}C-28.03^{o}C with mean value of 21.84^{o}C (Fig. 5-9. a4). Spatially, the Ob river basin has a higher temperature by about 2 ^{o}C than the Yenisei and Lena river basins (Fig. 5-9. a*). The duration of wet spells as similar range as dry spells: the duration of 5-year return period ranges from 3 to 14 days; that of 10-years return period ranges from 3.7 to 21.2 days; that of 20-year return period ranges from 5 to 27 days; and that of 50-year return period ranges from 6 to 35 days. The average duration of the wet spell at 5-, 10-, 20-, and 50-year return periods are 4.76, 6.96, 9.21, and 12.23 days, respectively. The duration of wet spells at the four return periods distributes more evenly spatially than that of dry spells because long duration and high temperature of wet spells concentrate in the Stanovoy Range for all four return periods (Fig. 5-9 *2).

a1) Ta 5-year b1) Ta 10-year c1) Ta 20-year d1) Ta 50-year

a2) Duration 5-year b2) Duration 10-year c2) Duration 20-year d2) Duration 50-year

Figure 5-9. Same as Figure 5-8, but for wet spells.

Over all, from the marginal distributions of the duration and temperature of dry and wet spells estimated from historical data, it seems that these three Siberia river basins, the northwest of Altay Mountains and part of Central Siberian Plateau at the downstream of Yenisei river basins are likely to suffer from both dry and wet spells with longer durations and warmer temperature than other areas. Stanovoy Range is likely to have dry and wet spells of shorter durations and colder temperature than other areas. As extreme conditions continue to increase, the probability of the upstream region of the Lena river basin suffering from dry and wet spells with warmer temperature will likely increase significantly.

5.4.4 Spatial probability distributions of joint dry/wet spells return periods

Based on the method of (Salvadori and De Michele 2004), the return period of the bivariate, duration and temperature of dry and wet spells corresponding to certain concurrent durations and temperature, and at least one of the two variable corresponding to the value, are estimated. The spatial distributions of specific duration and temperature of 5-, 10-, 20-, and 50-year return periods for dry and wet spells are estimated. The conditional and joint return periods of dry and wet spells are shown in Figures 5-10 and 5-11, respectively.

Figure 5-10. *1 illustrates the conditional return period characterized by the duration or temperature at a specific return period. For the conditional return period, under the first scenario (5-year), the mean return period for 221 stations is 4.15-years (Fig. 5-10. a1); the mean return period for the whole study area under the second scenario (10-year) is 8.66-years (Fig. 5-10. b1); that under the third scenario (20-year) is 17.66-years (Fig. 5-10. c1); and the mean return period for the whole study area under fourth scenario (50-year) is 45.08-years (Fig. 5-10. d1). Spatially, the Stanovoy Range in the west Lena river basin, the mountainous area upstream of the Yenisei and Ob river basins, and the mountainous area in the southeast Lena river basin, have lower than the basin-average return period under the all scenarios (Fig. 5-10. *1). This implies that these area are more likely to suffer from extreme dry spells with high temperature or long durations.

The mean joint return periods are much higher than the mean conditional return periods under the same scenarios, which are 25.43-years, 54.77-years, 84.06-years, and 117.28-years, respectively. Spatially, it seems that large areas in the southeastern parts of the study area have less than 10-year return period under the first scenarios while the Altay Mountains and the Stanovoy Range have lower than 5-year return periods (Fig. 5-10. a2). Under the second scenarios, the central Lena river basin, the Central Siberian Plateau within the Yenisei river basin, and the upstream region of the Ob river basin are expected to have lower than 10-year joint return periods (Fig. 5-10. b2). These areas are also expected to have dry spells of lower than 20-year return period under duration and temperature of joint 20-year return periods (Fig. 5-10. c2). For dry spells with both duration and temperature at 50-year return period, there are spots in the central Lena river basin, the upstream region of the Ob river basin, and the Central Siberian Plateau where the joint return periods are equal or less than 50 years (Fig. 5-10. d2).

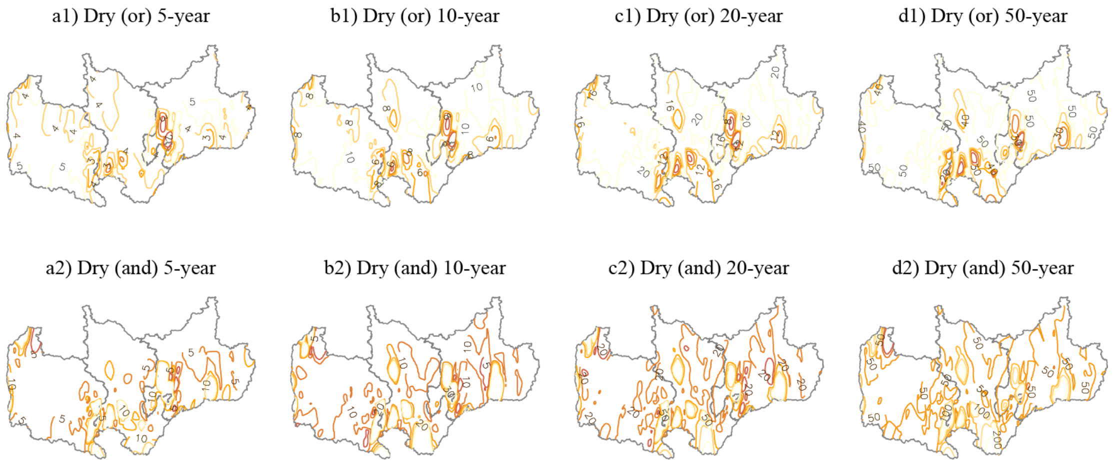
a1) Dry (or) 5-year b1) Dry (or) 10-year c1) Dry (or) 20-year d1) Dry (or) 50-year

a2) Dry (and) 5-year b2) Dry (and) 10-year c2) Dry (and) 20-year d2) Dry (and) 50-year

Figure 5-10. Spatial distribution of the conditional and joint return period of the duration and the temperature of dry spells at specific return period. a1, b1, c1, d1) conditional return period of when duration or temperature is at 5-years, 10-years, 20-years, and 50-years return period, respectively; a2, b2, c2, d2) joint return period of when duration and temperature is at 5-years, 10-years, 20-years, and 50-years return period, respectively.

For the wet spells, the mean conditional return periods under the first scenario is 3.17-year, while the spatial distribution shows that west of the Central Siberian Plateau to the Stanovoy Range has equal to or shorter than 3-year conditional return period for wet spells with duration or temperature at 5-year return periods (Fig. 5-11. a1). The mean conditional return periods under the second scenario is 6.27-year, even though most areas have equal to or less than 6-year return periods, especially in the Stanovoy Range (Fig. 5-11. b1). The conditional return periods of wet spells with duration or temperature at 20-year return period are distributed more evenly spatially than previous scenarios, with a mean conditional return period of 12.45-year (Fig. 5-11. c1). For the fourth scenario, the mean conditional return period is 31.03-year, but areas around Stanovoy Range have less than 30-year return period (Fig. 5-11. d1).

The mean joint return periods of the four scenarios are 13.58-year, 34.04-year, 83.33-year, and 259.95-year, respectively, which are much higher than the conditional return periods. Figure 5-11. a2 shows that for wet spells with duration and temperature jointly at 5-year return period, a large area in the north of study area have equal to or less than 10-year return periods, as well as a small area in the south mountainous area of Yenisei river basin. In the second scenario, the joint return period in the Stanovoy Range are much smaller than other regions (Fig. 5-11. b2). For the third scenario, the Altay Mountains within the Ob river basin have the lowest joint return periods (Fig. 5-11. c2). Under the highest return period, the Stanovoy Range has much smaller joint return periods than other regions (Fig. 5-11. d2), which means extreme wet spells are expected to occur more frequently in the Stanovoy Range than in other regions.

From the spatial distribution of conditional and joint return periods of extreme dry and wet spells, it seems that the likelihood of experiencing extreme dry or wet spells varies from location to location, but the Stanovoy Range is more likely to suffer from both extreme dry and extreme wet spells than other regions. The spatial distribution of the return periods also varies with scenarios, which indicates the non-linear relationship between the duration and temperature of spells. From the spatial distribution, the conditional return period of duration and temperature of wet spells have small values concentrating in the Stanovoy Range region in all scenarios.

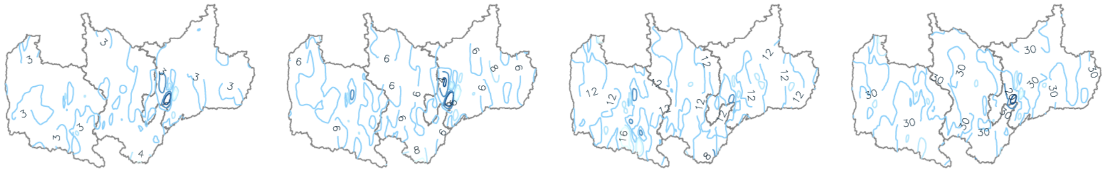

a1) Wet (or) 5-year b1) Wet (or) 10-year c1) Wet (or) 20-year d1) Wet (or) 50-year

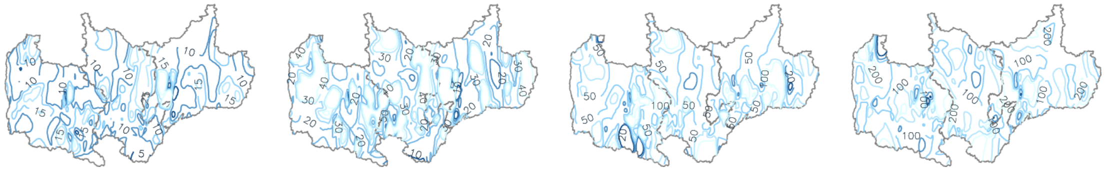

a2) Wet (and) 5-year b2) Wet (and) 10-year c2) Wet (and) 20-year d2) Wet (and) 50-year

Figure 5-11. Similar with Figure 5-10 but for wet spells.

5.5 Conclusions

In this study, the probabilistic characteristic of duration and temperature of dry and wet spells in Siberian river basins is investigated. Four continuous and two discrete probability distributions were fitted to the temperature and duration data of dry and wet spells occurring over three major river basins of Siberia. The results shows that the GEV Type-III distribution can model the probabilistic characteristic of temperature of both dry and wet spells well, while a two-parameter negative-binomial distribution fits the duration data of dry and wet spells better than the Poisson distribution. The spatial distributions of the marginal probability of duration and temperature show that north of the Altay Mountains upstream of the Ob river basin, the Central Siberian Plateau downstream of the Yenisei river basin, and the Dzhugdzhur Mountains in the southeast Lena river basin are more likely to have high temperature and long duration dry spells than other areas. The Stanovoy Range and the northwest Altay Mountain are more likely to have long duration and high temperature wet spells than other areas.

Based on the theoretical marginal distributions of duration and temperature, three types of Archimedean Copulas: Frank, Gumbel, and Clayton copulas functions are applied to develop the conditional and joint probabilities of these two variables of dry and wet spells. Among them, Gumbel and Clayton copulas develop better joint distributions of duration and temperature of dry and wet spells, respectively. From the fitted conditional and joint probability distributions at 5-year, 10-year, 20-year, and 50-year return periods, the respective resultant return periods estimated for dry and wet spells are plotted to show the spatial distributions of extreme dry and wet spells occurring over the study sites. Results show that the northwest Altay Mountains within the Ob river basin, the Stanovoy Range within the Lena river basin, and the Dzhugdzhur Mountains in the southeast Lena river basin are more likely to experience extreme dry and wet spells of long duration and high temperature than other regions.

Chapter 6. Conclusions and future work

6.1 Conclusions

Under the climate change, Arctic region, including the Arctic Ocean and the pan-Arctic area have been affected by the amplified warming, known as Arctic Amplification. Changes of Arctic sea ice has been concerned for decades, but the current understanding of the mechanism behind the changes is still unclear for prediction. Therefore, Chapter 1 of this thesis area devoted to the understanding of the changes of Arctic sea ice and its complex relationship with large-scale climate patterns and, hopefully, benefit the prediction of Arctic sea ice. For the pan-Arctic area, the hydrological process of these regions are of importance for the hydrological, oceanic, and atmospheric circulation of the entire Arctic region. However, researches about the hydrological processes of the pan-Arctic river basins are limited by the observations, especially Siberian area. Thus, Chapter 2, 3, and 4 of this thesis are devoted to the understanding of the hydrological changes of pan-Arctic river basins from the statistical and probabilistic characteristics and the prediction with the limited inputs. The following summaries provide better understanding of the sea ice changes and the hydrological changes over the Arctic region, which is essential for the analysis of the climate changes to Arctic regions where the warming has accelerated.

6.1.1 Variability of Arctic sea ice and teleconnection with climate patterns

From quantile regression analysis, the probabilistic analysis of Arctic sea ice was conducted with time and climate indices as covariates. The uneven declining magnitude of Arctic sea ice at different quantile levels were found at temporal scales that the sea ice have faster declining trend at the 5th and 95th percentiles than the 50th percentile, especially in most areas of the Beaufort Sea westward to the Kara Sea. Arctic sea ice of 5th quantiles is also found to have stronger teleconnections with climate patterns than the average. AO, NAO, PNA have more significant influence on Arctic sea ice than ENSO, PDO, and AMO.

From the projection of Arctic sea ice through a multivariate quantile regression model demonstrates that particular combined climate patterns have a stronger influence on Arctic sea ice than an individual climate pattern. Positive AO as well as positive NAO contribute to low winter sea ice, and a positive PNA contributes to low summer Arctic sea ice. In addition to these conditions, the sea ice decrease is amplified if there is concurrently positive AMO and PDO.

From the composite analysis of the climate variables (SLP, SST, GPH, UV), the anomalously strong anticyclonic circulation during the years of positive AO, NAO, and PNA were found to promotes more sea ice export through Fram Strait, resulting in excessive sea ice loss.

6.1.2 Non-stationarity of the streamflow of Siberia and teleconnection with climate patterns

Through applying the Mann-Kendall test, Pettitt test, and wavelet analysis, the non-stationarity were found to exist in the streamflow of three large Siberian river basins: the Ob, Yenisei, and Lena river basins. The streamflow of these Siberian river basins exhibit extensive increasing trends at multiple time-scales, except in the upstream of ORB and YRB, which suffer from the impacts of dam regulation, agricultural and industrial water use. From the regular and modified Mann-Kendall (MK) test, significant trend, auto-correlation and long-term persistence are determined in the streamflow time series of the Ob, Yenisei, and Lena river basins at annual, seasonal, and monthly timescales. Most stations are found to have abruptly changed during the 1970s to 1980s through the Pettitt test.

From a wavelet analysis, significant periodicities at annual, inter-annual, and interdecadal time scales were detected in the streamflow of the three northern Siberian river basins. From wavelet coherence analysis, the streamflow are found to have significant correlation with climate patterns, AO, NPO, PNA, and ENSO, at different time-scales, respectively, which could be the result of different forcing mechanisms.

Human activities, such as dam regulation and agricultural and industrial water use have limited influence on the seasonal streamflow changes, while the climate change and climate pattern have more responsibility for their non-stationary changes.

6.1.3 Simulation and prediction of streamflow from Pan-Arctic river basins under impact of climate change

From the calibrated Support Vector Regression Model (SVM) and Artificial Neural Network (ANN) model, the monthly streamflow of four great pan-Arctic river basins: Mackenzie river basin, Ob river basin, Lena river basin, and Yenisei river basin were simulated. Comparing with a statistical Multi-Variable Regression (MLR) model and the observation, SVM outperforms ANN and MLR in modeling the monthly streamflow of the four pan-Arctic river basins in both the calibration and validation stages. With precipitation, potential evapotranspiration, and temperature as predictors, the monthly streamflow of these four river basins subjected to climate changes based on RCP4.5 and RCP8.5 climate scenarios of four CMIP5 GCMs: ACCESS 1.0, CanESM2, HadESM2-ES, and MPI-ESM, for the 2050s and 2080s through the calibrated and validated SVM models. The monthly streamflow were projected to have increasing trend for all four river basins but with different magnitudes. These increasing trends were amplified by the increasing of air temperature and carbon emissions under RCP8.5 than under RCP4.5. As expected, under climate warming impacts attributed to rising greenhouse gas concentrations, the monthly streamflow of the four great pan-Arctic river basins are projected to increase significantly but with different increasing trends in different basins. In addition, the annual flow pattern is projected to change with the onset of spring snowmelt occurring earlier with higher peak flow at the expense of summer flows.

6.1.4 Probabilistic Characteristics of extreme wet and dry spells over Sibirian river basins

The dry and wet spells from daily temperature and precipitation of 221 stations within and around three Siberian river basins were extracted and their duration and temperature time series were fitted with univariate probability distribution. The results shows that GEV distribution can describe the probabilistic characteristic of temperature of both dry and wet spell, while two-parameter negative-binomial distribution outperforms the Poisson distribution on describing that of the duration. Then the copulas joint probability were applied to describe the joint probabilistic characteristics between the duration and temperature of dry and wet spells. Presented by conditional and joint return period, the regional likelihood of suffering from extreme dry and wet spells were investigated. Results show that the north Altay Mountain within Ob river basin, the Stanovoy Range within the Lena river, and Dzhugdzhur Mountains at the southeast of Lena river basin have higher likelihood of suffering from extreme dry and wet spell with long duration and high temperature than other places.

6.2 Future work

This thesis only provided limited analysis of Arctic sea ice and hydrological processes over the pan-Arctic river basins, and some qualitative discussions of physical mechanisms behind. Therefore, future works as a follow up to this thesis will be:

1) The spatial-temporal changes of precipitation over Siberian river basins and teleconnection with climate patterns

Since the non-stationarity of streamflow in the Siberian river basins has been found and has relationship with climate patterns, we expect that the precipitation to have non-stationarity and have relationship with climate patterns at both spatial and temporal scales. In addition to the evaluate the non-stationarity of precipitation over the Siberian river basins, future work should also estimate the teleconnection between the precipitation and climate patterns, such as PNA, ENSO, PDO. Moreover, in this thesis, the risk of suffering from extreme dry and wet spells has been found higher in some regions. The spatiotemporal quantile regression model will be used to detect the teleconnections of precipitations at extreme high or low quantiles with climate patterns.

2) Moisture transport patterns associated with Siberian heavy precipitation.

Recurrent large-scale atmospheric circulation patterns have been shown to be associated with variations in the intensity and location of polar jet stream, subtropical jet stream, or midlatitude storm tracks. In this research, significant statistical relationships have been detected between various climate indices and hydro-climatic variables over Siberian river basins, but causal mechanisms responsible for widespread precipitation and streamflow anomalies have not been comprehensively identified. Therefore, in future work, teleconnections between precipitation of Siberian river basins with large-scale atmospheric circulation patterns will be explored by identifying propagating patterns in atmospheric fields, e.g., jet stream–level wind speed, moisture flux, temperature advection, and vorticity advection, which have potential relevance to precipitation. Moisture sources and pathways that have contributed to the Siberian river basins extreme precipitation will be identified through moisture trajectory analysis.

3) Attribution of streamflow changes in Siberian river basin

Given the streamflow of Siberian have significant non-stationarity have been found in this thesis, the causes of this statistical changes have not been adequately concerned except the teleconnection with climate patterns. As there is quite low population in Siberian region, the influence of global warming on the land surface of the pan-Arctic regions, such as the permafrost, vegetation, and snow cover, is larger in magnitude and spatial-scales than human activities, which is essential to the hydrological cycling of river basins. Based on the long-term water balance of a river basin, Budyko curve describes the hydrological responses of a watershed to the climatic conditions with the respect to the characteristics of the watershed with the empirical parameter of the function representing the landscape properties that control water-energy balances. Therefore, the future work will use Budyko curve to evaluate the hydrological response of Siberian river basins to the climate changes.

Appendix

Appendix 1. Streamflow stations used in Chapter 3

	Point ID	Code	Latitude	Longitude	Drainage Area (km^2)	Hydro-zone	Altitude	Start Year	End Year
1	6076	9079	58.45	92.15	1400000	Yenisei	64.78	1936	1999
2	6145	3029	59.73	113.17	440000	Lena	166.2	1936	1999
3	6146	3036	60.48	120.7	770000	Lena	119.42	1933	1999
4	6147	3042	61.83	129.6	897000	Lena	85.08	1936	1999
5	6210	3157	60.17	116.8	27600	Lena	162.58	1934	1999
6	6214	3163	55.42	120.55	37300	Lena	494.72	1957	1999
7	6216	3169	59.37	121.32	115000	Lena	135.01	1936	1999
8	6224	3202	60.9	120.8	16600	Lena	139.68	1944	1999
9	6232	3219	58.97	126.27	49500	Lena	272.62	1936	1999
10	6234	3222	59.63	133.03	269000	Lena	152.55	1934	1999
11	6235	3225	61.87	135.5	514000	Lena	125.28	1926	1999
12	6236	3229	63.32	132.02	696000	Lena	74.1	1942	1999
13	6242	3248	58.65	127.05	43700	Lena	261.12	1952	1999
14	6245	3264	57.77	130.9	108000	Lena	230.35	1954	1999
15	6247	3271	59.78	134.75	165000	Lena	167.34	1935	1999
16	6250	3277	60.68	135.03	24200	Lena	45.46	1945	1999
17	6255	3291	59.67	127.05	23900	Lena	270.24	1933	1999
18	6256	3292	60.9	131.98	56800	Lena	134.35	1939	1999
19	6257	3293	62.22	134.13	65400	Lena	112.49	1937	1999
20	6265	3321	62.15	117.65	202000	Lena	109.35	1926	1999
21	6279	3366	64.23	116.91	78700	Lena	122.44	1954	1999
22	6342	3821	70.68	127.39	2430000	Lena	-1.41	1934	2000
23	6458	8084	58.38	97.45	866000	Yenisei	121.15	1936	1999
24	6459	8091	58.35	93.55	1040000	Yenisei	82.32	1953	1999
25	6495	8288	59.13	99.38	13300	Yenisei	172.95	1957	1999
26	6496	8289	58.1	99	9320	Yenisei	191.03	1957	1999
27	6498	8291	58.8	97.23	8950	Yenisei	151.12	1951	1999
28	6500	8296	57.82	94.32	127000	Yenisei	40.96	1936	1999
29	6537	9002	51.72	94.4	115000	Yenisei	615.5	1926	1999
30	6539	9022	53.02	91.48	182000	Yenisei	301.28	1911	1999
31	6541	9048	55.46	92.3	289000	Yenisei	NA	1955	1999
32	6543	9053	55.98	92.8	3.00E+05	Yenisei	134.41	1902	1999
33	6544	9092	61.6	90.08	1760000	Yenisei	19.84	1936	1999
34	6546	9112	52.47	96.1	15600	Yenisei	891.96	1958	1999
35	6547	9115	52.5	94.93	44600	Yenisei	789.31	1957	1999
36	6548	9116	51.88	94.46	56500	Yenisei	633.6	1956	1999
37	6553	9124	51.33	96.25	42300	Yenisei	45	1962	1999
38	6563	9166	52.08	92.73	6110	Yenisei	569.08	1951	1999

	Point ID	Code	Latitude	Longitude	Drainage Area (km^2)	Hydro-zone	Altitude	Start Year	End Year
39	6569	9207	52.65	90.1	14400	Yenisei	444.97	1932	1999
40	6570	9213	53.58	91.25	31300	Yenisei	264.97	1953	1999
41	6576	9252	53.8	92.87	31800	Yenisei	283.8	1911	1999
42	6594	9337	56.22	95.7	23000	Yenisei	197.98	1936	1999
43	6597	9342	55.7	95.73	11500	Yenisei	239.31	1955	1999
44	6606	9372	59.12	93.48	15100	Yenisei	144.89	1933	1999
45	6607	9374	58.8	92.83	19500	Yenisei	109.86	1960	1999
46	6615	9390	62.32	92.12	218000	Yenisei	42.51	1938	1999
47	6620	9401	62.48	86.28	16300	Yenisei	40.41	1960	1999
48	6622	9404	58.22	108.43	8270	Yenisei	329.72	1921	1999
49	6623	9406	61.27	108.02	77400	Yenisei	256.08	19511999	
50	6626	9415	65.63	90.02	447000	Yenisei	14.02	1938	1999
51	6628	9417	59.3	106.35	15000	Yenisei	344.22	1966	1999
52	6656	9803	67.43	86.48	2440000	Yenisei	0.03	1936	1999
53	6657	10002	52.45	84.92	98200	Ob	159.65	1953	2000
54	6658	10006	53.4	83.82	169000	Ob	127.89	1922	2000
55	6660	10011	54.8	82.95	232000	Ob	NA	1958	2000
56	6664	10021	58.3	82.88	486000	Ob	52.62	1936	2000
57	6666	10031	61.07	68.6	2690000	Ob	14.07	1936	1999
58	6668	10042	51.9	87.1	21000	Ob	43	1957	2000
59	6669	10044	52.27	87.17	25300	Ob	307.54	1962	2000
60	6670	10048	52.55	85.28	36900	Ob	162.68	1895	2000
61	6679	10062	51.28	87.72	16600	Ob	435.14	1930	2000
62	6684	10071	52.42	85.72	58400	Ob	197.08	1936	2000
63	6685	10073	50.27	85.62	5600	Ob	957.81	1945	2000
64	6701	10110	52.17	85.97	3360	Ob	40	1954	2000
65	6703	10112	52.28	85.42	1730	Ob	191.21	1960	2000
66	6705	10117	52.17	85.17	4720	Ob	181.65	1931	2000
67	6707	10120	51.65	84.32	2540	Ob	393.06	1955	2000
68	6708	10122	52.38	84.73	4870	Ob	44	1962	2000
69	6710	10126	51.02	84.32	3480	Ob	719.26	1936	2000
70	6711	10127	51.4	83.58	7180	Ob	47.2	1959	2000
71	6713	10132	52.1	82.55	17600	Ob	158.42	1964	2000
72	6715	10134	52.13	83.28	20700	Ob	145.04	1948	2000
73	6722	10150	51.18	81.2	6450	Ob	228.67	1955	2000
74	6723	10151	51.5	81.22	10300	Ob	207.33	1955	2000
75	6724	10153	52.52	82.77	18700	Ob	150.34	1954	2000
76	6728	10175	53.47	85.42	11000	Ob	34	1964	2000
77	6729	10176	53.73	84.95	15900	Ob	160.33	1937	1999
78	6730	10177	53.8	83.57	20600	Ob	132.35	1943	2000
79	6743	10205	54.63	83.4	6270	Ob	116.5	1956	2000

	Point ID	Code	Latitude	Longitude	Drainage Area (km^2)	Hydro-zone	Altitude	Start Year	End Year
80	6749	10216	54.95	85.67	7960	Ob	149.2	1960	2000
81	6751	10219	55.32	84.1	15700	Ob	119.17	1942	2000
82	6752	10220	55	83.33	17300	Ob	100.01	1959	2000
83	6757	10232	53.43	89.13	2480	Ob	437.97	1958	2000
84	6758	10233	53.63	88.53	4350	Ob	292.7	1966	2000
85	6760	10240	53.78	87.15	29800	Ob	192.46	1894	2000
86	6762	10251	56.5	84.92	57000	Ob	69.25	1918	2000
87	6764	10259	53.68	88.08	3320	Ob	240.04	1937	2000
88	6767	10266	53.7	87.8	8790	Ob	222.68	1955	2000
89	6770	10276	52.82	87.25	2510	Ob	314.51	1957	2000
90	6771	10277	53.33	87.23	7080	Ob	225.2	1936	2000
91	6772	10279	53.58	87.3	1060	Ob	242.63	1936	2000
92	6775	10287	54.03	87.17	1110	Ob	194.11	1953	2000
93	6778	10292	54.83	87.53	1330	Ob	178.85	1941	2000
94	6786	10308	56.55	83.62	8190	Ob	89.1	1953	2000
95	6788	10315	55.03	89.87	9990	Ob	368.09	1961	2000
96	6789	10317	55.38	91.62	14700	Ob	293.08	1939	2000
97	6790	10323	56.17	89.93	33800	Ob	196.26	1951	2000
98	6791	10328	57.33	88.1	55300	Ob	123.48	1936	2000
99	6792	10329	56.85	86.62	92500	Ob	97.19	1936	2000
100	6794	10331	57.78	85.15	131000	Ob	71.19	1936	2000
101	6795	10332	54.4	89.45	3520	Ob	498.59	1952	2000
102	6796	10338	54.87	89.3	3100	Ob	449.74	1959	2000
103	6799	10343	55.82	90.15	4580	Ob	250.66	1956	2000
104	6809	10379	56.65	90.55	2130	Ob	180.25	1946	2000
105	6816	10387	56.2	87.78	9820	Ob	119.63	1936	2000
106	6824	10402	57.05	88.08	11500	Ob	118.75	1961	2000
107	6835	10423	57.57	85.42	2620	Ob	44.5	1959	2000
108	6840	10432	57.48	82.22	6610	Ob	68.38	1959	2000
109	6845	10441	57.08	81.67	2330	Ob	92.03	1951	2000
110	6846	10444	56.85	83.07	2560	Ob	98.98	1936	2000
111	6847	10445	57.53	82.92	5210	Ob	70.54	1965	2000
112	6849	10453	58.65	86.82	38400	Ob	84.44	1937	2000
113	6850	10455	58.42	83.67	71500	Ob	57.6	1955	2000
114	6851	10460	58.77	86.07	8740	Ob	83.76	1956	2000
115	6854	10466	59.37	82.83	6500	Ob	72.81	1955	2000
116	6855	10468	58.17	80.6	17900	Ob	58.41	1957	2000
117	6857	10473	57.83	80.15	7090	Ob	41.96	1956	2000
118	6858	10475	57.78	77.28	3730	Ob	82.41	1955	2000
119	6859	10476	58.55	76.47	19000	Ob	62.7	1960	2000
120	6860	10478	59.22	78.22	31700	Ob	52.64	1936	2000

	Point ID	Code	Latitude	Longitude	Drainage Area (km^2)	Hydro-zone	Altitude	Start Year	End Year
121	6865	10488	60.35	84.08	10100	Ob	91.04	1954	2000
122	6866	10489	59.85	81.95	24500	Ob	60.58	1937	2000
123	6883	10511	61.45	68.93	11500	Ob	20.64	1968	1999
124	6894	10548	55.23	80.32	3910	Ob	123.34	1948	2000
125	6895	10549	54.7	78.67	6440	Ob	103.94	1936	2000
126	6950	11048	55.02	73.3	769000	Ob	68.94	1936	1999
127	6952	11056	58.2	68.23	1500000	Ob	35.62	1891	1999
128	7009	11309	55.45	78.32	12200	Ob	104.23	1936	2000
129	7010	11312	55.6	76.38	39200	Ob	92.31	1955	2000
130	7011	11313	55.07	74.58	47800	Ob	76.98	1936	1999
131	7020	11335	56.35	78.35	5480	Ob	113.5	1948	2000
132	7022	11337	55.67	76.75	16200	Ob	94.85	1939	2000
133	7027	11350	56.6377.5	6250	Ob	88.05	1954	2000	
134	7029	11352	56.47	76.02	14200	Ob	69.41	1948	2000
135	7030	11353	56.38	75.25	16400	Ob	61.13	1936	1999
136	7032	11357	56.63	77.52	1430	Ob	88.52	1948	2000
137	7033	11358	55.48	77.82	2740	Ob	97.7	1948	2000
138	7036	11369	56.95	75.32	4460	Ob	74.02	1950	1999
139	7037	11370	57.07	74.52	6650	Ob	54.6	1954	1999
140	7040	11379	56.98	72.63	4070	Ob	70.42	1960	1999
141	7041	11381	57.1	73.07	4580	Ob	62.56	1958	1999
142	7044	11385	57.35	74.75	2320	Ob	80.29	1945	1999
143	7057	1141256.1	69.47	140000	Ob	69.54	1955	1999	
144	7058	11414	56.82	70.63	151000	Ob	54.32	1952	1999
145	7059	11415	57.45	70.85	158000	Ob	42.48	1963	1999
146	7080	11491	57.67	69.2	15600	Ob	38.73	1961	1999
147	7081	11493	56.43	68.58	2540	Ob	82.95	1958	1999
1487083	11496	57.13	69.22	2140	Ob	57.7	1952	1999	
149	7085	11499	57.53	68.68	2080	Ob	52.48	1954	1999
150	7086	11502	58.4	67.47	6780	Ob	44	1964	1999
151	7094	11526	60.33	69	68600	Ob	19.63	1962	1999
152	7100	11538	62.43	60.88	9850	Ob	32.77	1954	1999
153	7103	11542	63.65	62.1	65200	Ob	12.04	1937	1999
154	7105	11545	63.18	64.4	87800	Ob	7.43	1958	1999
155	7112	11558	66.03	68.73	15100	Ob	5.67	1953	1999
156	7142	11801	66.63	66.6	2950000	Ob	0.44	1930	1999
157	7154	12018	56.67	66.35	241000	Ob	49.3	1936	1999
158	7174	12098	56.17	66.47	3250	Ob	66.7	1963	1999
159	7185	12129	56.48	65.35	56000	Ob	57.98	1937	1999
160	7228	12383	56.95	65.83	18600	Ob	50.52	1895	1999

Appendix 1. Weather Stations used in Chapter 5 and the simulation errors of each copulas function

	No.	Latitude (N)	Longitude (E)	Year	Dry spells						Wet spells					
					Clayton		Frank		Gumbel-Hougaard		Clayton		Frank		Gumbel-Hougaard	
					τ	RMSE	τ	RMSE	τ	RMSE	τ	RMSE	τ	RMSE	τ	RMSE
1	20982	70.97	94.5	1933	0.32	0.11	1.27	0.11	1.16	0.09	-0.24	0.12	-1.22	0.12	1.00	0.11
2	21824	71.58	128.92	1932	0.09	0.10	0.39	0.10	1.04	0.10	-0.02	0.12	-0.10	0.12	1.00	0.12
3	21921	70.68	127.4	1940	0.18	0.10	0.74	0.10	1.09	0.09	-0.17	0.13	-0.83	0.14	1.00	0.12
4	23032	69.72	66.8	1940	0.33	0.07	1.29	0.07	1.16	0.07	-0.12	0.13	-0.59	0.13	1.00	0.12
5	23074	69.4	86.17	1906	0.37	0.08	1.45	0.08	1.19	0.07	-0.18	0.15	-0.90	0.15	1.00	0.14
6	23146	68.47	73.58	1950	0.29	0.13	1.16	0.13	1.15	0.13	0.03	0.17	0.13	0.17	1.01	0.17
7	23220	67.05	64.07	1959	0.25	0.17	0.99	0.17	1.12	0.15	-0.27	0.12	-1.46	0.13	1.00	0.11
8	23242	67.68	72.88	1961	0.31	0.08	1.22	0.08	1.15	0.08	-0.11	0.14	-0.53	0.14	1.00	0.13
9	23274	67.47	86.57	1929	0.40	0.25	1.53	0.25	1.20	0.25	-0.18	0.16	-0.89	0.16	1.00	0.15
10	23324	66.43	60.77	1940	0.28	0.14	1.13	0.14	1.14	0.12	-0.29	0.14	-1.58	0.15	1.00	0.12
11	23330	66.53	66.68	1882	0.19	0.08	0.78	0.08	1.09	0.08	-0.09	0.24	-0.42	0.24	1.00	0.23
12	23331	66.9	65.67	1940	0.27	0.18	1.08	0.18	1.13	0.17	-0.18	0.14	-0.89	0.14	1.00	0.13
13	23345	66.63	72.93	1948	0.30	0.11	1.19	0.11	1.15	0.10	-0.17	0.15	-0.82	0.15	1.00	0.14
14	23383	66.88	93.47	1939	0.32	0.52	1.27	0.52	1.16	0.51	-0.15	0.13	-0.72	0.13	1.00	0.12
15	23412	65.97	56.92	1940	0.35	0.41	1.35	0.41	1.17	0.41	-0.29	0.14	-1.59	0.14	1.00	0.12
16	23418	65.12	57.1	1951	0.26	0.13	1.06	0.13	1.13	0.12	-0.30	0.13	-1.66	0.13	1.00	0.11
17	23445	65.47	72.67	1959	0.49	0.10	1.82	0.10	1.24	0.09	-0.20	0.28	-1.02	0.28	1.00	0.27
18	23463	65.98	84.27	1959	0.37	0.44	1.43	0.45	1.18	0.44	-0.22	0.13	-1.13	0.13	1.00	0.12
19	23472	65.78	87.93	1843	0.40	0.23	1.53	0.23	1.20	0.22	-0.24	0.34	-1.24	0.34	1.00	0.33
20	23527	64.28	60.88	1940	0.11	0.32	0.46	0.32	1.05	0.32	-0.15	0.12	-0.73	0.12	1.00	0.11
21	23589	64.2	93.78	1959	0.32	0.11	1.27	0.12	1.16	0.10	-0.21	0.13	-1.06	0.13	1.00	0.12
22	23631	63.93	65.05	1834	0.33	0.18	1.30	0.18	1.17	0.17	-0.21	0.27	-1.08	0.27	1.00	0.26
23	23656	63.38	78.32	1958	0.42	0.14	1.61	0.14	1.21	0.12	-0.26	0.17	-1.39	0.17	1.00	0.15
24	23662	63.98	82.08	1947	0.46	0.31	1.74	0.31	1.23	0.30	-0.27	0.20	-1.44	0.20	1.00	0.17

					Dry spells						Wet spells					
	No.	Latitude (N)	Longitude (E)	Year	Clayton		Frank		Gumbel-Hougaard		Clayton		Frank		Gumbel-Hougaard	
					τ	RMSE	τ	RMSE	τ	RMSE	τ	RMSE	τ	RMSE	τ	RMSE
25	23678	63.15	87.95	1911	0.51	0.10	1.88	0.10	1.25	0.09	-0.26	0.15	-1.34	0.16	1.00	0.14
26	23711	62.7	56.2	1888	0.26	0.21	1.05	0.22	1.13	0.21	-0.20	0.25	-1.02	0.25	1.00	0.24
27	23724	62.43	60.87	1933	0.25	0.12	0.99	0.12	1.12	0.11	-0.25	0.14	-1.28	0.15	1.00	0.13
28	23734	62.45	66.05	1904	0.43	0.10	1.64	0.11	1.22	0.09	-0.21	0.45	-1.08	0.45	1.00	0.44
29	23849	61.25	73.5	1884	0.56	0.36	2.05	0.36	1.28	0.36	-0.26	0.29	-1.38	0.29	1.00	0.28
30	23867	61.1	80.25	1937	0.52	0.11	1.94	0.11	1.26	0.10	-0.24	0.52	-1.26	0.52	1.00	0.52
31	23884	61.6	90.02	1934	0.38	0.08	1.48	0.08	1.19	0.07	-0.16	0.30	-0.79	0.30	1.00	0.30
32	23891	61.67	96.37	1934	0.44	0.45	1.66	0.45	1.22	0.44	-0.33	0.18	-1.84	0.18	1.00	0.15
33	23914	60.4	56.52	1888	0.34	0.23	1.32	0.23	1.17	0.22	-0.21	0.17	-1.10	0.17	1.00	0.15
34	23921	60.68	60.45	1934	0.43	0.19	1.64	0.19	1.22	0.18	-0.28	0.26	-1.53	0.26	1.00	0.25
35	23933	61.02	69.12	1897	0.47	0.32	1.78	0.32	1.24	0.31	-0.24	0.24	-1.23	0.24	1.00	0.23
36	23946	60.5	74.02	1944	0.52	0.55	1.93	0.55	1.26	0.55	-0.30	0.33	-1.65	0.33	1.00	0.32
37	23955	60.43	77.87	1932	0.36	0.12	1.40	0.12	1.18	0.10	-0.28	0.25	-1.50	0.25	1.00	0.24
38	23966	60.35	84.08	1955	0.75	0.30	2.61	0.30	1.37	0.28	-0.40	0.12	-2.37	0.13	1.00	0.11
39	23986	60.38	93.03	1941	0.32	0.37	1.25	0.37	1.16	0.37	-0.16	0.13	-0.78	0.14	1.00	0.13
40	24105	68.47	102.37	1937	0.41	0.08	1.58	0.08	1.21	0.08	-0.26	0.16	-1.39	0.17	1.00	0.15
41	24125	68.5	112.43	1935	0.30	0.25	1.18	0.25	1.15	0.25	-0.23	0.15	-1.16	0.16	1.00	0.14
42	24136	68.62	118.33	1938	0.25	0.08	1.02	0.08	1.13	0.08	-0.15	0.32	-0.72	0.32	1.00	0.31
43	24143	68.73	124	1936	0.20	0.13	0.81	0.13	1.10	0.12	-0.19	0.28	-0.94	0.28	1.00	0.28
44	24266	67.57	133.4	1869	0.25	0.37	1.03	0.37	1.13	0.37	-0.17	0.35	-0.86	0.35	1.00	0.35
45	24329	66.25	114.28	1940	0.31	0.10	1.24	0.10	1.16	0.09	-0.12	0.34	-0.59	0.34	1.00	0.33
46	24343	66.77	123.4	1935	0.23	0.49	0.93	0.49	1.11	0.49	-0.21	0.16	-1.07	0.17	1.00	0.15
47	24371	66.8	136.68	1942	0.40	0.09	1.52	0.09	1.20	0.08	-0.20	0.42	-1.02	0.42	1.00	0.41
48	24507	64.27	100.23	1928	0.32	0.11	1.25	0.11	1.16	0.11	-0.21	0.16	-1.09	0.16	1.00	0.14
49	24538	64.23	116.92	1955	0.38	0.24	1.47	0.24	1.19	0.23	-0.14	0.22	-0.69	0.22	1.00	0.21
50	24606	63.58	103.97	1951	0.44	0.20	1.68	0.20	1.22	0.20	-0.18	0.16	-0.90	0.16	1.00	0.15
51	24641	63.78	121.62	1863	0.45	0.14	1.69	0.14	1.22	0.14	-0.16	0.14	-0.77	0.14	1.00	0.13

	No.	Latitude (N)	Longitude (E)	Year	Dry spells						Wet spells					
					Clayton		Frank		Gumbel-Hougaard		Clayton		Frank		Gumbel-Hougaard	
					τ	RMSE	τ	RMSE	τ	RMSE	τ	RMSE	τ	RMSE	τ	RMSE
52	24643	63.95	124.83	1957	0.39	0.36	1.50	0.36	1.20	0.36	-0.22	0.14	-1.14	0.14	1.00	0.12
53	24661	64	130.3	1940	0.35	0.32	1.35	0.32	1.17	0.31	-0.15	0.55	-0.76	0.55	1.00	0.55
54	24671	63.95	135.87	1937	0.40	0.15	1.55	0.15	1.20	0.14	-0.14	0.13	-0.70	0.13	1.00	0.12
55	24679	63.22	139.6	1942	0.30	0.23	1.20	0.23	1.15	0.23	-0.20	0.43	-1.01	0.43	1.00	0.42
56	24688	63.25	143.15	1930	0.31	0.23	1.23	0.23	1.16	0.23	-0.24	0.17	-1.26	0.17	1.00	0.15
57	24713	62.88	108.43	1961	0.57	0.24	2.09	0.24	1.29	0.24	-0.28	0.45	-1.48	0.45	1.00	0.44
58	24726	62.53	113.87	1959	0.41	0.20	1.55	0.20	1.20	0.20	-0.14	0.19	-0.68	0.20	1.00	0.19
59	24738	62.15	117.65	1900	0.60	0.33	2.16	0.33	1.30	0.33	-0.20	0.25	-1.03	0.25	1.00	0.24
60	24763	62.82	134.43	1961	0.42	0.09	1.59	0.09	1.21	0.08	-0.16	0.27	-0.81	0.27	1.00	0.26
61	24802	61.75	102.8	1940	0.36	0.19	1.41	0.19	1.18	0.19	-0.21	0.16	-1.05	0.17	1.00	0.15
62	24817	61.27	108.02	1936	0.42	0.09	1.59	0.09	1.21	0.08	-0.25	0.30	-1.31	0.31	1.00	0.29
63	24908	60.33	102.27	1932	0.38	0.18	1.48	0.18	1.19	0.18	-0.22	0.23	-1.15	0.23	1.00	0.22
64	24923	60.72	114.88	1940	0.36	0.22	1.40	0.22	1.18	0.22	-0.27	0.40	-1.44	0.40	1.00	0.39
65	24933	60.95	119.3	1959	0.58	0.27	2.10	0.27	1.29	0.27	-0.25	0.31	-1.30	0.31	1.00	0.30
66	24944	60.4	120.42	1882	0.38	0.09	1.48	0.09	1.19	0.09	-0.23	0.39	-1.16	0.39	1.00	0.38
67	24951	60.82	125.32	1940	0.47	0.14	1.77	0.14	1.24	0.14	-0.17	0.28	-0.85	0.28	1.00	0.28
68	24959	62.02	129.72	1834	0.36	0.22	1.39	0.22	1.18	0.22	-0.27	0.16	-1.43	0.16	1.00	0.14
69	24966	60.38	134.45	1893	0.30	0.31	1.18	0.31	1.15	0.31	-0.13	0.28	-0.63	0.28	1.00	0.28
70	24967	60.47	130	1942	0.46	0.11	1.74	0.11	1.23	0.10	-0.19	0.18	-0.97	0.18	1.00	0.16
71	24982	60.72	142.78	1960	0.55	0.23	2.00	0.23	1.27	0.23	-0.26	0.18	-1.35	0.18	1.00	0.16
72	28064	59.62	65.72	1927	0.40	0.31	1.54	0.31	1.20	0.29	-0.29	0.43	-1.54	0.43	1.00	0.43
73	28138	58.52	58.85	1888	0.42	0.24	1.60	0.24	1.21	0.22	-0.30	0.24	-1.64	0.24	1.00	0.22
74	28144	58.87	60.78	1890	0.53	0.10	1.96	0.10	1.27	0.09	-0.26	0.40	-1.37	0.40	1.00	0.40
75	28255	58.05	63.68	1940	0.53	0.20	1.96	0.20	1.27	0.19	-0.32	0.16	-1.78	0.16	1.00	0.14
76	28275	58.15	68.25	1884	0.47	0.40	1.75	0.40	1.23	0.40	-0.30	0.29	-1.63	0.29	1.00	0.28
77	28367	57.12	65.43	1950	0.42	0.24	1.59	0.24	1.21	0.22	-0.32	0.25	-1.74	0.25	1.00	0.24
78	28434	56.65	57.78	1926	0.50	0.13	1.86	0.13	1.25	0.11	-0.32	0.35	-1.79	0.35	1.00	0.34

	No.	Latitude (N)	Longitude (E)	Year	Dry spells						Wet spells					
					Clayton		Frank		Gumbel-Hougaard		Clayton		Frank		Gumbel-Hougaard	
					τ	RMSE	τ	RMSE	τ	RMSE	τ	RMSE	τ	RMSE	τ	RMSE
79	28440	56.83	60.63	1831	0.54	0.29	1.99	0.29	1.27	0.28	-0.30	0.15	-1.61	0.16	1.00	0.13
80	28445	56.73	61.07	1959	0.57	0.36	2.09	0.36	1.29	0.35	-0.27	0.35	-1.42	0.35	1.00	0.34
81	28493	56.9	74.38	1887	0.51	0.41	1.90	0.41	1.26	0.40	-0.35	0.31	-2.02	0.31	1.00	0.29
82	28537	55.7	57.9	1940	0.49	0.10	1.83	0.10	1.24	0.09	-0.28	0.34	-1.51	0.34	1.00	0.33
83	28552	56.07	63.65	1894	0.54	0.66	1.99	0.66	1.27	0.66	-0.27	0.54	-1.42	0.54	1.00	0.54
84	28561	56.02	65.7	1959	0.54	0.30	1.97	0.30	1.27	0.29	-0.27	0.42	-1.41	0.42	1.00	0.42
85	28573	56.1	69.43	1925	0.44	0.42	1.67	0.42	1.22	0.41	-0.39	0.27	-2.32	0.27	1.00	0.26
86	28630	55.17	59.67	1936	0.67	0.10	2.39	0.10	1.34	0.09	-0.25	0.79	-1.33	0.79	1.00	0.78
87	28661	55.47	65.4	1893	0.55	0.32	2.00	0.32	1.27	0.32	-0.25	0.23	-1.31	0.23	1.00	0.22
88	28666	55.25	67.3	1961	0.59	0.11	2.15	0.11	1.30	0.10	-0.29	0.31	-1.60	0.31	1.00	0.30
89	28679	54.83	69.15	1890	0.54	0.40	1.99	0.40	1.27	0.40	-0.22	0.47	-1.12	0.47	1.00	0.47
90	28698	55.02	73.38	1875	0.47	0.17	1.77	0.17	1.24	0.17	-0.27	0.42	-1.43	0.42	1.00	0.41
91	28748	54.08	61.62	1940	0.39	0.54	1.51	0.54	1.20	0.54	-0.22	0.35	-1.12	0.36	1.00	0.35
92	28833	53.88	59.2	1903	0.56	0.14	2.05	0.14	1.28	0.14	-0.24	0.34	-1.23	0.34	1.00	0.34
93	28895	53.78	73.88	1959	0.59	0.12	2.14	0.12	1.30	0.10	-0.27	0.18	-1.43	0.18	1.00	0.16
94	28952	53.22	63.62	1902	0.48	0.28	1.79	0.28	1.24	0.27	-0.30	0.32	-1.61	0.32	1.00	0.31
95	29023	59.85	81.95	1940	0.60	0.33	2.17	0.33	1.30	0.33	-0.26	0.48	-1.35	0.48	1.00	0.48
96	29111	59.22	78.23	1940	0.42	0.11	1.62	0.11	1.21	0.09	-0.27	0.92	-1.42	0.92	1.00	0.92
97	29154	58.88	87.75	1940	0.43	0.30	1.64	0.30	1.22	0.29	-0.29	0.55	-1.59	0.55	1.00	0.54
98	29231	58.3	82.88	1925	0.37	0.24	1.43	0.24	1.18	0.24	-0.31	0.25	-1.67	0.25	1.00	0.24
99	29263	58.45	92.15	1853	0.53	0.29	1.96	0.29	1.27	0.29	-0.24	0.25	-1.27	0.25	1.00	0.24
100	29282	58.38	97.45	1930	0.34	0.23	1.33	0.23	1.17	0.22	-0.27	0.37	-1.44	0.37	1.00	0.37
101	29313	57.57	79.43	1927	0.42	0.29	1.61	0.29	1.21	0.29	-0.26	0.26	-1.38	0.26	1.00	0.25
102	29328	57	82.07	1934	0.35	0.10	1.38	0.10	1.18	0.10	-0.25	0.29	-1.30	0.29	1.00	0.28
103	29348	57.07	86.22	1940	0.29	0.34	1.17	0.34	1.15	0.34	-0.29	0.22	-1.56	0.22	1.00	0.21
104	29379	57.2	94.55	1988	0.46	0.34	1.74	0.34	1.23	0.34	-0.20	0.62	-0.99	0.62	1.00	0.62
105	29393	57.65	99.53	1959	0.54	0.23	1.98	0.23	1.27	0.22	-0.29	0.42	-1.54	0.42	1.00	0.41

	No.	Latitude (N)	Longitude (E)	Year	Dry spells						Wet spells					
					Clayton		Frank		Gumbel-Hougaard		Clayton		Frank		Gumbel-Hougaard	
					τ	RMSE	τ	RMSE	τ	RMSE	τ	RMSE	τ	RMSE	τ	RMSE
106	29418	56.33	78.37	1940	0.54	0.30	1.99	0.30	1.27	0.29	-0.30	0.38	-1.62	0.38	1.00	0.37
107	29430	56.5	84.92	1837	0.46	0.11	1.74	0.11	1.23	0.10	-0.24	0.41	-1.27	0.41	1.00	0.41
108	29467	56.28	90.52	1940	0.46	0.24	1.72	0.24	1.23	0.23	-0.31	0.36	-1.70	0.36	1.00	0.35
109	29539	55.67	84.4	1940	0.30	0.42	1.20	0.42	1.15	0.42	-0.22	0.24	-1.13	0.24	1.00	0.23
110	29541	56.07	85.62	1940	0.38	0.35	1.48	0.35	1.19	0.34	-0.26	0.46	-1.38	0.46	1.00	0.45
111	29557	55.75	88.3	1940	0.50	0.14	1.85	0.15	1.25	0.12	-0.33	0.32	-1.81	0.32	1.00	0.31
112	29570	56.03	92.75	1914	0.35	0.45	1.38	0.45	1.18	0.45	-0.28	0.30	-1.51	0.30	1.00	0.29
113	29580	56.17	95.27	1940	0.51	0.34	1.90	0.34	1.26	0.34	-0.24	0.38	-1.26	0.38	1.00	0.37
114	29594	55.95	98	1940	0.46	0.10	1.74	0.10	1.23	0.09	-0.20	0.31	-1.00	0.31	1.00	0.30
115	29605	55.22	75.97	1940	0.38	0.53	1.48	0.53	1.19	0.52	-0.26	0.40	-1.39	0.40	1.00	0.40
116	29612	55.33	78.37	1900	0.40	0.39	1.53	0.39	1.20	0.38	-0.25	0.16	-1.29	0.17	1.00	0.14
117	29638	54.9	82.95	1930	0.29	0.60	1.15	0.60	1.14	0.60	-0.23	0.39	-1.17	0.39	1.00	0.38
118	29645	55.25	86.22	1955	0.37	0.40	1.44	0.40	1.19	0.40	-0.15	0.21	-0.76	0.22	1.00	0.21
119	29664	55.1	90.83	1958	0.46	0.20	1.73	0.21	1.23	0.19	-0.28	0.35	-1.52	0.35	1.00	0.34
120	29698	54.88	99.03	1941	0.13	0.32	0.54	0.32	1.06	0.32	-0.10	0.47	-0.48	0.47	1.00	0.47
121	29752	54.75	88.82	1932	0.62	0.25	2.22	0.25	1.31	0.25	-0.21	0.35	-1.06	0.35	1.00	0.35
122	29789	54.22	96.97	1935	0.39	0.36	1.50	0.36	1.19	0.35	-0.20	0.33	-1.01	0.33	1.00	0.32
123	29807	53.35	75.45	1936	0.37	0.10	1.43	0.10	1.18	0.09	-0.23	0.23	-1.18	0.24	1.00	0.23
124	29822	53.82	81.27	1940	0.35	0.41	1.37	0.41	1.18	0.41	-0.29	0.47	-1.53	0.47	1.00	0.47
125	29838	53.43	83.52	1838	0.26	0.37	1.04	0.37	1.13	0.36	-0.23	0.38	-1.16	0.38	1.00	0.38
126	29849	53.33	87.18	1955	0.34	0.49	1.34	0.49	1.17	0.49	-0.26	0.46	-1.39	0.46	1.00	0.46
127	29858	53.28	89.07	1947	0.38	0.35	1.45	0.35	1.19	0.34	-0.28	0.36	-1.51	0.36	1.00	0.35
128	29862	53.77	91.32	1959	0.45	0.38	1.69	0.38	1.22	0.38	-0.18	0.17	-0.89	0.17	1.00	0.16
129	29866	53.72	91.7	1885	0.47	0.29	1.77	0.29	1.24	0.29	-0.19	0.24	-0.93	0.24	1.00	0.23
130	29915	52.97	78.65	1940	0.36	0.29	1.41	0.29	1.18	0.28	-0.27	0.34	-1.40	0.34	1.00	0.33
131	29923	53.08	82.33	1955	0.39	0.32	1.50	0.33	1.19	0.31	-0.21	0.16	-1.04	0.17	1.00	0.15
132	29939	52.68	84.93	1940	0.02	0.11	0.07	0.11	1.01	0.11	-0.02	0.47	-0.10	0.47	1.00	0.47

					Dry spells						Wet spells					
	No.	Latitude (N)	Longitude (E)	Year	Clayton		Frank		Gumbel-Hougaard		Clayton		Frank		Gumbel-Hougaard	
					τ	RMSE	τ	RMSE	τ	RMSE	τ	RMSE	τ	RMSE	τ	RMSE
133	29974	52.8	93.23	1926	0.34	0.09	1.33	0.09	1.17	0.08	-0.19	0.31	-0.94	0.31	1.00	0.30
134	29998	52.5	99.82	1934	0.30	0.57	1.21	0.57	1.15	0.57	-0.25	0.27	-1.31	0.27	1.00	0.27
135	30028	59.28	106.17	1944	0.18	0.21	0.75	0.21	1.09	0.20	-0.13	0.29	-0.61	0.29	1.00	0.29
136	30054	59.45	112.58	1929	0.32	0.08	1.25	0.08	1.16	0.08	-0.19	0.27	-0.95	0.27	1.00	0.26
137	30069	59	116.92	1941	0.70	0.12	2.48	0.12	1.35	0.10	-0.22	0.39	-1.11	0.39	1.00	0.39
138	30089	59.02	121.77	1940	0.23	0.10	0.94	0.10	1.12	0.09	-0.19	0.29	-0.93	0.29	1.00	0.28
139	30209	57.03	102.3	1961	0.49	0.35	1.84	0.35	1.25	0.34	-0.16	0.30	-0.81	0.30	1.00	0.29
140	30219	57.1	104.97	1940	0.28	0.29	1.12	0.29	1.14	0.28	-0.21	0.48	-1.05	0.48	1.00	0.48
141	30230	57.77	108.07	1892	0.39	0.23	1.49	0.23	1.19	0.23	-0.19	0.47	-0.97	0.47	1.00	0.47
142	30252	57.82	114.17	1959	0.41	0.22	1.57	0.22	1.21	0.21	-0.24	0.19	-1.26	0.19	1.00	0.17
143	30253	57.85	114.23	1931	0.29	0.09	1.16	0.09	1.15	0.09	-0.12	0.28	-0.58	0.28	1.00	0.28
144	30309	56.28	101.75	1901	0.31	0.31	1.21	0.31	1.15	0.31	-0.18	0.34	-0.91	0.34	1.00	0.34
145	30328	56.05	105.83	1932	0.26	0.35	1.03	0.35	1.13	0.35	-0.19	0.37	-0.96	0.37	1.00	0.36
146	30337	56.28	107.62	1959	0.16	0.55	0.67	0.55	1.08	0.55	-0.14	0.28	-0.69	0.28	1.00	0.28
147	30356	56.38	114.83	1964	0.40	0.30	1.55	0.30	1.20	0.29	-0.13	0.33	-0.61	0.33	1.00	0.33
148	30372	56.9	118.27	1938	0.43	0.20	1.62	0.20	1.21	0.18	-0.26	0.17	-1.40	0.17	1.00	0.15
149	30385	56.58	121.48	1940	0.30	0.19	1.18	0.19	1.15	0.19	-0.15	0.31	-0.73	0.31	1.00	0.31
150	30393	56.83	124.87	1927	0.22	0.17	0.90	0.17	1.11	0.15	-0.21	0.23	-1.07	0.23	1.00	0.22
151	30433	55.78	109.55	1933	0.15	0.41	0.62	0.41	1.07	0.41	0.02	0.43	0.11	0.43	1.01	0.43
152	30437	55.15	107.62	1943	-0.01	0.29	-0.06	0.29	1.00	0.29	0.06	0.13	0.27	0.13	1.03	0.13
153	30469	55.12	116.77	1935	0.26	0.36	1.04	0.36	1.13	0.36	-0.14	0.15	-0.69	0.15	1.00	0.14
154	30471	55.87	117.37	1940	0.17	0.15	0.71	0.15	1.09	0.14	-0.17	0.14	-0.83	0.15	1.00	0.13
155	30484	55.43	120.55	1959	0.38	0.25	1.45	0.26	1.19	0.25	-0.27	0.35	-1.46	0.35	1.00	0.34
156	30493	55.97	124.88	1940	0.20	0.45	0.83	0.45	1.10	0.45	-0.11	0.35	-0.55	0.35	1.00	0.35
157	30504	54.6	100.63	1940	0.05	0.09	0.21	0.09	1.02	0.09	-0.05	0.14	-0.25	0.14	1.00	0.14
158	30521	54.8	105.17	1938	0.04	0.11	0.19	0.11	1.02	0.11	-0.04	0.13	-0.17	0.13	1.00	0.13
159	30536	54.33	109.53	1959	-0.03	0.12	-0.15	0.12	1.00	0.11	-0.08	0.11	-0.35	0.11	1.00	0.11

	No.	Latitude (N)	Longitude (E)	Year	Dry spells						Wet spells					
					Clayton		Frank		Gumbel-Hougaard		Clayton		Frank		Gumbel-Hougaard	
					τ	RMSE	τ	RMSE	τ	RMSE	τ	RMSE	τ	RMSE	τ	RMSE
160	30554	54.47	113.58	1936	0.12	0.15	0.51	0.15	1.06	0.14	-0.04	0.14	-0.19	0.14	1.00	0.14
161	30555	54.62	113.13	1938	0.44	0.35	1.66	0.35	1.22	0.35	-0.19	0.46	-0.93	0.46	1.00	0.46
162	30565	54.43	116.53	1959	0.23	0.11	0.92	0.11	1.11	0.10	-0.25	0.25	-1.31	0.25	1.00	0.24
163	30612	54	103.07	1962	0.19	0.13	0.78	0.13	1.09	0.13	-0.08	0.15	-0.38	0.15	1.00	0.15
164	30627	53.1	105.53	1961	0.04	0.14	0.18	0.14	1.02	0.14	-0.07	0.59	-0.31	0.59	1.00	0.59
165	30632	53.85	108.58	1950	0.20	0.61	0.83	0.61	1.10	0.61	-0.13	0.54	-0.64	0.54	1.00	0.54
166	30635	53.42	109.02	1933	0.17	0.33	0.73	0.33	1.09	0.33	-0.07	0.13	-0.33	0.13	1.00	0.12
167	30636	53.62	109.63	1898	0.10	0.47	0.42	0.47	1.05	0.46	-0.10	0.41	-0.48	0.41	1.00	0.41
168	30650	53.2	112.78	1940	0.11	0.33	0.48	0.33	1.06	0.33	-0.04	0.14	-0.20	0.14	1.00	0.14
169	30673	53.75	119.73	1910	0.18	0.46	0.75	0.46	1.09	0.45	-0.18	0.38	-0.90	0.38	1.00	0.38
170	30692	54	123.97	1911	0.31	0.28	1.22	0.28	1.15	0.27	-0.12	0.23	-0.55	0.23	1.00	0.23
171	30703	52.97	101.98	1940	0.28	0.33	1.10	0.33	1.14	0.33	-0.17	0.34	-0.82	0.34	1.00	0.33
172	30710	52.27	104.35	1834	0.17	0.25	0.72	0.25	1.09	0.25	-0.05	0.32	-0.22	0.32	1.00	0.32
173	30716	52.47	104.37	1959	0.09	0.20	0.38	0.20	1.04	0.20	-0.14	0.40	-0.68	0.40	1.00	0.40
174	30727	52.03	105.42	1940	0.11	0.28	0.47	0.28	1.06	0.28	-0.19	0.26	-0.95	0.26	1.00	0.26
175	30745	52.53	111.55	1940	0.19	0.29	0.78	0.29	1.09	0.29	-0.09	0.25	-0.42	0.25	1.00	0.25
176	30758	52.08	113.48	1890	0.17	0.33	0.72	0.33	1.09	0.33	-0.03	0.24	-0.15	0.24	1.00	0.24
177	30777	52.23	117.7	1940	0.32	0.32	1.28	0.32	1.16	0.31	-0.21	0.17	-1.05	0.17	1.00	0.15
178	30811	51.73	102.53	1961	0.03	0.09	0.12	0.09	1.01	0.09	-0.03	0.13	-0.15	0.13	1.00	0.13
179	30815	51.53	103.6	1936	0.31	0.37	1.23	0.37	1.16	0.37	-0.16	0.41	-0.77	0.41	1.00	0.41
180	30822	51.72	105.85	1940	0.23	0.30	0.92	0.30	1.11	0.30	-0.04	0.39	-0.20	0.39	1.00	0.39
181	30823	51.83	107.6	1847	0.09	0.32	0.39	0.32	1.05	0.32	-0.03	0.33	-0.14	0.33	1.00	0.33
182	30825	51.75	107.28	1961	0.10	0.22	0.44	0.22	1.05	0.22	0.05	0.27	0.22	0.27	1.03	0.27
183	30844	51.35	110.47	1940	0.37	0.18	1.44	0.18	1.19	0.18	-0.10	0.22	-0.48	0.22	1.00	0.22
184	30915	50.43	103.6	1940	0.13	0.27	0.56	0.27	1.07	0.27	-0.12	0.30	-0.58	0.30	1.00	0.30
185	30925	50.37	106.45	1940	0.04	0.24	0.16	0.24	1.02	0.24	-0.09	0.29	-0.43	0.29	1.00	0.29
186	30935	50.37	108.75	1940	0.21	0.36	0.88	0.36	1.11	0.36	-0.15	0.25	-0.74	0.25	1.00	0.24

	No.	Latitude (N)	Longitude (E)	Year	Dry spells						Wet spells					
					Clayton		Frank		Gumbel-Hougaard		Clayton		Frank		Gumbel-Hougaard	
					τ	RMSE	τ	RMSE	τ	RMSE	τ	RMSE	τ	RMSE	τ	RMSE
187	30949	49.57	111.97	1927	0.46	0.14	1.73	0.15	1.23	0.13	-0.24	0.17	-1.23	0.17	1.00	0.15
188	30954	49.7	112.67	1940	0.49	0.29	1.83	0.29	1.25	0.28	-0.29	0.25	-1.56	0.25	1.00	0.24
189	31004	58.62	125.03	1926	0.46	0.28	1.75	0.28	1.23	0.27	-0.26	0.15	-1.37	0.16	1.00	0.13
190	31026	58.73	130.62	1940	0.19	0.53	0.78	0.53	1.09	0.53	0.00	0.16	-0.01	0.16	1.00	0.16
191	31062	59.77	137.67	1945	0.31	0.23	1.21	0.24	1.15	0.21	-0.26	0.18	-1.40	0.18	1.00	0.15
192	31088	59.37	143.2	1843	0.29	0.30	1.15	0.30	1.14	0.30	-0.14	0.14	-0.66	0.14	1.00	0.13
193	31102	57.65	125.97	1950	0.51	0.26	1.89	0.26	1.25	0.26	-0.35	0.67	-1.96	0.67	1.00	0.66
194	31137	56.28	131.13	1945	0.08	0.12	0.35	0.12	1.04	0.11	-0.13	0.18	-0.62	0.18	1.00	0.17
195	31152	57.65	136.15	1940	0.38	0.11	1.48	0.11	1.19	0.10	-0.25	0.14	-1.32	0.14	1.00	0.12
196	31168	56.45	138.15	1891	0.42	0.17	1.60	0.17	1.21	0.17	-0.19	0.14	-0.95	0.14	1.00	0.13
197	31235	55.33	134.5	1959	0.45	0.14	1.70	0.13	1.22	0.13	-0.25	0.47	-1.29	0.47	1.00	0.47
198	31253	54.72	128.87	1909	0.50	0.35	1.87	0.35	1.25	0.35	-0.24	0.28	-1.24	0.28	1.00	0.28
199	35041	52.43	60.35	1940	0.56	0.31	2.05	0.31	1.28	0.31	-0.28	0.39	-1.49	0.39	1.00	0.38
200	35078	51.82	68.37	1936	0.60	0.23	2.18	0.23	1.30	0.23	-0.24	0.39	-1.23	0.39	1.00	0.38
201	35133	51.52	59.95	1936	0.63	0.28	2.27	0.28	1.32	0.28	-0.34	0.22	-1.90	0.22	1.00	0.20
202	35188	51.13	71.37	1881	0.45	0.37	1.70	0.37	1.22	0.37	-0.30	0.17	-1.65	0.17	1.00	0.15
203	35233	50.75	59.55	1937	0.46	0.29	1.72	0.29	1.23	0.29	-0.30	0.47	-1.60	0.48	1.00	0.47
204	35358	49.63	63.5	1900	0.46	0.28	1.73	0.28	1.23	0.28	-0.17	0.20	-0.86	0.20	1.00	0.19
205	35394	49.8	73.15	1936	0.23	0.39	0.95	0.39	1.12	0.39	-0.20	0.40	-0.99	0.40	1.00	0.39
206	35576	48.3	69.65	1937	0.23	0.43	0.93	0.43	1.11	0.43	-0.29	0.54	-1.54	0.54	1.00	0.53
207	35663	47.83	66.75	1926	0.20	0.30	0.82	0.30	1.10	0.29	-0.19	0.28	-0.93	0.28	1.00	0.28
208	35796	46.8	75.08	1936	0.17	0.37	0.71	0.37	1.09	0.37	-0.16	0.40	-0.77	0.40	1.00	0.40
209	36034	51.58	81.2	1924	0.33	0.34	1.31	0.34	1.17	0.33	-0.23	0.56	-1.16	0.56	1.00	0.56
210	36038	51.15	82.17	1901	0.52	0.71	1.92	0.71	1.26	0.70	-0.24	0.33	-1.23	0.33	1.00	0.32
211	36045	51.63	84.33	1955	0.42	0.12	1.59	0.12	1.21	0.12	-0.13	0.25	-0.63	0.25	1.00	0.25
212	36055	51.9	86	1940	0.44	0.09	1.66	0.09	1.22	0.08	-0.14	0.30	-0.67	0.30	1.00	0.29
213	36064	51.77	87.6	1940	0.21	0.12	0.85	0.12	1.10	0.11	-0.14	0.40	-0.69	0.40	1.00	0.40

	No.	Latitude (N)	Longitude (E)	Year	Dry spells						Wet spells					
					Clayton		Frank		Gumbel-Hougaard		Clayton		Frank		Gumbel-Hougaard	
					τ	RMSE	τ	RMSE	τ	RMSE	τ	RMSE	τ	RMSE	τ	RMSE
214	36096	51.72	94.5	1943	0.31	0.34	1.23	0.34	1.16	0.34	-0.18	0.48	-0.89	0.48	1.00	0.47
215	36099	51.15	94.52	1961	0.30	0.22	1.20	0.22	1.15	0.22	-0.23	0.15	-1.16	0.15	1.00	0.13
216	36103	52.47	96.1	1945	0.04	0.13	0.18	0.13	1.02	0.13	0.06	1.15	0.26	1.15	1.03	1.15
217	36177	50.42	80.3	1901	0.16	0.09	0.69	0.09	1.08	0.09	-0.15	0.31	-0.72	0.31	1.00	0.31
218	36229	50.27	85.62	1940	0.37	0.25	1.45	0.25	1.19	0.25	-0.17	0.39	-0.83	0.39	1.00	0.39
219	36259	50	88.67	1933	0.44	0.22	1.66	0.23	1.22	0.21	-0.30	0.13	-1.65	0.13	1.00	0.11
220	36278	50.38	90.43	1961	0.36	0.46	1.39	0.46	1.18	0.46	-0.28	0.48	-1.47	0.48	1.00	0.48
221	36307	50.27	95.12	1949	0.19	0.21	0.80	0.21	1.10	0.21	-0.27	0.40	-1.42	0.40	1.00	0.39

Bibliography

Adam, J. C., I. Haddeland, F. Su, and D. P. Lettenmaier, 2007: Simulation of reservoir influences on annual and seasonal streamflow changes for the Lena, Yenisei, and Ob' rivers. *Journal of Geophysical Research: Atmospheres*, **112**.

Adamowski, J., and K. Sun, 2010: Development of a coupled wavelet transform and neural network method for flow forecasting of non-perennial rivers in semi-arid watersheds. *Journal of Hydrology*, **390,** 85-91.

Adankon, M. M., M. Cheriet, and A. Biem, 2011: Semisupervised Learning Using Bayesian Interpretation: Application to LS-SVM. *IEEE Transactions on Neural Networks*, **22,** 513-524.

ÅDlandsvik, B., and H. Loeng, 1991: A study of the climatic system in the Barents Sea. *Polar Research*, **10,** 45-50.

Armitage, T. W. K., S. Bacon, and R. Kwok, 2018: Arctic Sea Level and Surface Circulation Response to the Arctic Oscillation. *Geophysical Research Letters*, **45,** 6576-6584.

Arnell, N. W., 2005: Implications of climate change for freshwater inflows to the Arctic Ocean. *Journal of Geophysical Research*, **110**.

Arya Farid, K., and L. Zhang, 2017: Copula-Based Markov Process for Forecasting and Analyzing Risk of Water Quality Time Series. *Journal of Hydrologic Engineering*, **22,** 04017005.

Assel, R. A., 1992: Great Lakes Winter-Weather 700-hPa PNA Teleconnections. *Monthly Weather Review*, **120,** 2156-2163.

Balzter, H., and Coauthors, 2007: Coupling of Vegetation Growing Season Anomalies and Fire Activity with Hemispheric and Regional-Scale Climate Patterns in Central and East Siberia. *Journal of Climate*, **20,** 3713-3729.

Barbosa, S. M., 2008: Quantile trends in Baltic sea level. *Geophysical Research Letters*, **35**.

Berezovskaya, S., D. Yang, and D. L. Kane, 2004: Compatibility analysis of precipitation and runoff trends over the large Siberian watersheds. *Geophysical Research Letters*, **31**.

Bingyi, W., and W. Jia, 2002: Possible impacts of winter Arctic Oscillation on Siberian high, the East Asian winter monsoon and sea–ice extent. *Advances in Atmospheric Sciences*, **19,** 297-320.

Bintanja, R., and F. M. Selten, 2014: Future increases in Arctic precipitation linked to local evaporation and sea-ice retreat. *Nature*, **509,** 479-482.

Bintanja, R., E. C. van der Linden, and W. Hazeleger, 2011: Boundary layer stability and Arctic climate change: a feedback study using EC-Earth. *Climate Dynamics*, **39,** 2659-2673.

Bintanja, R., C. Katsman, and F. Selten, 2018: Increased Arctic Precipitation Slows Down Sea Ice Melt and Surface Warming. *Oceanography*, **31**.

Bladé, I., B. Liebmann, D. Fortuny, and G. J. van Oldenborgh, 2012: Observed and simulated impacts of the summer NAO in Europe: implications for projected drying in the Mediterranean region. *Climate Dynamics*, **39,** 709-727.

Boisvert, L. N., and J. C. Stroeve, 2015: The Arctic is becoming warmer and wetter as revealed by the Atmospheric Infrared Sounder. *Geophysical Research Letters*, **42,** 4439-4446.

Bony, S., and Coauthors, 2015: Clouds, circulation and climate sensitivity. *Nature Geoscience*, **8,** 261.

Boser, B. E., I. M. Guyon, and V. N. Vapnik, 1992: A training algorithm for optimal margin classifiers. *Proceedings of the fifth annual workshop on Computational learning theory*, Association for Computing Machinery, 144–152.

Bring, A., and Coauthors, 2016: Arctic terrestrial hydrology: A synthesis of processes, regional effects, and research challenges. *Journal of Geophysical Research: Biogeosciences*, **121,** 621-649.

Buchinsky, M., 1991: The theory and practice of quantile regression, Harvard University.

Bulygina, O. N., V. N. Razuvaev, and N. N. Korshunova, 2009: Changes in snow cover over Northern Eurasia in the last few decades. *Environmental Research Letters*, **4,** 045026.

Cade, B. S., and B. R. Noon, 2003: A gentle introduction to quantile regression for ecologists. *Frontiers in Ecology and the Environment*, **1,** 412-420.

Caian, M., T. Koenigk, R. Döscher, and A. Devasthale, 2018: An interannual link between Arctic sea-ice cover and the North Atlantic Oscillation. *Climate Dynamics*, **50,** 423-441.

Cannon, A., 2018: Non-crossing nonlinear regression quantiles by monotone composite quantile regression neural network, with application to rainfall extremes.

Cavalieri, D. J., and C. L. Parkinson, 2012: Arctic sea ice variability and trends, 1979-2010. *Cryosphere*, **6,** 881-889.

Ceppi, P., F. Brient, M. D. Zelinka, and D. L. Hartmann, 2017: Cloud feedback mechanisms and their representation in global climate models. *WIREs Climate Change*, **8,** e465.

Chapin III, F. S., and Coauthors, 2005: Role of Land-Surface Changes in Arctic Summer Warming. *Science*, **310,** 657-660.

Chen, L., and V. P. Singh, 2018: Entropy-based derivation of generalized distributions for hydrometeorological frequency analysis. *Journal of Hydrology*, **557,** 699-712.

Chen, L., V. P. Singh, S. Guo, J. Zhou, and J. Zhang, 2015: Copula-based method for multisite monthly and daily streamflow simulation. *Journal of Hydrology*, **528,** 369-384.

Chernokulsky, A., F. Kozlov, O. Zolina, O. Bulygina, and V. Semenov, 2018: Climatology of Precipitation of Different Genesis in Northern Eurasia. *Russian Meteorology and Hydrology*, **43,** 425-435.

Chernokulsky, A., F. Kozlov, O. Zolina, O. Bulygina, I. Mokhov, and V. Semenov, 2019: Observed changes in convective and stratiform precipitation in Northern Eurasia over the last five decades. *Environmental Research Letters*, **14,** 045001.

Chitralekha, S. B., and S. L. Shah, 2010: Support Vector Regression for soft sensor design of nonlinear processes. *18th Mediterranean Conference on Control and Automation, MED'10*, 569-574.

Cohen, J., J. Foster, M. Barlow, K. Saito, and J. Jones, 2010: Winter 2009–2010: A case study of an extreme Arctic Oscillation event. *Geophysical Research Letters*, **37**.

Cohn, T. A., and H. F. Lins, 2005: Nature's style: Naturally trendy. *Geophysical Research Letters*, **32**.

Cortes, C., and V. Vapnik, 1995: Support-vector networks. *Machine Learning*, **20,** 273-297.

Dee, D. P., and Coauthors, 2011: The ERA-Interim reanalysis: configuration and performance of the data assimilation system. *Quarterly Journal of the Royal Meteorological Society*, **137,** 553-597.

Delworth, T. L., 2000: Simulation of Early 20th Century Global Warming. *Science*, **287,** 2246-2250.

Derksen, C., and R. Brown, 2012: Spring snow cover extent reductions in the 2008-2012 period exceeding climate model projections. *Geophysical Research Letters*, **39,** n/a-n/a.

Déry, S. J., M. A. Hernández-Henríquez, J. E. Burford, and E. F. Wood, 2009: Observational evidence of an intensifying hydrological cycle in northern Canada. *Geophysical Research Letters*, **36**.

Deser, C., and K. E. Trenberth, 2016: The Climate Data Guide: Pacific Decadal Oscillation (PDO): Definition and Indices. N. C. f. A. Research, Ed.

Dessler, A. E., M. R. Schoeberl, T. Wang, S. M. Davis, and K. H. Rosenlof, 2013: Stratospheric water vapor feedback. *Proceedings of the National Academy of Sciences of the United States of America*, **110,** 18087-18091.

Ding, Q., and Coauthors, 2017a: Influence of high-latitude atmospheric circulation changes on summertime Arctic sea ice. *Nature Climate Change*, **7,** 289-295.

Ding, Q., and Coauthors, 2019: Fingerprints of internal drivers of Arctic sea ice loss in observations and model simulations. *Nature Geoscience*, **12,** 28-33.

Ding, S., W. Chen, J. Feng, and H.-F. Graf, 2017b: Combined Impacts of PDO and Two Types of La Niña on Climate Anomalies in Europe. *Journal of Climate*, **30,** 3253-3278.

Dirmeyer, P. A., Y. Jin, B. Singh, and X. Yan, 2013: Trends in Land–Atmosphere Interactions from CMIP5 Simulations. *Journal of Hydrometeorology*, **14,** 829-849.

Drucker, H., C. J. C. Burges, L. Kaufman, A. J. Smola, and V. Vapnik, 1997: Support vector regression machines. 155-161.

Durocher, M., A. I. Requena, D. H. Burn, and J. Pellerin, 2019: Analysis of trends in annual streamflow to the Arctic Ocean. *Hydrological Processes*, **33,** 1143-1151.

Elmendorf, S. C., and Coauthors, 2012: Plot-scale evidence of tundra vegetation change and links to recent summer warming. *Nature Climate Change*, **2,** 453.

Enfield, D. B., A. M. Mestas-Nuñez, and P. J. Trimble, 2001: The Atlantic Multidecadal Oscillation and its relation to rainfall and river flows in the continental U.S. *Geophysical Research Letters*, **28,** 2077-2080.

England, M., A. Jahn, and L. Polvani, 2019: Nonuniform Contribution of Internal Variability to Recent Arctic Sea Ice Loss. *Journal of Climate*, **32,** 4039-4053.

Esau, I., V. V. Miles, R. Davy, M. W. Miles, and A. Kurchatova, 2016: Trends in normalized difference vegetation index (NDVI) associated with urban development in northern West Siberia. *Atmos. Chem. Phys.*, **16,** 9563-9577.

Fan, L., and D. Chen, 2016: Trends in extreme precipitation indices across China detected using quantile regression. *Atmospheric Science Letters*, **17,** 400-406.

Feldl, N., B. T. Anderson, and S. Bordoni, 2017: Atmospheric Eddies Mediate Lapse Rate Feedback and Arctic Amplification. *Journal of Climate*, **30,** 9213-9224.

Fetterer, F., K. Knowles, W. Meier, M. Savoie, and A. K. Windnagel, 2017: updated daily. Sea Ice Index, Version 3. 3 ed., C. U. N. N. S. a. I. D. C. Boulder, Ed.

Froidurot, S., and A. Diedhiou, 2017: Characteristics of wet and dry spells in the West African monsoon system. *Atmospheric Science Letters*, **18,** 125-131.

Fukutomi, Y., H. Igarashi, K. Masuda, and T. Yasunari, 2003: Interannual Variability of Summer Water Balance Components in Three Major River Basins of Northern Eurasia. *Journal of Hydrometeorology*, **4,** 283-296.

Gan, T. Y., A. K. Gobena, and Q. Wang, 2007: Precipitation of southwestern Canada: Wavelet, scaling, multifractal analysis, and teleconnection to climate anomalies. *Journal of Geophysical Research: Atmospheres*, **112**.

Gao, M., and C. L. E. Franzke, 2017: Quantile Regression–Based Spatiotemporal Analysis of Extreme Temperature Change in China. *Journal of Climate*, **30,** 9897-9914.

Ghumman, A. R., Y. M. Ghazaw, A. R. Sohail, and K. Watanabe, 2011: Runoff forecasting by artificial neural network and conventional model. *Alexandria Engineering Journal*, **50,** 345-350.

Gitau, W., P. Camberlin, L. Ogallo, and E. Bosire, 2018: Trends of intraseasonal descriptors of wet and dry spells over equatorial eastern Africa. *International Journal of Climatology*, **38,** 1189-1200.

Gong, D. Y., and C. H. Ho, 2002: The Siberian High and climate change over middle to high latitude Asia. *Theoretical and Applied Climatology*, **72,** 1-9.

Graversen, R. G., P. L. Langen, and T. Mauritsen, 2014: Polar Amplification in CCSM4: Contributions from the Lapse Rate and Surface Albedo Feedbacks. *Journal of Climate*, **27,** 4433-4450.

Graversen, R. G., T. Mauritsen, M. Tjernstrom, E. Kallen, and G. Svensson, 2008: Vertical structure of recent Arctic warming. *Nature*, **451,** 53-56.

Groisman, P. Y., and Coauthors, 2007: Potential forest fire danger over Northern Eurasia: Changes during the 20th century. *Global and Planetary Change*, **56,** 371-386.

Guo, J., J. Zhou, H. Qin, Q. Zou, and Q. Li, 2011: Monthly streamflow forecasting based on improved support vector machine model. *Expert Systems with Applications*, **38,** 13073-13081.

Hamed, K. H., 2008: Trend detection in hydrologic data: The Mann–Kendall trend test under the scaling hypothesis. *Journal of Hydrology*, **349,** 350-363.

Hamman, J., B. Nijssen, A. Roberts, A. Craig, W. Maslowski, and R. Osinski, 2017: The coastal streamflow flux in the Regional Arctic System Model. *Journal of Geophysical Research: Oceans*, **122,** 1683-1701.

Han, W., C. Xiao, T. Dou, and M. Ding, 2018: Changes in the Proportion of Precipitation Occurring as Rain in Northern Canada during Spring–Summer from 1979–2015. *Advances in Atmospheric Sciences*, **35,** 1129-1136.

Harris, I. C. J., P.D, 2020: Climatic Research Unit (CRU) Time-Series (TS) version 4.03 of high-resolution gridded data of month-by-month variation in climate (Jan. 1901- Dec. 2018). U. o. E. A. C. R. U. C. f. E. D. Analysis, Ed.

Hegyi, B. M., and P. C. Taylor, 2017: The regional influence of the Arctic Oscillation and Arctic Dipole on the wintertime Arctic surface radiation budget and sea ice growth. *Geophysical Research Letters*, **44,** 4341-4350.

Held, I. M., and B. J. Soden, 2000: Water vapor feedback and global warming. *Annual Review of Energy and the Environment*, **25,** 441-475.

Hilmer, M., and T. Jung, 2000: Evidence for a recent change in the link between the North Atlantic Oscillation and Arctic Sea ice export. *Geophysical Research Letters*, **27,** 989-992.

Hurrell, J. W., 1995: Decadal Trends in the North Atlantic Oscillation: Regional Temperatures and Precipitation. *Science*, **269,** 676.

Hurrell, J. W., and C. Deser, 2010: North Atlantic climate variability: The role of the North Atlantic Oscillation. *Journal of Marine Systems*, **79,** 231-244.

Hurst, H. E., 1951: Long-term storage capacity of reservoirs. *Trans. Amer. Soc. Civil Eng.*, **116,** 770-799.

Hyo-seok, P., L. Sukyoung, S. Seok-Woo, S. B. Feldstein, and K. Yu, 2015: The Impact of Poleward Moisture and Sensible Heat Flux on Arctic Winter Sea Ice Variability. *Journal of Climate*, **28,** 5030-5041.

Iijima, Y., T. Nakamura, H. Park, Y. Tachibana, and A. N. Fedorov, 2016: Enhancement of Arctic storm activity in relation to permafrost degradation in eastern Siberia. *International Journal of Climatology*, **36,** 4265-4275.

IPCC, I. P. O. C., 2014: Fifth Assessment Report–AR5. *Disponível em: http://www. ipcc. ch/report/ar5/>. Acesso em*, **20**.

Jevrejeva, S., J. C. Moore, and A. Grinsted, 2003: Influence of the arctic oscillation and El Nino-Southern Oscillation (ENSO) on ice conditions in the Baltic Sea: The wavelet approach. *J Geophys Res-Atmos*, **108**.

Jorgenson, M. T., and Coauthors, 2010: Resilience and vulnerability of permafrost to climate change. *Canadian Journal of Forest Research*, **40,** 1219-1236.

Kalteh, A. M., 2013: Monthly river flow forecasting using artificial neural network and support vector regression models coupled with wavelet transform. *Computers & Geosciences*, **54,** 1-8.

Kashiwase, H., K. I. Ohshima, S. Nihashi, and H. Eicken, 2017: Evidence for ice-ocean albedo feedback in the Arctic Ocean shifting to a seasonal ice zone. *Scientific reports*, **7,** 8170.

Kattsov, V. M., J. E. Walsh, W. L. Chapman, V. A. Govorkova, T. V. Pavlova, and X. Zhang, 2007: Simulation and Projection of Arctic Freshwater Budget Components by the IPCC AR4 Global Climate Models. *Journal of Hydrometeorology*, **8,** 571-589.

Kay, J. E., M. M. Holland, and A. Jahn, 2011: Inter-annual to multi-decadal Arctic sea ice extent trends in a warming world. *Geophysical Research Letters*, **38**.

Kendall, M. G., 1955: Rank correlation methods.

Knutson, T. R., and Coauthors, 2006: Assessment of Twentieth-Century Regional Surface Temperature Trends Using the GFDL CM2 Coupled Models. *Journal of Climate*, **19,** 1624-1651.

Koenker, and Bassett, 1978: Regression Quantiles. *Econometrica*, **46,** 33-50.

Koenker, R.: Quantreg: quantile regression and related methods. R package version 5.34. https://cran.r-project.org/web/packages/quantreg/quantreg.pdf

Koenker, R., and K. F. Hallock, 2001: Quantile Regression. *Journal of Economic Perspectives*, **15,** 143-156.

Koenker, R. W., and V. D'Orey, 1987: Algorithm AS 229: Computing Regression Quantiles. *Journal of the Royal Statistical Society. Series C (Applied Statistics)*, **36,** 383-393.

Koutsoyiannis, D., and A. Montanari, 2007: Statistical analysis of hydroclimatic time series: Uncertainty and insights. *Water Resources Research*, **43**.

Kumar, S., P. A. Dirmeyer, V. Merwade, T. DelSole, J. M. Adams, and D. Niyogi, 2013: Land use/cover change impacts in CMIP5 climate simulations: A new methodology and 21st century challenges. *Journal of Geophysical Research: Atmospheres*, **118,** 6337-6353.

Kwok, R., 2000: Recent changes in Arctic Ocean sea ice motion associated with the North Atlantic Oscillation. *Geophysical Research Letters*, **27,** 775-778.

——, 2018: Arctic sea ice thickness, volume, and multiyear ice coverage: losses and coupled variability (1958–2018). *Environmental Research Letters*, **13,** 105005.

Kwok, R., G. Spreen, and S. Pang, 2013: Arctic sea ice circulation and drift speed: Decadal trends and ocean currents. *Journal of Geophysical Research: Oceans*, **118,** 2408-2425.

Kyselý, J., J. Picek, and R. Beranová, 2010: Estimating extremes in climate change simulations using the peaks-over-threshold method with a non-stationary threshold. *Global and Planetary Change*, **72,** 55-68.

L'Heureux, M. L., A. Kumar, G. D. Bell, M. S. Halpert, and R. W. Higgins, 2008: Role of the Pacific-North American (PNA) pattern in the 2007 Arctic sea ice decline. *Geophysical Research Letters*, **35**.

Lammers, R. B., A. I. Shiklomanov, C. J. Vörösmarty, B. M. Fekete, and B. J. Peterson, 2016: R-ArcticNet, A Regional Hydrographic Data Network for the Pan-Arctic Region (ISO-image of CD-ROM). *Supplement to: Lammers, RB et al. (2001): Assessment of contemporary Arctic river runoff based on observational discharge records. Journal of Geophysical Research: Atmospheres, 106(D4), 3321-3334, https://doi.org/10.1029/2000JD900444*, PANGAEA.

Landerer, F. W., J. O. Dickey, and A. Güntner, 2010: Terrestrial water budget of the Eurasian pan-Arctic from GRACE satellite measurements during 2003–2009. *Journal of Geophysical Research: Atmospheres*, **115**.

Landy, J. C., J. K. Ehn, and D. G. Barber, 2015: Albedo feedback enhanced by smoother Arctic sea ice. *Geophysical Research Letters*, **42,** 10,714-710,720.

Laurent, C., and S. Parey, 2007: Estimation of 100-year-return-period temperatures in France in a non-stationary climate: Results from observations and IPCC scenarios. *Global and Planetary Change*, **57,** 177-188.

Leathers, D. J., B. Yarnal, and M. A. Palecki, 1991: The Pacific/North American Teleconnection Pattern and United States Climate. Part I: Regional Temperature and Precipitation Associations. *Journal of Climate*, **4,** 517-528.

Lee, S., 2012: Testing of the Tropically Excited Arctic Warming Mechanism (TEAM) with Traditional El Niño and La Niña. *Journal of Climate*, **25,** 4015-4022.

Li, A. K., H. Paek, and J.-Y. Yu, 2016a: The changing influences of the AMO and PDO on the decadal variation of the Santa Ana winds. *Environmental Research Letters*, **11,** 064019.

Li, F., and Q. Zheng, 2016: Probabilistic modelling of flood events using the entropy copula. *Advances in Water Resources*, **97,** 233-240.

Li, J., and S. Tan, 2015: Nonstationary Flood Frequency Analysis for Annual Flood Peak Series, Adopting Climate Indices and Check Dam Index as Covariates. *Water Resources Management*, **29,** 5533-5550.

Li, X., A. Meshgi, and V. Babovic, 2016b: Spatio-temporal variation of wet and dry spell characteristics of tropical precipitation in Singapore and its association with ENSO. *International Journal of Climatology*, **36,** 4831-4846.

Li, Z., Y. Li, X. Shi, and J. Li, 2017: The characteristics of wet and dry spells for the diverse climate in China. *Global and Planetary Change*, **149,** 14-19.

Lindsay, R., and A. Schweiger, 2015: Arctic sea ice thickness loss determined using subsurface, aircraft, and satellite observations. *The Cryosphere*, **9,** 269-283.

Liu, J. P., J. A. Curry, and Y. Y. Hu, 2004: Recent Arctic Sea Ice Variability: Connections to the Arctic Oscillation and the ENSO. *Geophysical Research Letters*, **31,** n/a-n/a.

MacDonald, G. M., K. V. Kremenetski, L. C. Smith, and H. G. Hidalgo, 2007: Recent Eurasian river discharge to the Arctic Ocean in the context of longer-term dendrohydrological records. *Journal of Geophysical Research: Biogeosciences*, **112**.

Macias-Fauria, M., B. C. Forbes, P. Zetterberg, and T. Kumpula, 2012: Eurasian Arctic greening reveals teleconnections and the potential for structurally novel ecosystems. *Nature Climate Change*, **2,** 613.

Malik, N., B. Bookhagen, and P. J. Mucha, 2016: Spatiotemporal patterns and trends of Indian monsoonal rainfall extremes. *Geophysical Research Letters*, **43,** 1710-1717.

Mauritsen, T., 2016: Greenhouse warming unleashed. *Nature Geoscience*, **9,** 268-+.

McCabe, G. J., M. A. Palecki, and J. L. Betancourt, 2004: Pacific and Atlantic Ocean influences on multidecadal drought frequency in the United States. *Proceedings of the National Academy of Sciences*, **101,** 4136.

McClelland, J. W., R. M. Holmes, B. J. Peterson, and M. Stieglitz, 2004: Increasing river discharge in the Eurasian Arctic: Consideration of dams, permafrost thaw, and fires as potential agents of change. *Journal of Geophysical Research: Atmospheres*, **109**.

McClelland, J. W., S. J. Déry, B. J. Peterson, R. M. Holmes, and E. F. Wood, 2006: A pan-arctic evaluation of changes in river discharge during the latter half of the 20th century. *Geophysical Research Letters*, **33**.

McPhee, M. G., T. P. Stanton, J. H. Morison, and D. G. Martinson, 1998: Freshening of the upper ocean in the Arctic: Is perennial sea ice disappearing? *Geophysical Research Letters*, **25,** 1729-1732.

Milly, P. C. D., J. Betancourt, M. Falkenmark, R. M. Hirsch, Z. W. Kundzewicz, D. P. Lettenmaier, and R. J. Stouffer, 2008: Stationarity Is Dead: Whither Water Management? *Science*, **319,** 573.

Mirabbasi, R., A. Fakheri-Fard, and Y. Dinpashoh, 2012: Bivariate drought frequency analysis using the copula method. *Theoretical and Applied Climatology*, **108,** 191-206.

Moore, G. W. K., A. Schweiger, J. Zhang, and M. Steele, 2018: Collapse of the 2017 Winter Beaufort High: A Response to Thinning Sea Ice? *Geophysical Research Letters*, **45,** 2860-2869.

Muggeo, V. M. R., 2003: Estimating regression models with unknown break-points. *Statistics in Medicine*, **22,** 3055-3071.

Muskett, R. R., and V. E. Romanovsky, 2009: Groundwater storage changes in arctic permafrost watersheds from GRACE and in situ measurements. *Environmental Research Letters*, **4,** 045009.

Mwale, D., and T. Y. Gan, 2004: Wavelet Analysis of Variability, Teleconnectivity, and Predictability of the September–November East African Rainfall. *journal of Applied Meteorology*, **44,** 256-270.

Mysak, L. A., R. G. Ingram, J. Wang, and A. van der Baaren, 1996: The anomalous sea-ice extent in Hudson bay, Baffin bay and the Labrador sea during three simultaneous NAO and ENSO episodes. *Atmosphere-Ocean*, **34,** 313-343.

Nabeel, A., and H. Athar, 2018: Classification of precipitation regimes in Pakistan using wet and dry spells. *International Journal of Climatology*, **38,** 2462-2477.

Nijssen, B., G. M. O'Donnell, A. F. Hamlet, and D. P. Lettenmaier, 2001a: Hydrologic Sensitivity of Global Rivers to Climate Change. *Climatic Change*, **50,** 143-175.

Nijssen, B., G. M. O'Donnell, D. P. Lettenmaier, D. Lohmann, and E. F. Wood, 2001b: Predicting the Discharge of Global Rivers. *Journal of Climate*, **14,** 3307-3323.

Numaguti, A., 1999: Origin and recycling processes of precipitating water over the Eurasian continent: Experiments using an atmospheric general circulation model. *Journal of Geophysical Research: Atmospheres*, **104,** 1957-1972.

Nummelin, A., C. Li, and L. H. Smedsrud, 2015: Response of Arctic Ocean stratification to changing river runoff in a column model. *Journal of Geophysical Research: Oceans*, **120,** 2655-2675.

Ogi, M., and J. M. Wallace, 2012: The role of summer surface wind anomalies in the summer Arctic sea ice extent in 2010 and 2011. *Geophysical Research Letters*, **39,** n/a-n/a.

Ogi, M., Y. Tachibana, and K. Yamazaki, 2003: Impact of the wintertime North Atlantic Oscillation (NAO) on the summertime atmospheric circulation. *Geophysical Research Letters*, **30**.

Olonscheck, D., T. Mauritsen, and D. Notz, 2019: Arctic sea-ice variability is primarily driven by atmospheric temperature fluctuations. *Nature Geoscience*, **12,** 430-434.

Onarheim, I. H., T. Eldevik, L. H. Smedsrud, and J. C. Stroeve, 2018: Seasonal and Regional Manifestation of Arctic Sea Ice Loss. *Journal of Climate*, **31,** 4917-4932.

Ottersen, G., and N. C. Stenseth, 2001: Atlantic climate governs oceanographic and ecological variability in the Barents Sea. *Limnology and Oceanography*, **46,** 1774-1780.

Papacharalampous, G., H. Tyralis, and D. Koutsoyiannis, 2019: Comparison of stochastic and machine learning methods for multi-step ahead forecasting of hydrological processes. *Stochastic Environmental Research and Risk Assessment*, **33,** 481-514.

Park, H., T. Yamazaki, K. Yamamoto, and T. Ohta, 2008: Tempo-spatial characteristics of energy budget and evapotranspiration in the eastern Siberia. *Agricultural and Forest Meteorology*, **148,** 1990-2005.

Peterson, B. J., J. McClelland, R. Curry, R. M. Holmes, J. E. Walsh, and K. Aagaard, 2006: Trajectory Shifts in the Arctic and Subarctic Freshwater Cycle. *Science*, **313,** 1061-1066.

Peterson, B. J., and Coauthors, 2002: Increasing River Discharge to the Arctic Ocean. *Science*, **298,** 2171-2173.

Pettitt, A. N., 1979: A non-parametric approach to the change-point problem. *Applied Statistics*, **28,** 126-135.

Petty, A. A., 2018: A Possible Link Between Winter Arctic Sea Ice Decline and a Collapse of the Beaufort High? *Geophysical Research Letters*, **45,** 2879-2882.

Pithan, F., and T. Mauritsen, 2014: Arctic amplification dominated by temperature feedbacks in contemporary climate models. *Nature Geoscience*, **7,** 181-184.

Qian, L., H. Wang, S. Dang, C. Wang, Z. Jiao, and Y. Zhao, 2018: Modelling bivariate extreme precipitation distribution for data-scarce regions using Gumbel–Hougaard copula with maximum entropy estimation. *Hydrological Processes*, **32,** 212-227.

Rachold, V., and Coauthors, 2004: Modern Terrigenous Organic Carbon Input to the Arctic Ocean**,** 33-55.

Rajaee, T., H. Ebrahimi, and V. Nourani, 2019: A review of the artificial intelligence methods in groundwater level modeling. *Journal of Hydrology*, **572,** 336-351.

Ratan, R., and V. Venugopal, 2013: Wet and dry spell characteristics of global tropical rainfall. *Water Resources Research*, **49,** 3830-3841.

Raymond, F., A. Ullmann, P. Camberlin, B. Oueslati, and P. Drobinski, 2018: Atmospheric conditions and weather regimes associated with extreme winter dry spells over the Mediterranean basin. *Climate Dynamics*, **50,** 4437-4453.

Raymond, F., A. Ullmann, Y. Tramblay, P. Drobinski, and P. Camberlin, 2019: Evolution of Mediterranean extreme dry spells during the wet season under climate change. *Regional Environmental Change*, **19,** 2339-2351.

Reginald, R. M., and E. R. Vladimir, 2009: Groundwater storage changes in arctic permafrost watersheds from GRACE and in situ measurements. *Environmental Research Letters*, **4,** 045009.

Rigor, I. G., R. L. Colony, and S. Martin, 2000: Variations in Surface Air Temperature Observations in the Arctic, 1979–97. *Journal of Climate*, **13,** 896-914.

Rigor, I. G., J. M. Wallace, and R. L. Colony, 2002: Response of Sea Ice to the Arctic Oscillation. *Journal of Climate*, **15,** 2648-2663.

Rogers, J. C., 1981: The North Pacific Oscillation. *Journal of Climatology*, **1,** 39-57.

Rood, S. B., S. Kaluthota, L. J. Philipsen, N. J. Rood, and K. P. Zanewich, 2017: Increasing discharge from the Mackenzie River system to the Arctic Ocean. *Hydrological Processes*, **31,** 150-160.

Salvadori, G., and C. De Michele, 2004: Frequency analysis via copulas: Theoretical aspects and applications to hydrological events. *Water Resources Research*, **40**.

Sarhadi, A., D. H. Burn, M. C. Ausin, and M. P. Wiper, 2016: Time-varying nonstationary multivariate risk analysis using a dynamic Bayesian copula. *Water Resources Research*, **52,** 2327-2349.

Savelieva, N. I., I. P. Semiletov, L. N. Vasilevskaya, and S. P. Pugach, 2000: A climate shift in seasonal values of meteorological and hydrological parameters for Northeastern Asia. *Progress in Oceanography*, **47,** 279-297.

Scheepers, H., J. Wang, T. Y. Gan, and C. C. Kuo, 2018: The impact of climate change on inland waterway transport: Effects of low water levels on the Mackenzie River. *Journal of Hydrology*, **566,** 285-298.

Schuur, E. A. G., J. G. Vogel, K. G. Crummer, H. Lee, J. O. Sickman, and T. E. Osterkamp, 2009: The effect of permafrost thaw on old carbon release and net carbon exchange from tundra. *Nature*, **459,** 556.

Screen, J. A., and I. Simmonds, 2011: Declining summer snowfall in the Arctic: causes, impacts and feedbacks. *Climate Dynamics*, **38,** 2243-2256.

Serreze, M. C., and A. J. Etringer, 2003: Precipitation characteristics of the Eurasian Arctic drainage system. *International Journal of Climatology*, **23,** 1267-1291.

Serreze, M. C., and A. P. Barrett, 2010: Characteristics of the Beaufort Sea High. *Journal of Climate*, **24,** 159-182.

——, 2011: Characteristics of the Beaufort Sea High. *Journal of Climate*, **24,** 159-182.

Serreze, M. C., and R. G. Barry, 2011: Processes and impacts of Arctic amplification: A research synthesis. *Global and Planetary Change*, **77,** 85-96.

Serreze, M. C., A. P. Barrett, J. C. Stroeve, D. N. Kindig, and M. M. Holland, 2009: The emergence of surface-based Arctic amplification. *Cryosphere*, **3,** 11-19.

Serreze, M. C., D. H. Bromwich, M. P. Clark, A. J. Etringer, T. Zhang, and R. Lammers, 2002a: Large-scale hydro-climatology of the terrestrial Arctic drainage system. *Journal of Geophysical Research*, **108**.

——, 2002b: Large-scale hydro-climatology of the terrestrial Arctic drainage system. *Journal of Geophysical Research: Atmospheres*, **107,** ALT 1-1-ALT 1-28.

Serreze, M. C., and Coauthors, 2006: The large-scale freshwater cycle of the Arctic. *Journal of Geophysical Research*, **111**.

She, D., A. K. Mishra, J. Xia, L. Zhang, and X. Zhang, 2016: Wet and dry spell analysis using copulas. *International Journal of Climatology*, **36,** 476-491.

Sheridan, S. C., 2003: North American weather-type frequency and teleconnection indices. *International Journal of Climatology*, **23,** 27-45.

Shiklomanov, A. I., R.M. Holmes, J.W. McClelland, S.E. Tank, and R.G.M. Spencer, 2018: Arctic Great Rivers Observatory. . Version 2020/03/20 ed.

Shiklomanov, I. A., 1997: Assessment of water resources and water availability in the world. *Comprehensive Assessment of the Freshwater Re-sources of the World*.

Shiklomanov, I. A., A. I. Shiklomanov, R. B. Lammers, B. J. Peterson, and C. J. Vorosmarty, 2000: The Dynamics of River Water Inflow to the Arctic Ocean. *The Freshwater Budget of the Arctic Ocean*, E. L. Lewis, E. P. Jones, P. Lemke, T. D. Prowse, and P. Wadhams, Eds., Springer Netherlands, 281-296.

Sklar, M., 1959: Fonctions de repartition an dimensions et leurs marges. *Publ. inst. statist. univ. Paris*, **8,** 229-231.

Smith, L. C., T. M. Pavelsky, G. M. MacDonald, A. I. Shiklomanov, and R. B. Lammers, 2007: Rising minimum daily flows in northern Eurasian rivers: A growing influence of groundwater in the high-latitude hydrologic cycle. *Journal of Geophysical Research: Biogeosciences*, **112**.

Solomon, S., K. H. Rosenlof, R. W. Portmann, J. S. Daniel, S. M. Davis, T. J. Sanford, and G. K. Plattner, 2010: Contributions of stratospheric water vapor to decadal changes in the rate of global warming. *Science*, **327,** 1219-1223.

Sraj, M., N. Bezak, and M. Brilly, 2015: Bivariate flood frequency analysis using the copula function: a case study of the Litija station on the Sava River. *Hydrological Processes*, **29,** 225-238.

Steffen, H., J. Müller, and N. Peterseim, 2012: Mass Variations in the Siberian Permafrost Region from GRACE. *Geodesy for Planet Earth*, Berlin, Heidelberg, Springer Berlin Heidelberg, 597-603.

Stroeve, J., T. Markus, W. N. Meier, and J. Miller, 2017: Recent changes in the Arctic melt Season. *Annals of Glaciology*, **44,** 367-374.

Stroeve, J. C., M. C. Serreze, A. Barrett, and D. N. Kindig, 2016: Attribution of recent changes in autumn cyclone associated precipitation in the Arctic. *Tellus A: Dynamic Meteorology and Oceanography*, **63,** 653-663.

Stroeve, J. C., T. Markus, L. Boisvert, J. Miller, and A. Barrett, 2014: Changes in Arctic melt season and implications for sea ice loss. *Geophysical Research Letters*, **41,** 1216-1225.

Stroeve, J. C., V. Kattsov, A. Barrett, M. Serreze, T. Pavlova, M. Holland, and W. N. Meier, 2012: Trends in Arctic sea ice extent from CMIP5, CMIP3 and observations. *Geophysical Research Letters*, **39,** n/a-n/a.

Sturm, M., C. Racine, and K. Tape, 2001: Increasing shrub abundance in the Arctic. *Nature*, **411,** 546.

Su, L., C. Miao, D. Kong, Q. Duan, X. Lei, Q. Hou, and H. Li, 2018: Long-term trends in global river flow and the causal relationships between river flow and ocean signals. *Journal of Hydrology*, **563,** 818-833.

Sun, P., Q. Zhang, C. Cheng, V. P. Singh, and P. Shi, 2017: ENSO-induced drought hazards and wet spells and related agricultural losses across Anhui province, China. *Natural Hazards*, **89,** 963-983.

Swann, A. L., I. Y. Fung, S. Levis, G. B. Bonan, and S. C. Doney, 2010: Changes in Arctic vegetation amplify high-latitude warming through the greenhouse effect. *Proceedings of the National Academy of Sciences*, **107,** 1295.

Tan, X., and T. Y. Gan, 2016: Non-stationary analysis of the frequency and intensity of heavy precipitation over Canada and their relations to large-scale climate patterns. *Climate Dynamics*, **48,** 2983-3001.

Tan, X., and D. Shao, 2017: Precipitation trends and teleconnections identified using quantile regressions over Xinjiang, China. *International Journal of Climatology*, **37,** 1510-1525.

Tan, X., S. Chen, and T. Y. Gan, 2018a: Multi-model extreme event attribution of the weather conducive to the 2016 Fort McMurray wildfire. *Agricultural and Forest Meteorology*, **260-261,** 109-117.

Tan, X., T. Y. Gan, S. Chen, and B. Liu, 2018b: Modeling distributional changes in winter precipitation of Canada using Bayesian spatiotemporal quantile regression subjected to different teleconnections. *Climate Dynamics*.

Tan, X. Z., T. Y. Gan, and D. G. Shao, 2016: Wavelet analysis of precipitation extremes over Canadian ecoregions and teleconnections to large-scale climate anomalies. *J Geophys Res-Atmos*, **121,** 14469-14486.

Tananaev, N. I., O. M. Makarieva, and L. S. Lebedeva, 2016: Trends in annual and extreme flows in the Lena River basin, Northern Eurasia. *Geophysical Research Letters*, **43,** 10,764-710,772.

Tape, K., M. Sturm, and C. Racine, 2006: The evidence for shrub expansion in Northern Alaska and the Pan-Arctic. *Global Change Biology*, **12,** 686-702.

Tareghian, R., and P. Rasmussen, 2013: Analysis of Arctic and Antarctic sea ice extent using quantile regression. *International Journal of Climatology*, **33,** 1079-1086.

Thompson, D. W. J., and J. M. Wallace, 1998: The Arctic Oscillation signature in the wintertime geopotential height and temperature fields. *Geophysical Research Letters*, **25,** 1297-1300.

Thorndike, A. S., and R. Colony, 1982: Sea ice motion in response to geostrophic winds. *Journal of Geophysical Research: Oceans*, **87,** 5845-5852.

Torre Jorgenson, M., and Coauthors, 2013: Reorganization of vegetation, hydrology and soil carbon after permafrost degradation across heterogeneous boreal landscapes. *Environmental Research Letters*, **8,** 035017.

Trenberth, K. E., 1997: The Definition of El Niño. *Bulletin of the American Meteorological Society*, **78,** 2771-2778.

Varlamova, E., and V. Solovyev, 2016: *Study of NDVI vegetation index in East Siberia under global warming*. Vol. 10035, SPIE.

Vavrus, S., 2004: The impact of cloud feedbacks on Arctic climate under greenhouse forcing. *Journal of Climate*, **17,** 603-615.

Vicente-Serrano, S. M., S. Beguería, and J. I. López-Moreno, 2010: A Multiscalar Drought Index Sensitive to Global Warming: The Standardized Precipitation Evapotranspiration Index. *Journal of Climate*, **23,** 1696-1718.

Villarini, G., J. A. Smith, and G. A. Vecchi, 2012: Changing Frequency of Heavy Rainfall over the Central United States. *Journal of Climate*, **26,** 351-357.

Vinnarasi, R., and C. T. Dhanya, 2016: Changing characteristics of extreme wet and dry spells of Indian monsoon rainfall. *Journal of Geophysical Research: Atmospheres*, **121,** 2146-2160.

von Storch, H., 1999: Misuses of Statistical Analysis in Climate Research. *Analysis of Climate Variability*, Berlin, Heidelberg, Springer Berlin Heidelberg, 11-26.

Vörösmarty, C. J., and D. Sahagian, 2000: Anthropogenic Disturbance of the Terrestrial Water Cycle. *BioScience*, **50,** 753-765.

Wagner, A., G. Lohmann, and M. Prange, 2011: Arctic river discharge trends since 7ka BP. *Global and Planetary Change*, **79,** 48-60.

Walvoord, M. A., and R. G. Striegl, 2007: Increased groundwater to stream discharge from permafrost thawing in the Yukon River basin: Potential impacts on lateral export of carbon and nitrogen. *Geophysical Research Letters*, **34**.

Walvoord, M. A., and B. L. Kurylyk, 2016: Hydrologic Impacts of Thawing Permafrost—A Review. *Vadose Zone Journal*, **15**.

Wang, H., and Coauthors, 2012: Increased water storage in North America and Scandinavia from GRACE gravity data. *Nature Geoscience*.

Wang, L., C. Derksen, R. Brown, and T. Markus, 2013: Recent changes in pan-Arctic melt onset from satellite passive microwave measurements. *Geophysical Research Letters*, **40,** 522-528.

Wang, M., and J. E. Overland, 2009: A sea ice free summer Arctic within 30 years? *Geophysical Research Letters*, **36,** n/a-n/a.

Watson, V., H. Kooi, and V. Bense, 2013: Potential controls on cold-season river flow behavior in subarctic river basins of Siberia. *Journal of Hydrology*, **489,** 214-226.

Wetherald, R. T., and S. Manabe, 1988: Cloud Feedback Processes in a General-Circulation Model. *Journal of the Atmospheric Sciences*, **45,** 1397-1415.

White, D., and Coauthors, 2007: The arctic freshwater system: Changes and impacts. *J Geophys Res-Biogeo*, **112,** n/a-n/a.

Wu, M.-C., G.-F. Lin, and H.-Y. Lin, 2014: Improving the forecasts of extreme streamflow by support vector regression with the data extracted by self-organizing map. *Hydrological Processes*, **28,** 386-397.

Xu, M., S. Kang, X. Wang, H. Wu, D. Hu, and D. Yang, 2020: Climate and hydrological changes in the Ob River Basin during 1936–2017. *Hydrological Processes*, **n/a**.

Xu, W., D. Yang, Y. Li, and R. Xiao, 2016: Correlation Analysis of Mackenzie River Discharge and NDVI Relationship. *Canadian Journal of Remote Sensing*, **42,** 292-306.

Yamamoto-Kawai, M., F. A. McLaughlin, E. C. Carmack, S. Nishino, K. Shimada, and N. Kurita, 2009: Surface freshening of the Canada Basin, 2003–2007: River runoff versus sea ice meltwater. *Journal of Geophysical Research: Oceans*, **114**.

Yang, D., B. Ye, and A. Shiklomanov, 2004a: Discharge Characteristics and Changes over the Ob River Watershed in Siberia. *Journal of Hydrometeorology*, **5,** 595-610.

Yang, D., B. Ye, and D. L. Kane, 2004b: Streamflow changes over Siberian Yenisei River Basin. *Journal of Hydrology*, **296,** 59-80.

Yang, D., X. Shi, and P. Marsh, 2015: Variability and extreme of Mackenzie River daily discharge during 1973–2011. *Quaternary International*, **380-381,** 159-168.

Yang, D., D. Robinson, Y. Zhao, T. Estilow, and B. Ye, 2003: Streamflow response to seasonal snow cover extent changes in large Siberian watersheds. *Journal of Geophysical Research: Atmospheres*, **108**.

Yang, D., D. L. Kane, L. D. Hinzman, X. Zhang, T. Zhang, and H. Ye, 2002: Siberian Lena River hydrologic regime and recent change. *Journal of Geophysical Research: Atmospheres*, **107,** ACL 14-11-ACL 14-10.

Yang, D. Q., B. S. Ye, and A. Shiklomanov, 2004c: Discharge characteristics and changes over the Ob River watershed in Siberia. *Journal of Hydrometeorology*, **5,** 595-610.

Yang, Q., T. H. Dixon, P. G. Myers, J. Bonin, D. Chambers, and M. R. van den Broeke, 2016: Recent increases in Arctic freshwater flux affects Labrador Sea convection and Atlantic overturning circulation. *Nature communications*, **7,** 10525.

Yaseen, Z. M., A. El-shafie, O. Jaafar, H. A. Afan, and K. N. Sayl, 2015: Artificial intelligence based models for stream-flow forecasting: 2000–2015. *Journal of Hydrology*, **530,** 829-844.

Ye, B., D. Yang, and D. L. Kane, 2003: Changes in Lena River streamflow hydrology: Human impacts versus natural variations. *Water Resources Research*, **39**.

Ye, B., D. Yang, Z. Zhang, and D. L. Kane, 2009: Variation of hydrological regime with permafrost coverage over Lena Basin in Siberia. *Journal of Geophysical Research: Atmospheres*, **114**.

Ye, H., 2008: Changes in Frequency of Precipitation Types Associated with Surface Air Temperature over Northern Eurasia during 1936–90. *Journal of Climate*, **21,** 5807-5819.

——, 2018: Changes in duration of dry and wet spells associated with air temperatures in Russia. *Environmental Research Letters*, **13,** 034036.

Ye, H., and J. Cohen, 2013: A shorter snowfall season associated with higher air temperatures over northern Eurasia. *Environmental Research Letters*, **8,** 014052.

Ye, H., E. J. Fetzer, S. Wong, and B. H. Lambrigtsen, 2017a: Rapid decadal convective precipitation increase over Eurasia during the last three decades of the 20th century. *Science Advances*, **3,** e1600944.

Ye, H., E. J. Fetzer, S. Wong, A. Behrangi, D. Yang, and B. H. Lambrigtson, 2015: Increasing atmospheric water vapor and higher daily precipitation intensity over northern Eurasia. *Geophysical Research Letters*, **42,** 9404-9410.

Ye, H., E. J. Fetzer, S. Wong, B. H. Lambrigtsen, T. Wang, L. Chen, and V. Dang, 2017b: More frequent showers and thunderstorm days under a warming climate: evidence observed over Northern Eurasia from 1966 to 2000. *Climate Dynamics*, **49,** 1933-1944.

Ye, H., and Coauthors, 2014: Impact of increased water vapor on precipitation efficiency over northern Eurasia. *Geophysical Research Letters*, **41,** 2941-2947.

Yilmaz, A. G., and N. Muttil, 2014: Runoff Estimation by Machine Learning Methods and Application to the Euphrates Basin in Turkey. *Journal of Hydrologic Engineering*, **19,** 1015-1025.

Yin, J., S. Guo, S. He, J. Guo, X. Hong, and Z. Liu, 2018: A copula-based analysis of projected climate changes to bivariate flood quantiles. *Journal of Hydrology*, **566,** 23-42.

Yu, K.-x., L. Xiong, and L. Gottschalk, 2014: Derivation of low flow distribution functions using copulas. *Journal of Hydrology*, **508,** 273-288.

Yu, K. M., Z. D. Lu, and J. Stander, 2003: Quantile regression: applications and current research areas. *Journal of the Royal Statistical Society Series D-the Statistician*, **52,** 331-350.

Yue, S., P. Pilon, B. Phinney, and G. Cavadias, 2002: The influence of autocorrelation on the ability to detect trend in hydrological series. *Hydrological Processes*, **16,** 1807-1829.

Zhang, D. D., D. H. Yan, F. Lu, Y. C. Wang, and J. Feng, 2015a: Copula-based risk assessment of drought in Yunnan province, China. *Natural Hazards*, **75,** 2199-2220.

Zhang, L., and V. P. Singh, 2007: Bivariate rainfall frequency distributions using Archimedean copulas. *Journal of Hydrology*, **332,** 93-109.

Zhang, S., T. Y. Gan, and A. B. G. Bush, 2020: Variability of Arctic Sea Ice Based on Quantile Regression and the Teleconnection with Large-Scale Climate Patterns. *Journal of Climate*, **33,** 4009-4025.

Zhang, T., and Coauthors, 2005: Spatial and temporal variability in active layer thickness over the Russian Arctic drainage basin. *Journal of Geophysical Research: Atmospheres*, **110**.

Zhang, W., X. Mei, X. Geng, A. G. Turner, and F.-F. Jin, 2018: A Nonstationary ENSO–NAO Relationship Due to AMO Modulation. *Journal of Climate*, **32,** 33-43.

Zhang, W., Z. Wang, M. F. Stuecker, A. G. Turner, F.-F. Jin, and X. Geng, 2019: Impact of ENSO longitudinal position on teleconnections to the NAO. *Climate Dynamics*, **52,** 257-274.

Zhang, X., Y. Peng, C. Zhang, and B. Wang, 2015b: Are hybrid models integrated with data preprocessing techniques suitable for monthly streamflow forecasting? Some experiment evidences. *Journal of Hydrology*, **530,** 137-152.

Zhang, X., J. He, J. Zhang, I. Polyakov, R. Gerdes, J. Inoue, and P. Wu, 2012: Enhanced poleward moisture transport and amplified northern high-latitude wetting trend. *Nature Climate Change*, **3,** 47-51.

Zhang, X. B., J. F. Wang, F. W. Zwiers, and P. Y. Groisman, 2010: The Influence of Large-Scale Climate Variability on Winter Maximum Daily Precipitation over North America. *Journal of Climate*, **23,** 2902-2915.

Zolina, O., C. Simmer, K. Belyaev, S. K. Gulev, and P. Koltermann, 2013: Changes in the Duration of European Wet and Dry Spells during the Last 60 Years. *Journal of Climate*, **26,** 2022-2047.